Analysis of Inflow Control Devices for Steam Assisted Gravity Drainage Using Computational Fluid Dynamics

by

Matthew Miersma

A thesis submitted in partial fulfillment of the requirements for the degree of

Master of Science
Department of Mechanical Engineering
University of Alberta

Abstract

One of the main methods of extracting oil from deep oil sands deposits is through the use of steam assisted gravity drainage (SAGD). For the best performance, inflow control devices (ICDs) are implemented along the SAGD production well to even out production and restrict unwanted fluids. Current methods of evaluating these devices rely on criteria that are dependent on the flow rate and fluid properties at which they are measured. In this study, three new criteria are proposed to evaluate and compare ICDs. These new criteria are derived from the physics of the flow in order to tie them to specific aspects of the flow and to have a reduced dependence on the flow rate and fluid properties. To further reduce the dependence of the criteria, they are calculated from a range of data, using a least squares fit. In order to evaluate the proposed criteria, detailed CFD models are developed for six fundamental ICD designs: a $15°$ nozzle, a $40°$ nozzle, a long channel, an expanding nozzle, a device based on Tesla's fluidic diode, and a vortex based device. The CFD models are carefully tested to ensure they accurately model the flow. Using these simulations, the three criteria are calculated for each device. The criteria are then compared to the flow results and examined for flow and viscosity independence. Finally, the criteria are used to compare the six ICDs and identify the best design. The new criteria are not only better than existing criteria for comparing ICDs, but they are also specially adapted to support design development and optimization of new devices.

Acknowledgements

Contents

List of Figures

List of Tables

Chapter 1

Introduction

While Canada has the third largest proven oil reserve in the world, around 97% of this oil is trapped in the oil sands [1], a mixture of viscous heavy oil, sand, and water [2]. To efficiently extract this oil is an ongoing challenge. The first commercial production from the oil sands started in 1967 with surface mining, where the oil sands are removed and processed to extract the oil [3]. While surface mining still makes up 45.7% of production [4], this method is limited to shallow oil sands deposits that are less than 75 m below the surface. For 80% of the oil sands the deposits are too deep for surface mining [2]. To extract from these deep deposits, in situ, or in place, methods were introduced. In these methods steam is injected into the reservoir to heat the oil so it can be extracted directly from the reservoir [2].

With the improvement of in situ methods the production from these wells has grown and, by 2027, production from in situ methods is forecast to account for 56.4% of total production from the oil sands [4] There are two main in situ methods in use today, steam assisted gravity drainage (SAGD) and cyclic steam stimulation (CSS). Of these, SAGD is the predominant method used [5].

1.1   Steam Assisted Gravity Drainage

The need for special in situ methods is dictated by the challenging conditions found in the oil sand reservoir. The bitumen or heavy oil in the oil sands is essentially immobile, because of its high viscosity. This makes it difficult to extract the oil from the reservoir [5]. A conventional oil well will not work, as the oil is too viscous. If the bitumen is heated, its viscosity decreases, allowing it to flow, but the surrounding reservoir is still immobile, preventing the oil from flowing. As soon as the oil cools it returns to a highly viscous state. Thus, to extract the oil it must be maintained at a high temperature as it flows through the reservoir [6].

To maintain this high temperature, the steam assisted gravity drainage method was proposed [7]. In this method, two horizontal wells of 500 to 1000 meters, are drilled through the reservoir, one above another [8]. By continuously injecting steam into the upper injection well, the bitumen is constantly heated. This keeps the bitumen at a high enough

temperature that it can flow down to the lower production well, where it is pumped to the surface. The mechanism for heating the bitumen is the condensation of the steam, when it contacts the bitumen. As the oil is produced, a steam chamber is formed around the injection well, where the oil has been produced [6].

This steam chamber grows throughout the life of the well, as more of the oil is produced. Ideally the chamber grows up and out, extracting more oil from the reservoir. But, when the steam chamber grows irregularly, it can expand downward reaching the production well. When steam breaks through to the production well, steam is produced, severely limiting the performance of the well [8].

A wide variety of fluids enter the production well of a SAGD well pair [5]. To avoid steam breakthrough, while maintaining production, the temperature of the fluids entering the production well is kept several degrees below the saturation temperature of the steam. This ensures that the fluids entering the production well are liquid. This temperature difference, or subcool, is typically kept at less than 40°C [9]. During normal production, an emulsion of oil and water is produced with varying properties, depending on the amount of water being produced [10]. When steam or pure water is produced, the low viscosity and density of these fluids results in a dramatic increase in flow velocity in this section of the well.

Due to the length of the wells, the steam injection and production along the wells tends to be uneven, with most of the production near the heel of the well. In order to even out production, two strings are often used in the wells, with one terminating at the heel and one at the toe of the well. Although this improves the well performance, it tends to result in a dumbbell shaped profile for the steam chamber, where most of the production is from the heel and toe of the well as shown in Figure 1.1. To improve performance inflow control devices (ICDs) can be implement in the production well [8].
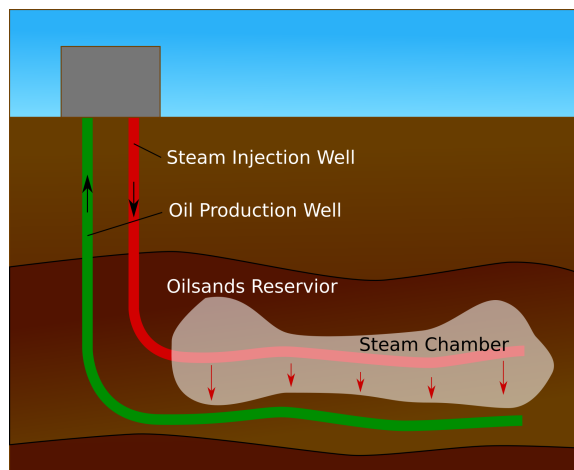
Figure 1.1: SAGD well with dumbbell shaped steam chamber.

1.2   Inflow Control Devices

The purpose of the inflow control devices is to even out production by restricting the flow of high velocity fluids. The pressure drop from the reservoir to the well is relatively constant. But, when there are no ICDs, variations in the reservoir permeability and fluid properties result in large variations in the fluid velocity. The introduction of ICDs produces a pressure drop that reacts to the increased flow rate, balancing the inflow rate. Thus, the ICDs tend towards an even flow distribution along the length of the well [11]. A SAGD well with ICDs is shown in Figure 1.2.
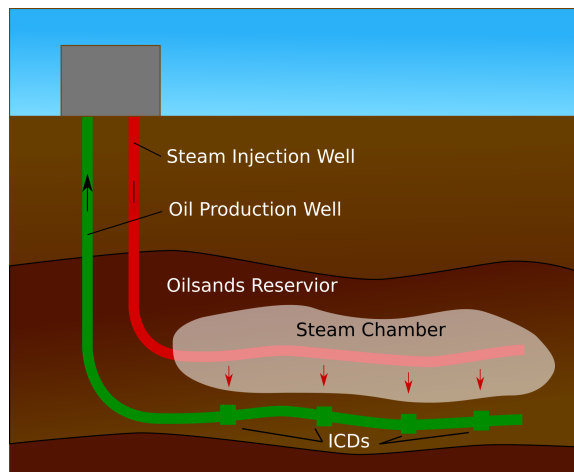
Figure 1.2: SAGD well ICDs.

There are two main types of ICDs in use: the passive ICD and autonomous ICD. The passive ICDs use simple geometries to create the pressure drop, with basic losses. Passive ICDs rely on either an orifice or a channel to create the pressure drop. For the autonomous ICDs, complex geometries are used to generate different flow behaviours, depending on the fluid properties. This allows the device to selectively restrict the flow of steam or water [12].

The simplest design for an ICD is a nozzle or orifice. To investigate the application of an orifice ICD Jones et al. [13] ran a series of experiments testing the effects of various parameters. The number and size of the orifices was varied along with the type of fluid. For the experiments, the pressure drop across the device was measured. The results of these experiments were compared to a theoretical model. For this orifice there was a good fit between the theoretical model and the experimental data. So the theoretical model accurately predicts the behaviour of the ICD. The study also investigated the risk of erosion and plugging to the orifice. The orifice design had only minor erosion and no issues with plugging. For this study the focus was on the behaviour and modelling of a particular device [13].

To compare different passive ICD designs a study was performed by Zeng et al. [14], using computational fluid dynamics (CFD) to simulate the flow through three passive ICD

designs. The study considered an orifice device, a helical channel device, and a short channel, or tube device. Each device was sized for the same flow resistance rating (FRR) define as the pressure drop in bars for a fluid with a density of 998 kg/m^3 and a viscosity of 1 cP at a flow rate of 30 m^3/d (187 STB/d). To compare the devices, simulations were run with a range of flow rates, viscosities, and densities. The pressure drop was then plotted against each of these variables to evaluate the differences in behaviour between the devices. A comparison of the pressure drop versus flow rate plots for water showed only slight differences. Since the devices had the same FRR of 0.8, little change in flow sensitivity was observed and flow sensitivity was not considered. The density sensitivity was greatest for the nozzle design and the viscosity sensitivity for the helical channel design. In addition, the risk of erosion or plugging was evaluated based on the maximum velocity and minimum flow area. The helical channel was found to have the lowest risk of erosion or plugging. Since few details were given as to the mesh quality or simulation setup, it is not possible to determine the quality of the simulations reported in [14].

For autonomous ICD designs, individual studies have been done to investigate the performance of particular devices. Among these designs is the fluidic diode ICD from Halliburton studied by Fripp et al. [12]. The flow mechanism in the device is designed to selectively restrict unwanted fluids. To achieve this the device directs the inflow with a split channel into a circular region with an exit at the centre. For a high inertial flow the fluid flows straight into the circular region causing a vortex that generates a large pressure drop. For a low inertial flow the flow is split in the channel causing the flow to exit directly without causing a vortex. The purpose of this is to create a large pressure drop for the high inertial flow experienced in steam breakthrough and water production. While for the low inertial flow of oil production, it creates a low pressure drop. Thus it encourages oil production and discouraging steam or water production. To test their device Halliburton ran experiments and simulations and compared them to a theoretical model. Although details of the designs and models is not given, Fripp et al. [12] demonstrate a good fit between their models.

To investigate the design of vortex based ICDs, a parametric study was performed by Wang et al [15]. Using CFD simulations, a study was made of the effects of the flow rate and the number, angle, and type of channels entering the circular region or vortex bowl. It was found that the best results were produced by a device with three channels symmetrically placed around the vortex bowl. The preferred channel design had a split angle of 60° , where one branch enters the bowl tangentially and one radially. This device was then simulated using a two-phase flow model with varying water content, density and viscosity. It was found to preferentially produce viscous oil over water, with an increase in pressure drop for mixtures with a high water content. For the CFD simulations, local refinement was used in the mesh to capture the flow in the vortex. To model the turbulent flow a k-ε model was used [15], which is known to provide poor results for vortex flows [16].

Another factor in ICD design is how the ICD is implemented in the well. When deploying

the ICDs in the well, they can either be placed as part of the outer liner or as part of an inner tubing string. When ICDs are deployed in the liner, each ICD has a section of sand control attached to it that feeds directly into the ICD. The liner deployed devices have the advantage that there is a larger inner diameter and only one pipe is needed [17]. But, since the sand control is attached to the ICDs, there is inflow only locally around the ICDs. Because the liner deployed devices are in contact with the reservoir, they cannot be removed for servicing [18]. Most of the devices that have been investigated are liner deployed devices [17]. Since the sand control is built into the device, it is difficult to perform a side by side comparison of the designs.

Tubing deployed devices are placed along a tubing string inside an outer liner that provides sand control the length of the well [17]. Because of the constrained space, these devices tend to have simpler geometries than the liner deployed devices. The advantage of this design is that they allow for inflow everywhere along the well and can sometimes be removed for servicing or replacement. To control the flow, packers are typically placed in the annular region between the tubing and the outer liner. This allows the flow into the ICDs to be isolated from the influence of neighbouring regions [17]. For this study only the simpler tubing deployed devices are considered as the upstream flow is independent of the device. This allows the behaviour of the device to be isolated.

1.3   Tesla Diode

One of the devices included in this study is an ICD design based on Tesla's fluidic diode [19], shown in Figure 1.3. This device is designed to create a low pressure drop for flow in one direction, while producing a high pressure drop in the other direction. Originally designed by Nikola Tesla to act as a one-way flow valve without moving parts, the design would allow the valve to operate with high temperature corrosive flows that would otherwise destroy a valve with moving parts. To increase the effectiveness of the device, Tesla proposed that multiple devices be placed in a series to maximize the one-way character of the device [19].

Recent studies have adapted this device for use in mini-channels to provide a one-way flow valve [20–23]. For this application, the Reynolds number at the entrance to the device is small and laminar or transitionally turbulent flows are expected. Studies of Tesla's diode have focused on optimizing the diode properties of the device, as defined by the diodicity, the ratio between the pressure drop in opposite flow directions [20–23]. This device has not previously been used in the design of ICDs. To use this as an ICD, the device is used in the reverse direction so the device creates a large pressure drop.

While most studies have been for laminar flow, a study by Thompson et al. [20] has investigated the transitionally turbulent flow behaviour of the device for a Reynolds number range of 500 to 2000. To study the device, CFD simulations were used. By demonstrating grid independence, the model was verified. To correctly capture the transitional turbulence, the results of three different turbulence models were compared to experimental data and 2D
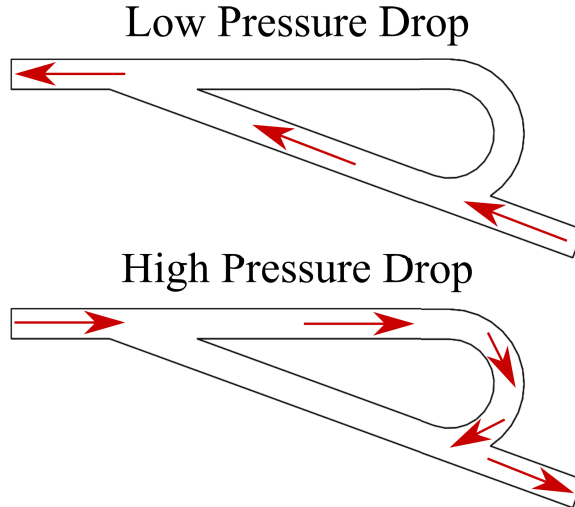
Figure 1.3: Pressure drop mechanism in Tesla diode.

laminar simulations. It was found that the k-ε turbulence model greatly underpredicts the diodicity of the device. Both the k-ω shear stress transport (SST) and the three equation k-k_L-ω models provided an accurate simulation of the flow in the diode. It was demonstrated that the diodicity of the device increases with the Reynolds number of the flow [20].

1.4   Fluid Dynamics of ICDs

Once the flow leaves the reservoir and enters the production well, it passes through a variety of different flow regions before it is incorporated into the main flow inside the inner liner. In the initial sections, as it passes through the slots and the annulus, the flow rate is low. As the flow enters the device the flow rate increases resulting in turbulent flow as the flow exit as a jet into the main flow in the inner liner. To understand the expected flow behaviour in these regions, previous research into these flows is examined. For each region, the Reynolds number of the flow can be used to predict the expected type of flow. The Reynolds number is defined by

$$\text{Re} = \frac{\rho u D}{\mu} \tag{1.1}$$

where Re is the Reynolds number, ρ is the fluid density, u is the average velocity of the flow, D is the diameter, and μ is the fluid viscosity. For non-circular geometry, the hydraulic diameter is used instead. The Reynolds number gives the ratio of the inertial and viscous forces in the flow [24].

As the flow enters the outer liner, it passes through narrow slots in the liner that provide sand control. Since the overall production is spread out over all the slots, the flow rate through each individual slot is small. As detailed by Mahmoudi et al [25], with sand

6

production the slots can become plugged, increasing the flow rate in the remaining slots. When all the slots are open production rates vary from 10 to 30 ml/h/slot. When the slots become plugged the flow can, in extreme cases, reach 600 ml/h/slot. Compared to the pressure drop in the reservoir or the ICDs, the pressure drop in the slots is insignificant [25]. The flow in the slots was investigated by Rasimarzabadi et al. [26]. With the low flow rates, the Reynolds number of the flow in the slot is below one and creeping flow is expected. The hydraulic diameter of the slot is given by

$$\text{D}_\text{h} = \frac{4ab}{2(a+b)} \tag{1.2}$$

where a and b are the length and width of the slot, respectively. For a straight slot a fully developed profile develops across the slot, when the depth of the slot is greater than the slot width [26].

As the flow exits the slots it enters an annular region between the slotted liner and the inner tubing. Since the slots are evenly distributed in the outer liner, the flow rate in the annular region continuously increases as the flow gets closer to the ICD and more flow is added from the slots.

As the flow enters the device, the flow rate rapidly increases. To understand the flow in the device, the models for simple devices are examined. The physics of the flow through basic orifices and channels has been studied in detail, and pressure losses can be modelled using the Bernoulli equation with losses for internal flow, given in equation 1.3.

$$\frac{P_1}{\rho} + \frac{V_1^2}{2} + gz_1 = \frac{P_2}{\rho} + \frac{V_2^2}{2} + gz_2 + \left(f\frac{L}{D} + \sum K_L \right) \frac{V^2}{2} \tag{1.3}$$

where P is the pressure at two points, V is the velocity at two points and in the device, z is the height at two points, ρ is the density, g is the gravitational acceleration, f is the Darcy friction factor, L is the length of the flow path, D is the diameter, and $\sum K_L$ is the sum of the minor loss coefficients. The pressure losses are divided into minor losses, resulting from changes in flow geometry, and major losses from friction between the fluid and the wall [24].

For the case of passive ICDs and single phase incompressible fluids the pressure loss behaviour of the flow is often predicted using the minor losses and frictional losses from equation 1.3, as exemplified in Aadnoy et al. [27]. By breaking down the device into a series of nozzles, bends, and channels, the minor loss coefficients and friction factor for each section can be estimated. Once the coefficients are known, the sum of the losses can be used to predict the behaviour of the device [27].

For the autonomous ICD designs other types of flow behaviour create additional pressure losses in the devices. In vortex based designs, like Halliburtons fluidic diode, the fluid causes a vortex as it tangentially enters the circular region [12, 15]. This vortex takes the form of a compound or Rankine vortex, where the outer part of the vortex is irrotational and the core of the vortex rotates as a solid body as it exits the region. This results in an increase

in the tangential velocity of the flow as it approaches the core with a sudden decrease at the core. As the velocity increases the pressure decreases by Bernoulli's equation. This drop in pressure depends on the strength of the vortex [28].

For the pressure drop in the Tesla diode two proposed mechanisms are outlined in Bardell [23]. The first describes the pressure drop in terms of the momentum of the jet at the intersection where the channels rejoin. By performing a momentum balance for a control volume at this intersection the pressure loss can be estimated. The second approach views the impingement of the jet from the loop as creating a vena contracta in the flow at the channel intersection. This contraction of the flow then produces a pressure loss [23].

The exit of the device into the flow in the inner liner is complicated by the interaction of the two flows. As the flow exits the device it creates a jet into the crossflow in the liner. Once the jet enters the crossflow it is entrained into the main flow. Studies of the mechanism for this entrainment found that, for perpendicular jets, vortices in the jet are the primary source of entrainment [29, 30]. As the jet enters the crossflow, the flow around the jet causes two counter rotating vortices in the jet. As the vortices pull flow from the crossflow into the jet, the jet is quickly entrained into the crossflow. To understand the flow, detailed direct numerical simulations were performed and compared to experimental data. Due to the complex nature of the flow, even advanced models struggled to precisely model the complex flow structures [29].

1.5 Device Erosion Mechanics

In the SAGD production well small sand particles are carried with the fluid that cause erosion to the ICDs as they impact the walls of the device [17]. There are a large number of factors that affect the rate of erosion, ranging from the angle and velocity of the particles to the physical properties of the particles and the material used for the device [17].

To reduce sand production, various forms of sand control are used in the production well, such as slotted liners. While these cannot completely prevent sand production, they greatly reduce the amount of sand produced and the size of the particles [25]. The erosion rate is affected by the size of the particles, with larger particles causing significantly greater erosion. The hardness and shape of the particles also affects the erosion rate [31].

Another significant factor in the erosion rate is the material used for the device. In general the erosion rate decreases when a harder material is used [32]. In addition to the material, the impact angle of the particle affects the erosion rate. But the effect of the angle is connected to the material with ductile materials eroding more at lower angles and brittle materials eroding more at higher angles [31].

The impact velocity of the particles also affects the erosion rate in the device, with a power law increase in the erosion rate as the velocity increases so that

$$\text{Erosion Rate} \propto v^n, \quad (n > 0) \tag{1.4}$$

where v is the impact velocity and n is a constant [33]. The value of the exponent, n, depends on the properties of the materials involved in the erosion [33, 34].

Although there are many factors that affect the erosion, the two factors that can be controlled when designing the shape of a device are the impact velocity and impact angle. Since the best impact angle depends on the material, the main quantity to control is the impact velocity of the particles.

1.6   Current Performance Criteria

While the physics of the flow in the devices is useful for modelling their performance, a general set of quantifiable criteria is desirable when comparing devices. These criteria are designed to quantify an aspect of the performance of the ICD. Using these criteria devices are compared and an appropriate device is selected when designing a well. To derive the criteria, simplified physics models are usually used [14, 35].

Current criteria focus on the pressure drop in the device. One of the primary values used to characterize an ICD is the flow resistance rating (FRR) of the device. The FRR is defined as the pressure drop in bars across the device for the following conditions [14]:

- Flow rate: 187 STB/d

- Viscosity: 1 cP

- Density : 998.2 kg/m^3

By running experiments or simulations at these conditions the FRR value of a device is measured. Devices can be compared using this value to determine the flow resistance of a device. But this does not give an indication of the behaviour of the devices as the flow properties change. Thus the FRR value is of limited use in evaluating a device's flow performance. Many devices are available with a range of FRR values or with the ability to adjust the device to achieve a particular value [36]. The main use of the FRR value is in sizing devices for a desired pressure drop and in selecting appropriately sized devices, when designing a well. The FRR values for the devices are used in well simulations, and are selected based on the expected production in each section of the well [37].

The Bernoulli equation has been shown to provide a good model of the flow behaviour for passive ICDs [13]. To extract a single value for the losses the total losses are often combined. For nozzles or orifices, the losses are described with the discharge coefficient, C_d where the losses are given as

$$\Delta P = \frac{\rho u^2}{2C_d^2} \tag{1.5}$$

where u is the average flow rate in the device. For channels the losses are combined into a total loss coefficient, K_t, given by

$$\Delta P = K_t \, \frac{\rho u^2}{2} \tag{1.6}$$

The discharge coefficient corresponds to the ratio of the actual and theoretical mass flow rate through the device. This works well for devices where the minor losses dominate [35]. But, the discharge coefficient depends on the Reynolds number of the flow in the device, especially for low Reynolds numbers. Since the discharge coefficient includes the frictional losses, its Reynolds number dependence increases, when the device include channels and bends. This coefficient is intended for short nozzles or orifices, in which the frictional losses are relatively small. Because of this limited scope and its variation with Reynolds number, the discharge coefficient struggles to provide a single quantitative value for comparing devices. This variation also means that, if the coefficient is calculated from a single flow case, it can only be compared at those flow conditions.

For channel type designs with significant frictional losses, the total loss coefficient is sometimes used instead. But this loss coefficient also depends on the flow conditions [35]. While it helps to describe the behaviour of the device, the total loss coefficient depends on the flow rate and Reynolds number and does not provide a fixed criterion to characterize the behaviour of the device.

These coefficients are not constant but are highly dependent on the flow conditions. To predict this dependence various models have been proposed that relate the coefficients to the flow conditions [13, 38]. One proposed model expresses the loss coefficient as a function of Reynolds number with seven coefficients that are determined by a regression analysis [38]. While this provides a good fit to the data for more complex designs, the resulting equation is complicated and the coefficients do not correspond directly to particular flow behaviours in the device.

Due to the variability of these coefficients, other qualitative comparisons are often used. By plotting the pressure drop against the flow rate, viscosity, or density, a qualitative comparison can be made between different devices [12]. This also allows the behaviour for different fluids to be compared, where both the viscosity and density vary.

1.7 Erosion Criteria

Another consideration for ICD performance is the effect of erosion on the device. To study this issue experiments are performed to test the erosion in the device [13, 38]. For these experiments small sand particles are added to the flow and the experiment is run for an extended period. The device is then examined to determine the amount of erosion. To provide a measure of the erosion over the life of the well, these experiments use increased particle concentrations that approximate the expected erosion for the lifetime of the well [13, 38]. The experiments indicate whether the device will fail for the expected conditions, but do not provide details on the erosion rate.

To better understand the erosion, a study was performed by Olsen et al. to investigate the erosion rate in nozzle devices and its effect on the performance of the device [34]. For the study CFD simulations were performed with a Lagrangian formulation to track particles injected into the simulation. With this setup the impact of the particles with the wall of the ICD was tracked to determine the erosion rate of the device. Using this setup, the sensitivity of the erosion rate to different factors was tested. It was found that the primary source of erosion was from flow separation that caused the particles to be concentrated when impacting the wall. By using fillets at the entrance of the nozzle or using a more vertical nozzle the separation and erosion can be reduced. In addition to the flow behaviour, the erosion is dependent on the size and concentration of the particles and on the erosion resistance of the material in the device. For the simulations, several turbulence models were tested including the k-ω SST and realizable k-ε model. Although the erosion rate was dependent on the turbulence model, a preferred model could not be identified, since there were no experimental results for comparison [34].

Both experimental and numerical methods of predicting erosion require an extensive study. For a simpler method of comparing erosion rates in devices, the maximum velocity is used. To use this the devices must be sized for the same pressure drop and compared at the same volumetric flow rate [14]. For all these methods the erosion is only predicted for a particular flow case.

1.8   Objective

The goal of this study is to develop a set of new criteria that can be used to analyze and compare ICD designs for SAGD wells. For these criteria to be effective, they should address the issues with current criteria. The criteria should be less dependent on the flow rate and fluid properties at which they are calculated, and multiple criteria should be used to address the various aspect of the device performance. Finally, the criteria should be designed so they can be easily used, when optimizing an ICD design or developing new designs.

To demonstrate the proposed criteria, high quality CFD models are developed for six ICD fundamental designs, ranging from basic nozzle and channel designs to complex autonomous ICD designs. The CFD models must be carefully constructed to ensure they accurately predict the flow in the ICDs. By comparing the simulated results to the new criteria, the relationship of the criteria to the flow can be investigated. The dependence of the new criteria can be examined by comparing the criteria, calculated at different flow rates and viscosities.

To achieve this objective, the study must first examine the governing physics of the flow. In Chapter 2, the underlying physics of the flow are developed from the governing equations, along with the CFD models used to simulate the flow. In Chapter 3, the limitations of the current criteria are analyzed and, based on the physics of the flow, three quantitative criteria are proposed. In Chapter 4, the details of CFD models are described, along with the

verification and validation needed to ensure accurate models. The results of the simulation are presented in Chapter 5, where the flow structures are examined to understand the pressure losses and erosion in the devices. The criteria are then analyzed in Chapter 6, where the proposed criteria are compared to the flow results and tested for flow rate and fluid dependence. Finally, using the criteria, the six ICD designs are compared to identify the best design.

Chapter 2

Fluid Dynamics

The flow behaviour of ICDs is the result of the physics of the flow as defined by the governing equations. These equations are the starting point for understanding the flow. By solving a simplified form of the equations the CFD simulations are used to predict the flow in the devices. Then, by further simplifying the equations, a set of criteria is derived to quantify the performance of the devices. Different devices can then be compared using these criteria.

2.1 Fundamental Equations

The physics of the flow through an ICD is governed by the conservation equations of mass, momentum, and energy. The fundamental differential form of these equations without simplifications is given in equations 2.1 through 2.4. For the continuity equation the conservation of mass is expressed by

$$\frac{\partial \rho}{\partial t} + \nabla \cdot (\rho \vec{v}) = 0 \tag{2.1}$$

where ρ is the density, t is the time, and $\vec{v}$ is the velocity vector. The conservation of momentum is given by

$$\frac{\partial \rho \vec{v}}{\partial t} + \nabla \cdot (\rho \vec{v} \vec{v}) = \nabla \cdot \vec{T} + \rho \vec{b} \tag{2.2}$$

where $\vec{b}$ is the vector of body forces on the fluid and $\vec{T}$ is the stress tensor for the fluid given in index notation as

$$T_{ij} = -\left(P + \frac{2}{3}\mu \frac{\partial u_k}{\partial x_k}\right)\delta_{ij} + \mu\left(\frac{\partial u_i}{\partial x_j} + \frac{\partial u_j}{\partial x_i}\right) \tag{2.3}$$

where P is the pressure, μ is the viscosity, and u_i is the velocity vector in index notation. The conservation of energy equation is given by

$$\frac{\partial \rho h}{\partial t} + \nabla \cdot (\rho \vec{v} h) = \frac{\partial P}{\partial t} + \nabla \cdot (\vec{v}P) + \nabla \cdot (k\nabla T) + \dot{Q} \tag{2.4}$$

13

where h is the enthalpy of the fluid, k is the thermal conductivity, T is the fluid temperature, and $\dot{Q}$ is the sum of the heat sources.

2.2   Flow Assumptions

For the purposes of this study the focus is on the behaviour of the flow in the vicinity of the device for different flow conditions. To simplify the equations for this case, the flow conditions in the production well are analyzed. Based on this analysis a set of assumptions is formulated and applied to the fundamental equations.

In a SAGD well a variety of different fluids is produced. As the steam condenses on the walls of the steam chamber, the liquid water and heated bitumen form an emulsion that flows down to the production well. This emulsion makes up the primary flow entering the production well during regular production [39]. To represent its behaviour, the emulsion can be treated as a single phase fluid with effective fluid properties [40]. This is a rough approximation, as the multiphase characteristics of the emulsion still affects the flow behaviour. In addition, this emulsion of the oil and water increases the viscosity of the emulsion [10, 39, 40]. When water is produced with the emulsion the water easily flashes into steam in the device. Thus, in case of steam breakthrough of steam flashing, wet steam will be produced and the multiphase character of the flow will greatly change the behaviour of the device [41]. For this study the scope is restricted to the production of single phase flow and the effects of the basic fluid properties.

During regular production of the oil water emulsion and the liquid water have a high density and a low flow rate. For these conditions the flow is expected to be incompressible with a Mach number well below 0.3. However, when the water flashes into steam of steam breakthrough occurs, the low density high velocity flow is compressible. Since only single phase flow is considered, these compressible flow conditions are outside the scope of this study. Thus it is assumed that the flow through the ICD is incompressible.

Finally, it is assumed that the fluids are newtonian with a constant viscosity. While bitumen does exhibit non-newtonian behaviour, it approaches newtonian behaviour at the high temperatures experienced in a SAGD well [42]. The water and steam are also newtonian. Thus a constant viscosity assumption is valid.

The only body forces on the fluid is the gravitational force. When the ICDs are deployed in the well, the orientation of the devices is random. Typically there are at least two devices at each location distributed symmetrically around the pipe. While the orientation of the device may effect the performance, it is not considered in this study and is left for future research. It is assumed that any gravitational effect on one device will be cancelled out by the other devices at that location.

For the simulations an isothermal condition is assumed, since there are no sources of heat and the fluid maintains a relatively constant temperature. If the temperature is constant and the flow is incompressible, the terms of the energy conservation disappear. Thus, for

the purpose of simulating the flow, the energy conservation equation is neglected. Although it is not used in the simulations, it is used in its most basic form to derive the Bernoulli equation and losses.

2.3 Simplified Equations

Summarizing the simplified flow model, gives the following assumptions

- Single phase flow

- Incompressible flow

- Newtonian flow

- Negligible effect of gravity

- Isothermal flow

This set of assumptions is then applied to the fundamental equations and the equations are simplified. After making these simplifications the energy equation is removed, and the continuity and momentum equations are given as

$$\nabla \cdot \vec{v} = 0 \tag{2.5}$$

$$\rho \frac{\partial \vec{v}}{\partial t} + \rho \nabla \cdot (\vec{v}\vec{v}) = -\nabla P + \mu \nabla^2 \vec{v} \tag{2.6}$$

Over the life of a SAGD well there are large changes in the production rate. But most of these changes occur gradually, so the inflow rate is relatively constant. Depending on the design of the ICD, transient behaviour may occur in the device, but any oscillations will quickly disappear in the large main flow in the inner liner. Therefore for most simulations it is valid to assume steady state flow in the devices, since any variations in the flow are too gradual or localized to affect the performance of the devices. For these steady state simulations, the momentum conservation equation can be further simplified, giving

$$\rho \nabla \cdot (\vec{v}\vec{v}) = -\nabla P + \mu \nabla^2 \vec{v} \tag{2.7}$$

By discretizing these equations over a mesh, the CFD solver can predict the flow through an ICD.

2.4 Bernoulli Equation

To derive a set of criteria, a more simplified set of equations is needed. Although the energy conservation equation is not used in the simulations, it can be used, in its basic form, to

derive the Bernoulli equation and understand the pressure losses through an ICD. The energy conservation equation for a control volume is

$$E_{\text{in}} - E_{\text{out}} = 0 \tag{2.8}$$

where E is the energy in the system. As the flow passes through a control volume surrounding the ICD the energy in the flow is conserved according to equation 2.8. The energy in and out of this volume consists of two kinds: mechanical energy and thermal energy. The only thermal energy introduced into the system is from mechanical energy that is converted into thermal energy. These mechanical energy losses result in a slight heating of the fluid. This added thermal energy is very small and has a negligible effect on the temperature of the fluid [24]. Since there are no other heat sources in the system, it is assumed to be isothermal. Thus the energy conservation equation can be written in terms of only the mechanical energy. This gives

$$E_{\text{mechanical, in}} - E_{\text{mechanical, out}} - E_{\text{mechanical losses}} = 0 \tag{2.9}$$

Here the mechanical losses represent a negative energy source term. The mechanical energy in and out of the volume consists of three elements: the flow energy, the kinetic energy, and the potential energy. The mechanical energy in is given by

$$E_{\text{mechanical, in}} = \frac{P_{\text{in}}}{\rho} + \frac{V^2}{2} + gz \tag{2.10}$$

where V is the average velocity and z is the vertical location. The Bernoulli equation with losses is derived by inserting equation 2.10 into equation 2.9 giving

$$\frac{P_{\text{in}}}{\rho} + \frac{V_{\text{in}}^2}{2} + gz_{\text{in}} = \frac{P_{\text{out}}}{\rho} + \frac{V_{\text{out}}^2}{2} + gz_{\text{out}} + E_{\text{mechanical losses}} \tag{2.11}$$

By rearranging this equation an expression can be derived for the pressure loss across the device. Solving for the change in pressure gives

$$\Delta P = \rho \frac{V_{\text{out}}^2 - V_{\text{in}}^2}{2} + \rho g(z_{\text{out}} - z_{\text{in}}) + \rho E_{\text{mechanical losses}} \tag{2.12}$$

As for the fundamental equations, the effects of gravity are neglected, because any gravitational effects will cancel out. The focus is on the flow in the ICD, so to simplify equation 2.12, the velocities are expressed in terms of the average velocity, u at the narrowest point in the ICD. The continuity equation for incompressible flow gives

$$A_{\text{in}}V_{\text{in}} = A_{\text{out}}V_{\text{out}} = A_{\text{icd}}u \tag{2.13}$$

where A is the cross sectional area of the flow at the narrowest point in the ICD. Applying this to equation 2.12 gives

$$\Delta P = \frac{1}{2}\rho \left(\frac{A_{\text{icd}}^2}{A_{\text{out}}^2} - \frac{A_{\text{icd}}^2}{A_{\text{in}}^2} \right) u^2 + \rho E_{\text{mechanical losses}} \tag{2.14}$$

Since the geometry is fixed, the cross sectional areas are constant and can be replaced with a single constant giving

$$\Delta P = \frac{1}{2}\rho C_{\text{area}} u^2 + \rho E_{\text{mechanical losses}} \tag{2.15}$$

2.5 Mechanical Losses

As the fluid passes through the device, some of the mechanical energy of the fluid is converted into thermal energy. There are two main sources of these losses, the frictional losses at the wall and the losses caused by flow separation and mixing in the flow [24]. These energy losses result in additional pressure losses through the device.

2.5.1 Major Losses

The major or frictional losses are the result of the interaction between the fluid and the surrounding walls. At the walls a no-slip boundary condition applies so that fluid has zero velocity at the walls. The friction of the fluid, characterized by the viscosity, creates a boundary layer at the wall. For pipe flow this creates a velocity profile across the pipe. This friction in the fluid results from the velocity gradient across the flow. The friction causes some of the mechanical energy of the fluid to be dissipated as heat. Based on a dimensional analysis of the factors affecting frictional losses, the dimensionless Darcy friction factor f can be used to relate the quantities [24]. For flow in a pipe these frictional losses can be calculated as

$$\Delta P_{\text{friction}} = f \frac{L}{D} \frac{\rho u^2}{2} \tag{2.16}$$

where L is the length of the pipe, and D is the diameter of the pipe. The value of the friction factor is a function of the Reynolds number of the flow and the surface roughness of the wall. For laminar flow (Re < 2300) the friction factor can be shown to be given by $64/\text{Re}$ and is independent of the roughness of the pipe. At high Reynolds numbers, the surface roughness dominates and the friction factor is constant.

2.5.2 Minor Losses

Minor losses are generated when the fluid passes through changes in geometry. These geometry changes cause flow separation and eddies in the flow that dissipate energy as they decay [24]. Since these losses are hard to predict, they are usually estimated using a loss coefficient that is derived empirically. These losses are expressed by

$$\Delta P_{\text{minor}} = K_L \frac{\rho u^2}{2} \tag{2.17}$$

where K_{L} is the loss coefficient for the system. Sudden changes in geometry tend to trigger flow separation which results in a high loss coefficient. Geometry with rounded corners and gradual transitions avoids flow separation resulting in a much smaller loss coefficient. Sharper angles also tend to result in greater losses [43].

2.5.3 Total Losses

An equation for the total pressure loss can be derived by replacing the mechanical losses in equation 2.15 with losses in equations 2.16 and 2.17. This gives

$$\Delta P = \frac{1}{2}\rho C_{\text{area}}u^2 + f\frac{L}{D}\frac{\rho u^2}{2} + K_L\frac{\rho u^2}{2} \tag{2.18}$$

Finally, combining the area coefficient with the loss coefficient gives

$$\Delta P = \frac{1}{2}(K + \frac{fL}{D})\rho u^2 \tag{2.19}$$

This equation then provides a theoretical model for the pressure drop behaviour of an ICD. However the loss coefficient and friction factor are not known in most cases. While this can only provide a rough approximation of the pressure drop across a device, it can be used to derive a set of criteria that are calculated from CFD simulation.

2.6 CFD Models

For this study, simulations were performed using ANSYS® CFX 17.1. This software provides the advanced meshing capability needed for the complex designs that are considered [44]. For the mesh, it uses an element-based finite volume based method to discretize the governing equations given in equations 2.5 and 2.7.

2.6.1 Meshing

As explained in the ANSYS theory guide [45], a finite element based approach is used to produce the mesh. In this method the volume of the domain is divided up into finite elements of various types. For the main body of the flow the mesher defaults to tetrahedral elements, while for uniform flow areas hexahedral element can be selected. In the inflation layer at the wall prism and hexahedral elements are used to capture the boundary layer in the flow [45].

Although the mesh is created with elements, the value of the solution field is stored at the nodes that form the corners of the element. By using shape functions for the elements the value of the solution field at any point in an element can be calculated with a trilinear interpolation from the values at the nodes of the element [45].

2.6.2 Discretization

For the discretization of the governing equations the integral form of the equations is used on control volumes surrounding each node in the mesh. To estimate the values at the surface of the control volume, the element shape functions are used to linearly interpolate the value [45].

To discretize the advection it is necessary to estimate the value of variables at integration points around the control volume. The values at these integration points is then used to calculate the surface integral around each control volume. A variable, ϕ_{ip}, can be estimated at an integration point, using the following formula.

$$\phi_{\text{ip}} = \phi_{\text{up}} + \beta \, \nabla \phi \, \vec{r} \tag{2.20}$$

where ϕ_{up} is the variable value at the upwind node, β is a blending factor, $\nabla \phi$ is the average gradient of the variable, and $\vec{r}$ is the vector from the upwind node to the integration point. For a blending factor of $\beta = 0$, the scheme is a first order accurate upwind differencing scheme (UDS). For a blending factor of $\beta = 1$, the scheme is a second order accurate central differencing scheme (CDS) [45].

While a UDS scheme is the most robust it creates artificial diffusion and is only first order accurate [16]. This scheme is used for initial simulations to aid convergence, but a higher order scheme is needed for the final results. For the final simulations, the high resolution scheme is used. This scheme uses an algorithm to maximize the value of β for each node to achieve a high order solution, while avoiding artificial oscillations in the solution [45]. Since this method uses a variable value for β, the order of the error is not consistent and it cannot be used for mesh independence calculations. For the mesh independence simulations a fixed blending factor of 0.7 is used to achieve a fixed error order.

2.6.3 Turbulence

The Reynolds numbers in the device is defined at the narrowest cross-section of the device, using the minimum diameter in the device and the average flow rate at that point. For the simulations the Reynolds numbers in the devices range from less than 1,000 to 1,868,000. Thus turbulence is expected in many of the simulations [8, 27, 34, 38]. One of the most common ways of modelling turbulence is through the use of Reynolds averaged Navier-Stokes (RANS) models [16, 45]. For these, the velocity is expressed as

$$u_i = \bar{u}_i + u_i' \tag{2.21}$$

where $\bar{u}_i$ is the time averaged velocity and u_i' is the turbulent fluctuations in velocity. Inserting this into the momentum conservation equation gives

$$\frac{\partial \rho \bar{u}_i}{\partial t} + \frac{\partial}{\partial x_j}(\rho \bar{u}_i \bar{u}_j) = \frac{\partial}{\partial x_j}(\overline{T_{ij}} - \rho \overline{u_i' u_j'}) + \rho b_i \tag{2.22}$$

19

Thus the turbulent fluctuations are confined to the six terms given by $\rho \overline{u_i' u_j'}$. These are called the Reynolds stresses. This equation can still be used for transient simulations, by time averaging over time period larger than the scale of the turbulence but smaller than the time step used in the simulation. For complex flows, like a vortex, the turbulence is modelled by solving the transport equations of the six Reynolds stresses [16, 45].

Calculating the transport of all six stress terms is computationally expensive, as it introduces six additional transport equations that must be solved. One proposed way of simplifying this is through the addition of an eddy viscosity that accounts for the Reynolds stress term. This eddy viscosity is add to the fluid viscosity to give an effective viscosity $\mu_{\text{eff}} = \mu_{\text{fluid}} + \mu_{\text{t}}$. The commonly used two equation turbulence models work by providing a model for this eddy viscosity [16, 45].

In the $k - \varepsilon$ model the turbulence kinetic energy, k, and the turbulence eddy dissipation rate, ε are used to calculate the eddy viscosity, according to the equation

$$\mu_t = C_\mu \rho \frac{k^2}{\varepsilon} \tag{2.23}$$

where C_μ is a constant. Two transport equations are added for k and ε. This model works well in free stream flows but struggles to model the near wall flow and the location of flow separation. In the $k - \omega$ model the turbulent frequency, ω is used instead of the eddy dissipation rate, so that

$$\mu_{\text{eddy}} = \rho \frac{k}{\omega} \tag{2.24}$$

While this model is accurate near the wall, it tends to be sensitive to freestream conditions. These models can be implemented at a low computational cost, as only two additional equations need to be solved [16, 45].

For the simulations in this study the shear stress transport (SST) model in CFX is used. This model blends the $k - \varepsilon$ and $k - \omega$ models to provide accurate turbulence modelling near the wall with the $k - \omega$ model and in the freestream flow with the $k - \varepsilon$ model [45].

Chapter 3

ICD Assessment

The physics of the flow were investigated along with the computational fluid dynamics that are used to predict the flow. Now the loss equation 2.19 and the CFD models need to be applied to ICDs and the evaluation of ICD performance. To compare ICD designs, it is important to have quantifiable criteria that can be used to describe the performance of the ICDs. With appropriate criteria, different devices can be compared and a suitable design can be selected. Current criteria, however, are limited and an improved set of criteria is needed. Here, a new set of criteria is proposed and tested using CFD simulations.

3.1 ICD Performance Goals

The purpose of the ICDs is to improve the well performance by restricting unwanted fluids and promoting even production along the length of the well [8]. The goal when designing an ICD is to make it react to changes in the fluid and flow rate so that undesirable fluids, like water of steam, are held back while oil is produced. When oil is produced, the fluid has a high viscosity and flows slowly. When water is produced the fluid is less viscous and flows faster. Ideally the ICD would encourage the production of oil with a low pressure drop, while restricting the production of water using a high pressure drop.

To examine how well a design achieves this behaviour, criteria are used to evaluate the performance of the device. For this study, two aspects of the performance are focused on, namely the flow behaviour and the levels of erosion in the device. Current performance criteria are examined and a new set of criteria are proposed. These new criteria are designed to provide an improved method of evaluating and comparing ICD designs.

3.2 Ideal Characteristics of Performance Criteria

When developing new ICDs or comparing current designs, the criteria should be linked to the performance of the ICDs and be independent of the flow conditions. To determine the quality of criteria a standard is developed that details the ideal characteristics of a set of criteria. By comparing criteria with this standard, the quality of the criteria can be

evaluated.

An ideal set of criteria should be

- Independent of the flow rate

- Independent of the fluid properties

- Independent of the scale of the device

- Quantifiable value that can be easily measured

- Linked to specific aspects of the performance

- Adapted for use in a design optimization

Independence from the flow rate is important, since the flow rate through the device varies greatly over the life of the well, depending on the fluid being produced. In connection with this, the criteria should also be independent of the properties of the fluid being produced. Ideally the criteria are exclusively dependent on the design of the device. In this way, the overall performance of the device can be quantified.

Even for a single ICD design, the device is scaled by adjusting the dimensions to achieve a particular flow resistance. To prevent this device scaling from affecting the values, the criteria should be independent of the scale of the device. Although the criteria should not depend on all dimensions, there are dimensions inherent in the design that should be included in the criteria.

In calculating the criteria, precisely quantifiable values should be used that allow for their detailed comparison. Since there is a wide range of designs, the criteria need to be defined, so they are not restricted to only a few types of designs. For this, the criteria should be based on the performance for a wide range of flow conditions. At the same time, the criteria should be calculated from a small set of data, to avoid extensive simulations or testing.

For the criteria to be meaningful, they should be tied to specific aspects of the device's performance. By having a set of criteria that quantify key aspects of the performance, an informed comparison can be made between ICD designs. In reality, criteria that meet precisely all these conditions cannot be found. But by comparing criteria to this standard, the quality of the criteria can be evaluated. Based on these ideal characteristics current criteria can be evaluated and an improved set of criteria can be developed.

Although multiple criteria allow for an informed comparison, the lack of a single value makes it challenging to select an optimum design. To resolve this issue the criteria should be designed for an optimization. Although the criteria are not used for an optimization in this study, the criteria are designed to be used in future work, when optimizing a design. For an optimization the criteria should produce the best results when they are minimized. Then the criteria can easily be used in a design optimization like that proposed by Li et al. [46] for

outflow control devices. In this type of optimization various design parameters are varied, using design of experiments, to find the design that minimizes the criteria [46, 47]. By designing the criteria to be minimized, they can also be combined in a single cost function for optimization.

3.3   Limitations of Current Criteria

To evaluate the current criteria, detailed in Chapter 1, they are compared with the ideal criteria characteristics. Current criteria for ICDs are used to provide a quantitative measure of the flow resistance of the device. The most basic measure is the flow resistance rating, defined as the pressure drop in bars for water at a flow rate of 187 STB/d [14]. While this is useful for sizing a device, it is dependent on the scale of the device and cannot be used to compare designs. As a single pressure drop value, it does not give any information on the behaviour of the device.

The most commonly used criteria for analyzing the behaviour of ICDs are the discharge coefficient, C_d, defined as

$$\Delta P = \frac{\rho u^2}{2C_d^2} \tag{3.1}$$

and the total loss coefficient, K_t, defined as [13, 35, 38]

$$\Delta P = K_t \frac{\rho u^2}{2} \tag{3.2}$$

These are relatively independent of flow rate and fluid properties for orifices, when the Reynolds number is large. But, when the Reynolds number is small or the device has significant frictional losses, they become dependent on the flow rate and fluid properties [35]. This dependence means that the criteria can only be compared at similar flow conditions. Because of this dependence, they do not fully describe the behaviour of the devices.

The reason for this dependence is that the pressure losses are the combination of two types of losses. In Chapter 2 the pressure loss behaviour of ICDs was expressed using the Bernoulli equation, where the losses are given by

$$\Delta P = \frac{1}{2} \left(K + \frac{fL}{D} \right) \rho u^2 \tag{3.3}$$

For these criteria, the minor and frictional losses are combined into a single coefficient, as either the total loss coefficient or the discharge coefficient. By including the frictional losses in the coefficient, the coefficient becomes dependent on the flow rate and fluid properties, since the friction factor depends on the Reynolds number of the flow. Due to this dependence the coefficients are often expressed as a function of the Reynolds number in the device. While it would be convenient to express the losses as a function of only the Reynolds number, it is not this simple. Although the friction factor is a simple function of the Reynolds number,

the rest of the loss equation shows a separate dependence on the density and flow rate, resulting in a complex dependence.

Since the discharge coefficient and total loss coefficient are not fixed, a comparison of the coefficients has a limited scope. To allow for a broader comparison, plots of the flow behaviour are often used to qualitatively compare devices [12, 13, 15]. By inspecting the plots, an understanding is gained of how the flow behaviour varies with flow rate and fluid properties. Although this is useful, it lacks the quantitative result that is desired for a detailed comparison.

To account for the various aspects of the device performance, multiple criteria are needed. By making the criteria more specific, the dependence of the criteria on the flow conditions is reduced. In this way, minor and frictional losses can be evaluated with separate criteria, developed to minimize the flow rate and viscosity dependence. In this study three new criteria are introduced that are designed to more closely match the ideal characteristics proposed above.

3.4 Pressure Loss Criteria

3.4.1 Criteria Derivation

The first two of these criteria are designed to evaluate the pressure drop performance of the ICDs. In designing these criteria, the goal is to isolate the effect of the flow rate and viscosity so that their effect can be evaluated separately. Although the loss equation is inadequate for precisely predicting the flow behaviour, it can be compared with experimental or simulated results to extract criteria from the results. Since these criteria are calculated from the actual results, they can be used to analyze the behaviour of a device.

In comparing the results with the loss equation, the effect of the viscosity needs to be accounted for separately. The viscosity of the fluid is a measure of the resistance of the fluid to shearing, or the diffusive exchange of momentum between layers of the fluid [24]. As the fluid flows through the device, this viscosity makes the fluid interact with the wall of the device to create a force that resists the flow. This contributes to the pressure loss in the device. As the viscosity of the fluid increases, so does the internal frictional loss of the fluid.

In equation 3.3 the frictional losses are included using the Darcy friction factor, f. This friction factor is a function of the Reynolds number of the fluid and the surface roughness of the device. For low Reynold number flow, the effect of surface roughness is small, and the friction factor can be expressed as a function of the Reynolds number [24]. For flow in the device the Reynolds number is given by $\mathrm{Re} = \rho u D / \mu$, where D is the minimum diameter in the device and u is the average velocity at this narrowest point. While there are models designed to accurately predict the friction factor [24], these are too complicated for this simplified model. To model the friction factor, an equation of the form $f = C/\mathrm{Re}$ is used.

This model corresponds to the friction factor for laminar flow, where $f = 64/\text{Re}$ [24]. Due to the range of flow rates in the device, this provides an adequate model for the friction factor, as shown in Appendix A. Inserting $f = C/\text{Re}$ into equation 2.19 gives

$$\Delta P = \frac{K_L \rho u^2}{2} + \left(\frac{\mu}{\rho u D}\right) \frac{CL\rho u^2}{D} = \frac{K_L \rho u^2}{2} + \frac{CLu\mu}{D^2} \tag{3.4}$$

By doing this, the two types of losses are separated in the two terms of the equation. The first term is the sum of the minor losses in the device and is proportional to the flow rate squared. The second term represents the frictional losses, and depends on the flow rate and viscosity. In order to isolate the effects of the flow rate and viscosity, the other quantities are combined into two coefficients. This simplified form of equation 3.4, expresses the losses as purely a function of the flow rate and viscosity with an equation of the form

$$\Delta P = C_1 u^2 + C_2 \mu u \tag{3.5}$$

where the coefficients give the sensitivity of the pressure drop to the flow rate and viscosity. The goal is for the coefficients in the equation to be independent of the flow rate, fluid properties, and scale of the device. To reduce this dependence, the two coefficients are examined separately to identify factors that affect the independence of the coefficients.

First the coefficient C_1 is examined. For this coefficient, the density of the fluid in the first term of equation 3.4 has been incorporated into C_1. This makes the coefficient dependent on the density of the fluid. To reduce this dependence, the density is extracted from the coefficient to make it independent of the density. Although no dimensions are included in the first term, the minor loss coefficients that make up K_L are often given as functions of the geometry. Since the type of minor losses depends on the design, this dependence cannot be further simplified.

In the second term of the equation, all the fluid properties have already been extracted from the coefficient. However, the coefficient C_2 does depend on the diameter and length of the device. As the goal is to make the coefficient independent of the scale of the device, the relation of these dimensions to the scale of the device must be examined. When sizing a nozzle or channel type design for a particular pressure drop, the diameter of the device is adjusted to give the desired value. To remove this dependence, the diameter of the device is extracted from the coefficient, C_2. When scaling the device, the length of the device is usually not changed. Thus, the length is left in the coefficient, as it is a component of the design and independent of the scale of the device. Applying these simplifications gives

$$\Delta P = C_1 \rho u^2 + \frac{C_2 u \mu}{D^2} \tag{3.6}$$

where the two coefficients now have a reduced dependence on the fluid properties and scale. To further improve these criteria, the coefficients should be adapted so they can be easily used in an optimization. For this, the criteria should have an optimum value of zero, so that

the best performance of the ICD occurs when the criteria are minimized. The best design for the criteria is determined by considering the contribution of each term of equation 3.6 to the pressure drop.

The first term of the equation is the sum of the minor losses and contains the effect on the pressure of the density and the square of the flow rate. As long as liquids are produced, the flow is incompressible and variations in density are minor. During regular production of oil, the flow rate is low. When flashing occurs or steam is produced the density drops significantly, decreasing the contribution of the first term. Although the production of fluid with low density and low viscosity increases the flow rate, the square of the flow rate in the first term grows rapidly, restricting the flow. While the second term also includes the flow rate, it does not grow as rapidly as in the first term and does a poorer job of restricting the flow. Thus, although the first term decreases when a low density fluid is produced, it is better at restricting the resulting increase in flow rate. In this situation, the ICD is intended to penalize this increase in the flow rate. For this term to be maximized, the coefficient should be moved to the denominator so that it can be minimized for the best results. Hence, the coefficient in the first term is defined as $C_{\mathrm{qfc}} = 1/C_1$, where C_{qfc} is called the quadratic flow coefficient.

The second term of the equation contains the contribution of the frictional losses to the total pressure loss. The factors influencing this term are the viscosity, flow rate, and diameter of the device. The effect of the diameter can be neglected, since this depends on the scale of the device and is not changed after the device is installed. Since the flow rate sensitivity is accounted for by the first term, it is not the dominant factor in this term. The focus is on the viscosity sensitivity of the device given in this term. For the best performance, the high viscosity oil is preferred over the low viscosity water or steam. Thus, to minimize the viscosity sensitivity, this second term should be minimized, and the coefficient should be left in the numerator.

An examination of the second coefficient reveals that it has units of length, since the length of the device was left in the coefficient. For the purposes of optimization and comparison it is desirable to have dimensionless criteria. To make this second coefficient dimensionless, a length needs to be extracted from the coefficient that is not an essential part of the design. Since this length is linked with the design of the ICD, another length is needed that is related to the scale of the device. For the tubing deployed ICD in this study, the device is fitted between an annular space and an inner pipe. If this gap were changed, the design of the device would have to be scaled accordingly to fit the gap. It is proposed that the length, L, be replaced with the scale of the device, as measured by the radial distance, δ, between the baseline of the entrance from the annular flow to the base line of the exit of the device into the inner liner. This radial distance is easily measured, regardless of the type of ICD.

The final form of the equation is then

$$\Delta P = \frac{\rho u^2}{C_{\text{qfc}}} + \frac{C_{\text{vis}} \, \delta u \mu}{D^2} \qquad (3.7)$$

where C_{qfc} is the quadratic flow coefficient and C_{vis} is the viscosity sensitivity coefficient. These two coefficients can be used as dimensionless criteria to optimize the design of ICDs. Each criterion characterizes separate behaviours of the device.

The coefficient C_{qfc} is related to the minor losses in the device and represents the sensitivity of the device to square of the flow rate. Although the focus of this criterion is on the flow rate, C_{qfc} is also related to the density. An inspection of equation 3.7 reveals that a low C_{qfc} value results in a high density sensitivity.

The second coefficient C_{vis} is related to the frictional, or major, losses in the device. This coefficient provides a measure of the sensitivity of the device to changes in viscosity. By deriving the coefficients in this way they are tied to specific aspects of the ICD performance.

3.4.2 Criteria Calculation

Equation 3.7 is only an approximate model for the flow behaviour of ICDs. To further reduce the dependence of these coefficients on the flow rate and fluid properties, the method of calculating these criteria is examined. Since there are two coefficients in the equation, at least two measurements are needed. Although the criteria are designed to reduce the dependence on flow rate and viscosity, there is still some dependence on these variables, especially for autonomous ICDs where the flow behaviour varies with the flow properties.

To reduce this dependence, it is proposed that they should be calculated from a set of measurements across the range of expected flow rates and viscosities. To extract the coefficient values from a set of more than two measurements, a curve is fitted to the data, using a least squares fit. For each coefficient a set of data is used that varies with the quantity of interest. For the quadratic flow coefficient the flow rate is varied and for the viscosity sensitivity coefficient, the viscosity is varied. A form of equation 3.7 is then fitted to the sets of data, and the two criteria are extracted from the coefficients of the fitted equations.

To calculate C_{qfc}, a set of simulations is performed with a fixed viscosity. Holding the viscosity constant in equation 3.7 gives a quadratic equation of the form $\Delta P = au^2 + bu$. Once this is fitted to the data, the coefficients are extracted from the fitted equation. Then C_{qfc} is calculated from the fitted coefficient a as

$$C_{\text{qfc}} = \frac{\rho}{a} \qquad (3.8)$$

For C_{vis}, a set of experiments or simulations is performed for a range of viscosities with a fixed flow rate. Holding the flow rate constant in equation 3.7 gives a linear equation of the form $\Delta P = m\mu + b$. Using this linear fit the coefficients are extracted for the pressure drop in terms of viscosity. Then C_{vis} is calculated from the coefficient m as

$$C_{\text{vis}} = \frac{mD^2}{\delta u} \tag{3.9}$$

By calculating the criteria in this way, the effect of the flow rate and viscosity on their respective criteria has been removed. But the effect of the viscosity on C_{qfc} and flow rate on C_{vis} needs to be tested. To test this for the quadratic flow coefficient, the criteria should be calculated with other viscosities. Then the criteria can be compared to determine the effect of the viscosity on C_{qfc}.

In the same way, the value of C_{vis} can be collected for other flow rates. The effect of the flow rate can then be calculated. Although this method of extracting the coefficient does not eliminate the dependence of the coefficients, it reduces the dependence of the criteria on the factors that most influence them. By reducing the dependence the criteria are representative of the devices performance.

3.5   Erosion Criterion

Another area of interest is the potential of erosion in the device. The main quantity of interest is the erosion rate in the device. While this can be calculated with detailed experiments, the complexity of measuring this value in this way means that the erosion is usually only calculated for one fluid, flow rate, and particle density [13, 38]. Simulations can provide detailed results, but are challenging to setup [34]. For a comparison of multiple ICD designs this method is expensive and does not test for flow rate and fluid property dependence. A simpler method, used by Zeng et al. [14], compared the maximum velocity to provide an estimate of the erosion rate. For this comparison, the devices were sized for the same pressure drop [14].

Although there are many factors that influence erosion, the two related to the flow are the impact angle and velocity. Even though the impact angle affects the erosion rate, the material used for the device changes the optimal angle [31]. Due to this dependence, a preferred angle cannot be determined independently of the material. When calculating the erosion rate, the impact velocity includes an exponent. The value of this exponent depends on the material [33]. Due to these numerous factors, the erosion criteria is not designed to provide a model for the erosion rate, but to provide a relative measure of the impact velocity. For this, the maximum velocity is used. For the criteria, the exponent on the impact velocity is neglected, as the criteria is only an approximation that allows the potential of erosion to be ranked. Also, by neglecting the exponent, the physical meaning of the velocity is retained.

Based on the maximum velocity, a third criterion is proposed for the erosion rate in the device. Because the erosion rate is directly related to the impact velocity, the maximum velocity in the device is used. Although not as accurate as the erosion rate, this provides a simple estimate of the erosion rate, since the erosion rate is proportional to the velocity

of the flow causing the erosion. The maximum velocity on its own is not sufficient, as it is directly related to the average flow rate in the device. Normalizing the maximum velocity by the average flow rate reduces the flow rate dependence giving

$$\overline{u_{\mathrm{max}}} = \frac{u_{\mathrm{max}}}{u_{\mathrm{ave}}} \tag{3.10}$$

This removes the flow rate dependence at each point. If the flow behaviour changes with the flow rate, the normalized maximum velocity, $\overline{u_{\mathrm{max}}}$ may still vary with the flow rate. To remove this dependence the normalized value is calculated from a range of flow rates. Using a linear fit of the form $u_{\mathrm{max}} = s\,u_{\mathrm{ave}}$, a line is fitted to the maximum velocity and average velocity data. The slope, s, of this fit provides a normalized value for this ratio.

This normalized value is by definition greater than one, since even a perfectly flat velocity profile gives a value of $s = 1$. For this criteria to be used in an optimization, it is preferable that the optimum performance occur when the criteria approaches zero. To achieve this one is subtracted from s, giving

$$EP = s - 1 \tag{3.11}$$

where EP is the erosion potential, expressed as a percentage. By defining the erosion potential in this way, it gives the excess flow of the maximum velocity, as a percentage of average velocity. This gives an ideal value of zero, where the flow would be evenly distributed across the device.

3.6   Conclusion

Three new quantitative criteria are proposed. First, the quadratic flow coefficient, C_{qfc}, that measures the resistance of the device to increases in flow rate. Second, the viscosity sensitivity coefficient, C_{vis}, that measures the ability of the device to maintain flow resistance at low viscosities. Third, the erosion potential, EP, that measures the risk of increased erosion from high velocity flows. The criteria are designed to have a reduced dependence on the flow rate, fluid properties, and scale of the device. This is achieved by carefully defining the criteria and their method of calculation. All three criteria are also designed to be dimensionless quantities that provide the best results, when they are minimized.

Chapter 4

Simulation Setup

To test the new quantitative criteria, a range of ICD designs is investigated, using CFD simulations. CFD modelling allows multiple devices to be easily tested with a wide range of flow conditions. Based on the simulations, details of the flow can be analyzed and the criteria can be calculated.

For the simulations ANSYS®CFX 17.1 is used [44]. One of the challenges with simulating multiple devices is the development of a suitable mesh for each design. This software is selected because of its advanced mesher to deal with the complex geometry of the ICD designs. It also provides an efficient solver that helps to reduce the simulation time for the large simulations [44].

4.1 Well Case

To derive the geometry and boundary conditions, a well case is considered. The well case consists of a 1000 m slotted liner with an inner tubing string containing 6 evenly distributed ICDs. The well is divided into three equally sized sections using packers placed between the slotted liner and the inner tubing. The dimensions of the slotted liner and inner tubing are given in Table 4.1. For the slotted liner .012" slots were used with 36 slots per ring.

Table 4.1: Well case.

Pipe	Outer Diameter	Inner Diameter
Slotted liner	8 5/8 in	7.921 in
Inner tubing	6 5/8 in	5.7 in

The ICD sizing is based on a device diameter cross-sectional of 3.8 mm. For the well case each location is considered to have two devices placed symmetrically on either side of the inner tubing. By using two devices the interaction of the devices can be considered, while limiting the computing cost. The geometry around the devices was based on a two nozzle device from RGL Reservoir Management Inc. To keep the devices as comparable as

possible, this surrounding geometry is used for all the devices that are simulated. Details of the geometry are given in appendix C.

For the boundary conditions the well production is assumed to be evenly distributed along the length of the well. In reality the production is uneven with areas of high and low production. For the sake of the simulations these uneven areas are represented by a low or high total production to derive the boundary conditions. Overall, approximate well production rates of 30 to 600 m^3/d are assumed [48–50]. Although the production rates vary, the flow rate through the slots in the vicinity of the device is held constant at 40 cc/h per slot [25]. For the simulations, a 381 mm section surrounding the ICD is used, so that five rings of slots are included, as shown in Figure 4.1.
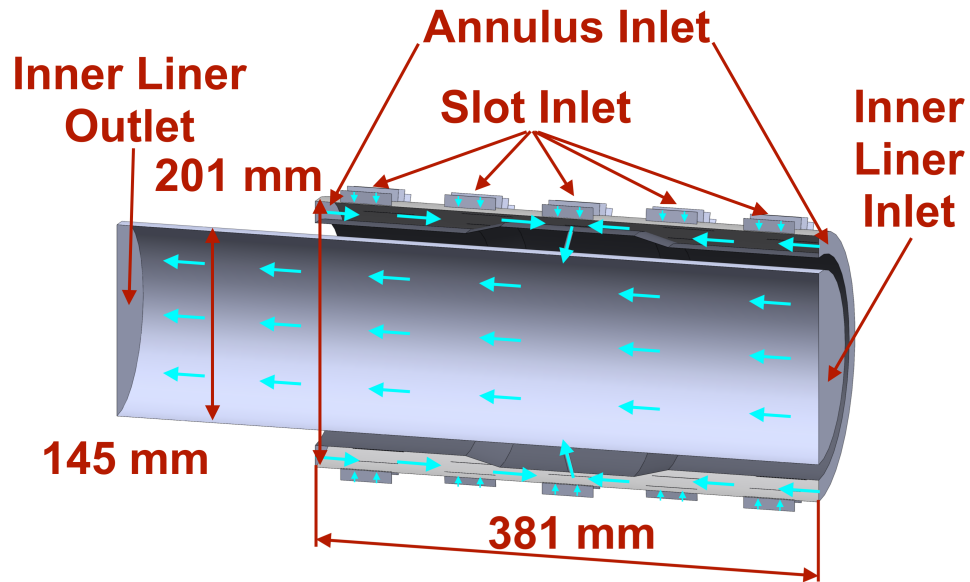
Figure 4.1: Boundary locations and dimensions.

Using this set of dimensions and flow rates, the boundary conditions are calculated, along with the average flow rate and Reynolds number in each region. The range of Reynolds numbers is calculated for a production range of 30 to 600 m^3/d with water having a density of 997 kg/m^3 and a viscosity of 0.8899 cP. The corresponding range of Reynolds numbers in the device is 11,201 to 216,900. For the simulations, the flow rate is adjusted to achieve a Reynolds number range of 10,000 to 210,000 for water.

For the given production range, the flow rate in the inner tubing is calculated to be up to 0.35 m/s, depending on where the device is located. When the device is closer to the toe of the well, less flow has accumulated in the inner tubing and the flow rate is smaller. For the simulations, the flow rate in the inner liner is fixed at an intermediate value of 0.18 m/s.

4.2 Simulation Geometry

To generate the geometry for the simulations, SolidWorks®2016 [51] is used, and the models are imported into ANSYS®. For the simulations the models are of the fluid rather than the solid materials. Thus, the models appear as a negative of a solid model of the device. Detailed drawings of the device geometry are given in Appendix C.

For the purpose of testing the criteria, a range of different types of ICDs need to be compared. By keeping the flow in and out of the devices as similar as possible, one can reduce the effect of outside factors on the comparison. To achieve this, the study is restricted to tubing deployed devices, where differences in the surrounding region are eliminated, so the devices can be more easily compared. All the differences between the devices are encompassed in the space between the annular region and the inner tubing. The geometry for the slotted liner, annular region, and inner liner are the same for all the designs. The regions surrounding the devices are shown in Figure 4.2.
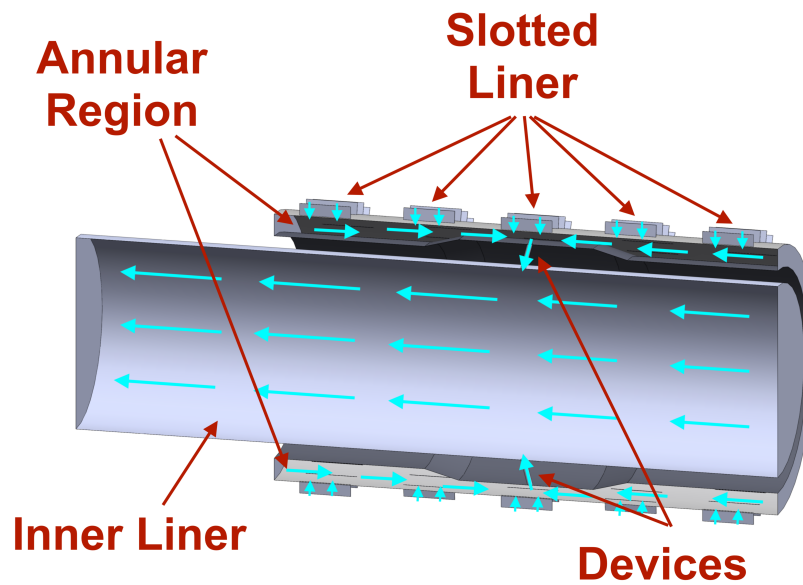
Figure 4.2: Flow regions.

For the geometry a slotted liner is used for the sand control. Although focus of the study is on the ICD, the slots are included in the model to account for any effect they may have on the flow into the device. When an ICD is placed in a well, its position relative to the slots is random. The slots in the well could be in any orientation relative to the ICDs. To maximize the effect the slots have, the liner for the model is oriented with a slot centred above each ICD. The slots for the model are 0.305 mm wide and 38.61 mm long. For the model five rings of slots are considered with 36 slots in each ring. The rings are spaced by

37.6 mm and the alignment of the slots is staggered so that alternating rings are aligned. This represents a typical slotted liner with a low slot density. The slot geometry is shown in Figure 4.3.
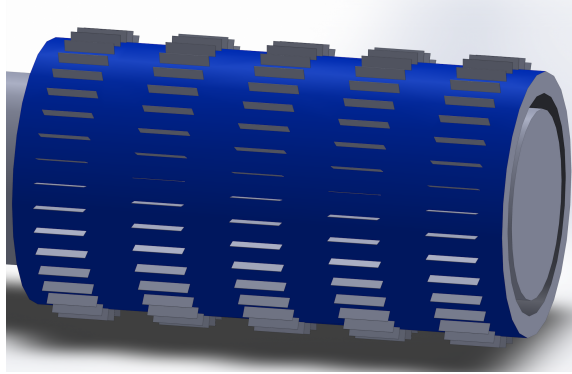

Figure 4.3: Slot geometry.

Although the annular space is fixed for most of the well, in the region around the ICDs the thickness of the inner liner increases to accommodate the ICD design. This thickening results in a gradual contraction of the flow in the annular region as it approaches the ICD. In the main portion of the well the annular gap is 16.46 mm. At the ICD this narrows down to 9.54 mm. The device is centred within this thickened section.

4.2.1 Passive ICD Geometry

For this study, four passive ICD designs and two autonomous ICD designs are considered. The geometry for the devices is given in Figure 4.4. For all the figures, the geometry is shown with the outlet on the left to match the convention for horizontal wells. First a basic nozzle design is considered, consisting of a short straight nozzle at an angle of 15° from vertical. The nozzle is directed in the downstream direction in the inner liner. This initial design is used as a basis for the grid and domain sensitivity analyses, when testing the simulation setup.

To make the geometry of the ICDs comparable, they are designed to be incorporated into the well in a similar way. For all the devices, the flow enters and exits the device in a similar way, although angles vary between designs. To make the pressure drop in the devices comparable, the minimum diameter of the devices is fixed at 3.8 mm. The only exception is the vortex device, where, due to size constraints, a diameter of 2 mm is used.

To investigate the effect of the nozzle angle, a second nozzle is modelled at a steeper angle of 40° from the vertical. By testing at these two angles the effect of the entrance and exit angles on the performance of the device can be investigated. For the basic nozzles the predominant losses are expected to be the minor losses at the entrance and exit of the device.
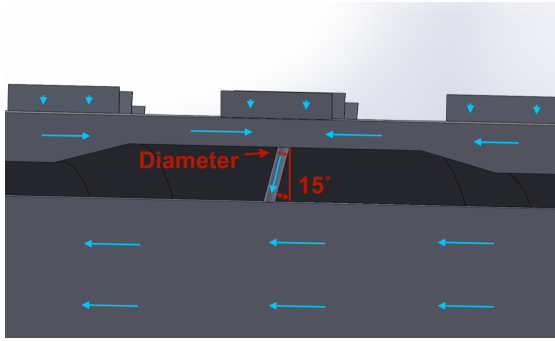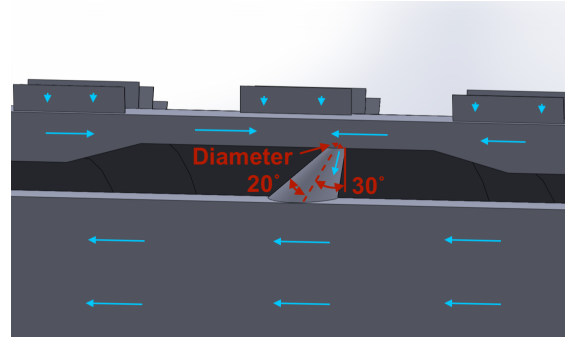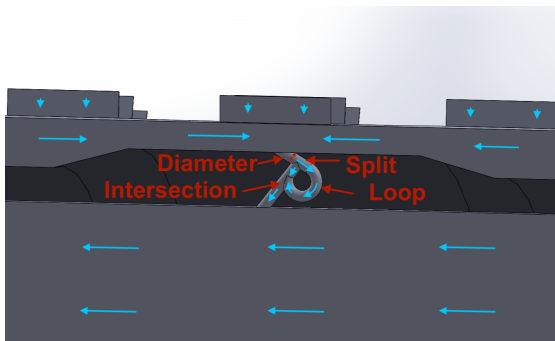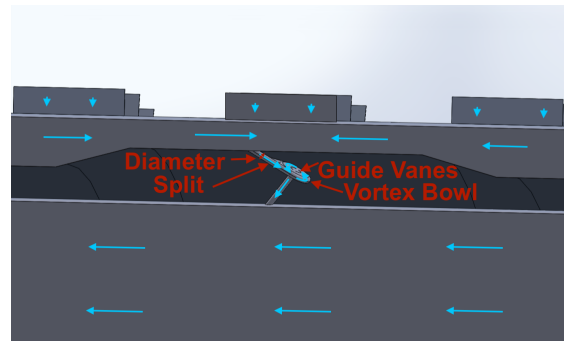
(a) 15° Nozzle.
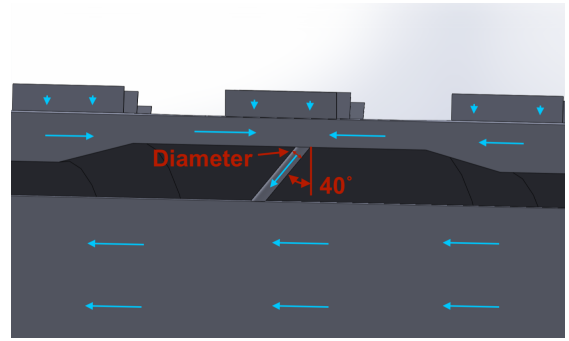
(b) 40° Nozzle.
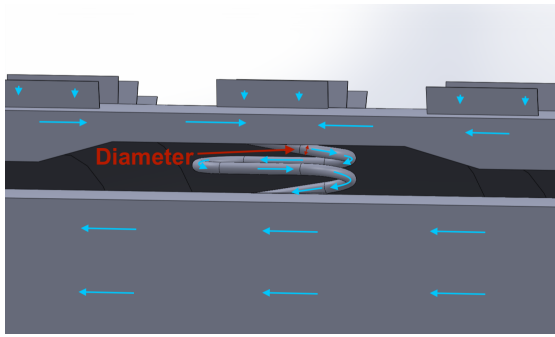
(c) Channel.

(d) Expanding nozzle.

(e) Diode nozzle.

(f) Vortex device.

Figure 4.4: Device geometry.

To create a device with large frictional losses, a long channel design is modelled. Typically long channel designs are found in liner deployed devices, where the additional space allows the channel to wrap around the pipe in a long helix. Due to the constraints of a tubing deployed device and to minimize differences with the nozzle design, an alternate design is introduced. To extend the channel, it winds down from the annulus to the inner liner, with long straight section in the axial direction as shown in Figure 4.4c. For this long channel design, the frictional losses are expected to be significant.

For the first three designs the nozzles and channel maintain a constant diameter along their length. But, another feature used in passive ICDs is an expansion in the device. To test the effect of an expansion, a nozzle is considered, with a $20°$ expansion, beginning at the entrance to the nozzle. This allows an investigation of the effect of an expansion on the entrance losses. So that the flow is still directed against the wall of the nozzle, the nozzle is angled at $30°$ from the vertical. This allows for a comparison of the exit and frictional losses in the expanding design with those in a straight nozzle.

For many passive designs, a series of nozzles and channels is used to control the flow [27]. By examining these basic designs independently, the flow in these elements can be understood. This knowledge can then be used to analyze combinations of these design features in more complex designs. This can also be used, when developing new designs based on these features.

4.2.2   Autonomous ICD Geometry

In addition to the passive designs, two autonomous ICD designs are also included. In these designs the flow behaviour changes with the flow rate, so the expected behaviour does not always follow the Bernoulli equation. This allows the proposed criteria to be tested for cases where the flow behaviour is unpredictable. The two autonomous ICD designs consist of a design based on Tesla's fluidic diode and a vortex based design.

For the Tesla diode design, a fluidic diode is placed in the reverse direction to create a large pressure drop. The geometry of the device is shown in figure 4.4e. In placing the diode device, the orientation of the device is selected to fit the diode in the small space, while maintaining a reasonable entrance angle. To achieve this, the entrance angle to the device is set at $60°$ from the vertical.

In designing this device a major consideration is the angle at which the channel splits. For the best performance the design should cause most of the flow to be directed into the loop. This results in an increased pressure drop, when the channels rejoin. For the split in the channel an angle of $98.9°$ is used. This large angle directs most of the flow into the loop. Details of the design optimization are given in Appendix D. Since this device is not being used as a diode, the flow in the reverse direction does not need to be considered. Another consideration in designing the device is the intersection angle at which the two channels rejoin. Based on the momentum balance around the intersection, a shallow angle directed

into the flow should create a large pressure drop. For the design an angle of 20° is used, with the orientation counter to the flow.

The second autonomous ICD design is the vortex design. For the vortex design the flow enters a straight channel that then splits with a branch at an angle of 60°. While most of the flow continues straight to produce the vortex, a portion of the flow is designed to enter the side branch, countering the vortex. For the best results, both branches of the channel then tangentially enter a circular vortex bowl [15]. To maintain the vortex flow, four guide vanes are placed in the vortex bowl surrounding the exit at the centre. For a better comparison with the diode design, the entrance and exit angles are identical for the two devices. The geometry for the vortex design is shown in Figure 4.4f.

For the simulations the geometry of the designs is defeatured by removing small complexities in the geometry that adversely affect the performance of the simulations, while not affecting the flow. With the exception of the channel, sharp edges are retained in the device, making the geometry similar to the condition of the ICD, when it is installed. As the device is used, erosion in the device rounds the edges in a device. These rounded edges change the behaviour of the device, usually resulting in a decrease in the minor losses [24]. For this study these geometry changes are not included in the designs.

4.3   Meshing

Due to the complex nature of the geometry in this study, the meshing is particularly challenging. A variety of different meshing strategies are needed to create the mesh. In addition to the complexities of the geometry, the size of the geometry provides a challenge. Because the surrounding region is included in the model, the mesh needs to conserve nodes where possible, so the size of the mesh can be kept small enough to allow for efficient simulations.

For the meshing, the advanced mesher provided in ANSYS®is used [44]. This mesher allows the geometry to be easily divided into multiple regions to facilitate meshing of complex regions. In these regions, mesh settings can be adjusted to achieve the method best suited to each type of geometry and flow. In the region surrounding the device, a tetrahedral mesh with refinement can capture the details of the flow. In regions where the geometry is simple and the flow is parallel to the walls, a uniform mesh can be used to conserve nodes. An example of the overall mesh is shown in Figure 4.5.

In the model there are 180 slots around the devices. Since the focus is not on the flow in the slots, it is important to limit the number of nodes in the slots. The slots are very narrow and a tetrahedral mesh would require a large number of nodes to capture the flow. Since the flow in the slots is parallel to the walls, a uniform mesh is used. Even with a uniform mesh, the automatic mesher produces a very detailed mesh. To produce a coarser mesh, the element size is prescribed with only five elements across the slot. This is adequate to model the inflow from the slots into the annular region, which typically has a very low Reynolds number. A cross-section of the mesh in the slots is shown in Figure 4.6.
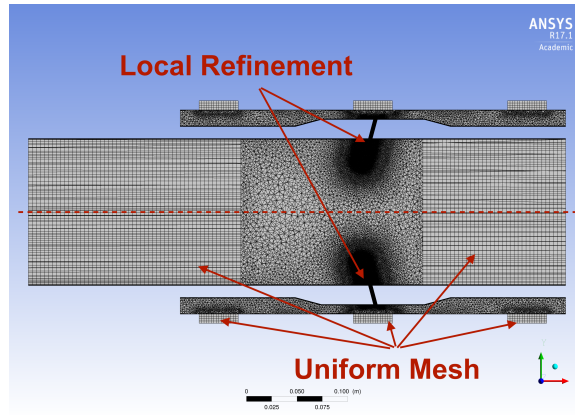
Figure 4.5: Cross-section of the mesh.

As the flow enters the annular region the mesh transitions to tetrahedral mesh. To avoid errors being introduced at this transition, it is important that the size and aspect ratio of the elements not change too rapidly. By using larger elements in the slots, the number of tetrahedral elements is reduced in the annular region.
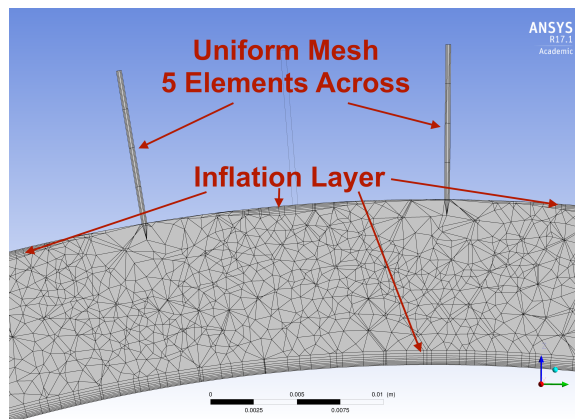

Figure 4.6: Cross-section of the mesh in the slots.

As the flow approaches the devices, the gradients in the flow increase. To capture this, the mesh gradually becomes finer close to the ICD. To produce this, several volumes surrounding the ICDs are used to refine the mesh in this region. Since the devices produce jets into the flow in the inner liner, sharp flow gradients and shear flows are expected as the jets enter the inner liner and are entrained into the main flow. To properly capture this flow, the refinement regions are extended to include the jet, downstream of the device. The mesh gradually transitions back to a coarse mesh away from the jets, as the flow gradients decrease. The resulting mesh around the 15° nozzle is shown in Figures 4.7 and 4.8.

Once the flow is far enough from the jets, the flow is predominantly a straight flow, aligned with the inner liner. Thus, in the inner liner, up and down stream of the influence
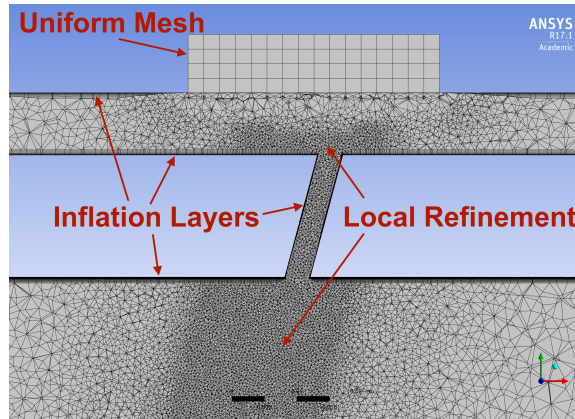
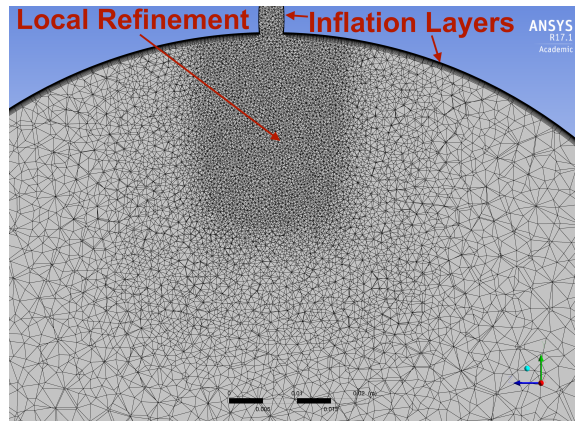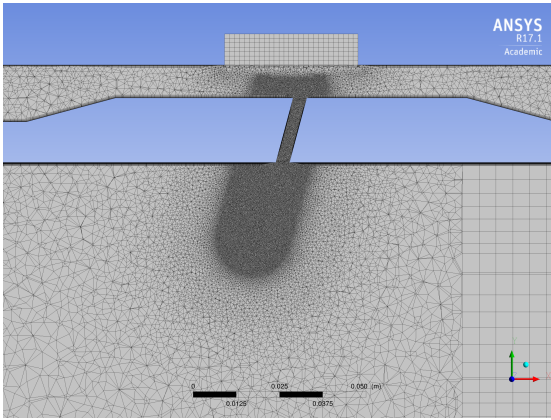Figure 4.7: Cross-section of the mesh in the 15° nozzle.

Figure 4.8: Cross-section of the mesh around the jet in the inner liner.

of the jets, a uniform mesh is used. This helps to reduce the number of nodes used in these large flow regions.

For the other ICD designs the refinement region around the device is adjusted to include the whole device. The refinement around the jets is also adjusted to match the direction at which the flow enters the inner liner. The mesh for all the devices is shown in Figure 4.9. For the more complex vortex based design, an additional refinement is made near the centre of the vortex, where the flow exits the vortex. Note, while the devices are all oriented in the same way, the direction of the x axis is reversed for the channel design as a result of the way the geometry was imported.
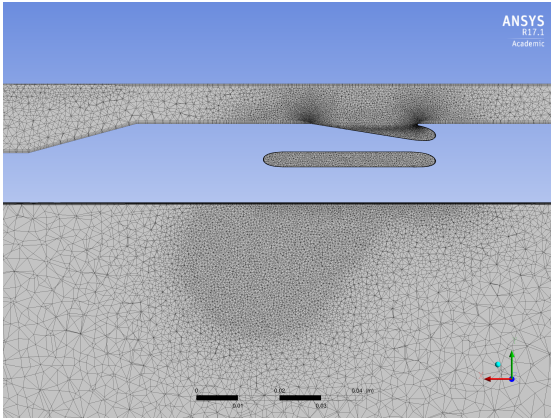
4.3.1 Inflation layer

To capture the boundary layer in the model an inflation layer is used at solid walls throughout the model. The inflation layer consists of several layers of thin elements parallel to the wall that are used to model the boundary layer in the near wall region. The mesh used in
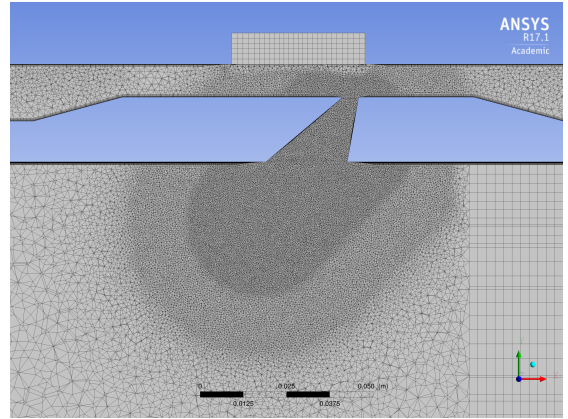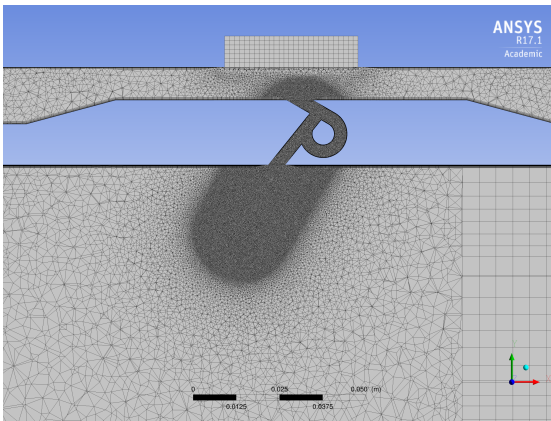
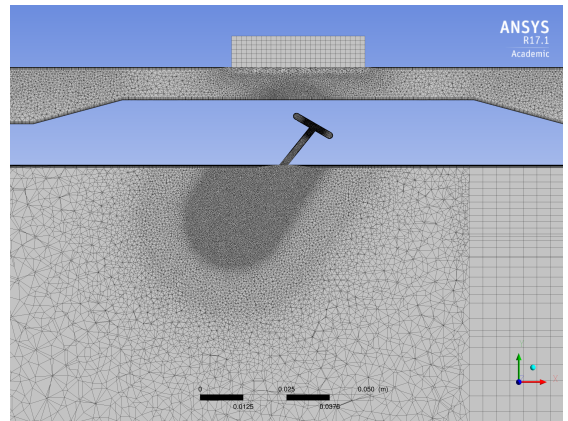(a) 15° Nozzle.
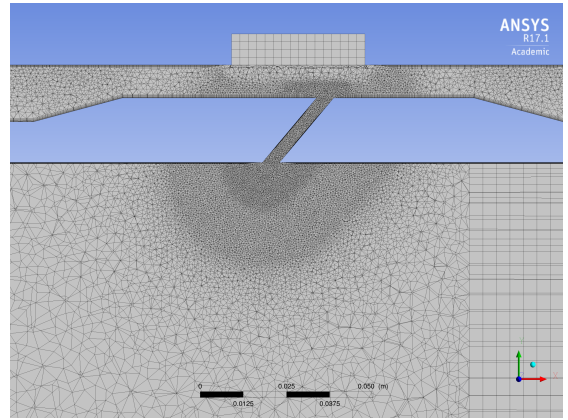
(b) 40° Nozzle.

(c) Channel.

(d) Expanding nozzle.

(e) Diode nozzle.

(f) Vortex device.

Figure 4.9: Cross-section of the mesh in the ICDs.

Table 4.2: Inflation layer.

Region	Number of Layers	First Layer Thickness	Growth Rate
Annulus	6	0.06 mm	1.2
Device	12	0.004 mm	1.2
Inner liner	10	0.02 mm	1.1

this model is designed to allow a low-Re wall model to be used. The low-Re model simulates the flow as laminar near the wall to capture the profile of the boundary layer.

For the low-Re model to work the first element in the inflation layer must be thin enough. The first layer thickness of the inflation layer is expressed by the Y^+ scale, where the first layer thickness is non-dimensionalized, using the shear rate and viscosity. To guarantee the low-Re model is used, the Y^+ value should be less than 3 [16]. Since the flow rate and boundary layer are different in each region, the inflation layer needs to be selected for each region based on the expected flow rate. The inflation layer sizing is given in Table 4.2.

For some of the meshes the inflation layer could not be generated near sharp corners in the design. At these features the inflation layer tapers down, restarting on the other side of the corner. This results in Y^+ values that are too high to use the low-Re model. To model these regions, ANSYS®uses a transitional model that approximates the expected boundary layer behaviour [45].

The resulting mesh for each design is used for all the simulations. Although the boundary layer thickness varies with flow rate, the inflation layer is designed to be appropriate for a range of flow conditions so the mesh can be used for a range of simulations. However, in some cases where the flow rate is high or the viscosity is low, higher Y^+ values can occur in the inflation layer resulting in the transitional model being applied.

4.3.2   Mesh Fineness

For the larger or more complicated ICD designs a larger number of nodes is used. The total number of nodes for each design are given in Table 4.3. In particular, the diode nozzle and vortex device use a refined mesh to capture the complexities of the flow. To ensure the mesh is sufficiently refined a mesh independence analysis is carried out in Section 4.11.2.

4.4   Boundary Conditions

Although the flow through the devices is a pressure driven flow, the pressure drop is unknown. For the simulations the inlet velocities are prescribed with a constant velocity. By setting the flow rate the source of pressure drop can be easily compared. It is expected that the results can be compared, as long the resultant pressure drop range is of the same order of magnitude. Since a top hat flow profile is used at the inlets, enough space is given in the

Table 4.3: Number of nodes.

ICD Design	Number of Nodes
15° Nozzle	3,199,329
40° Nozzle	3,903,497
Channel	5,291,223
Expanding Nozzle	8,425,140
Diode Nozzle	6,449,140
Vortex Device	16,744,674

model for an accurate profile to develop. The outlet of the model is set as a zero gradient boundary condition. All the walls are set to a no-slip boundary condition.

There are three inlet velocities to set for the model, the slot inlet, the annular inlet, and the inner liner inlet. A typical inflow rate for a single slot in a SAGD well is 40 cc/h [25]. For the slots in the model this corresponds to an inlet velocity of 0.94 mm/s at all the slots. This flow rate is used for all the simulations.

The velocity of the flow in the inner liner is determined by the amount of production from other devices upstream. For a device at the toe of the well this flow rate is negligible. A device at the heel of the well experiences the greatest flow rate. Based on typical production rates the inlet velocity varies up to 0.4 m/s. For most runs a velocity of 0.18 m/s is used. Simulations were also run with a velocity of 0.36 m/s to determine the effect of the inner liner flow rate on the simulations. The primary flow rate that is modified is the annular inlet velocity. By changing this velocity, the desired flow rate is achieved in the device.

At the outlet in the inner liner the boundary condition is set to a zero gradient, or zero average static pressure, boundary condition. This combination of boundary conditions provides the most stable setup for the simulations.

4.5 Domain

Because of symmetry in the design the initial simulations run using a quarter and half domain with one devices. It was found that the jet from the devices extends far enough to reach the centre plane between the devices. Since the jets from the two devices collide, a full domain is needed to capture the interaction of the two jets.

The extent of the domain must be sufficient to capture the flow. Because of the zero gradient boundary condition at the outlet, the outlet must be placed downstream where the flow is parallel. To ensure the outlet is far enough downstream, the domain in the inner liner is extended to test the sensitivity to the domain length. A domain length is then selected that does not effect the flow, while keeping the domain size small.

4.6   Advection Scheme

When simulating the flow, multiple schemes are available to discretize the advection. For the initial simulations, a first order upwind differencing scheme (UDS) is used to ensure convergence. Once the model is developed, the High Resolution scheme is used. This automatically blends the first order UDS scheme with the second order central differencing scheme (CDS). This is designed to keep the order of the error high, while avoiding the artificial oscillations associated with the CDS scheme. Since the order of the error in this method is unpredictable, it cannot be used when studying grid independence. To avoid this, a fixed blending factor is used for the study of grid independence.

4.7   Turbulence Model

For these simulations, the flow in the devices has a Reynolds number ranging from 1,000 to 1,868,000, based on the flow rates from the well case in Section 4.1 and a range of viscosities from 0.1 cP to 10 cP. For most of this range of Reynolds numbers the flow is expected to be turbulent. To select an appropriate turbulence model the type of flow features expected in the simulation are considered. The sharp edges at the entrance to the devices are expected to cause flow separation. As the flow enters the inner liner it produces a jet into the crossflow. Because of the flow separation the shear stress transport (SST) model is used, where a k-ω model near the wall is blended with a k-ε model in the free stream [45]. To test the turbulence model, simulations were also run with a transient SST model and scale adaptive simulation (SAS). The results were compared to ensure that the steady state SST model was adequate, except for the vortex cases. The test procedure is explained in detail in section 4.11.3.

4.8   Vortex Model

For the vortex case, with its complex flow, the choice of turbulence model must be reevaluated. Due to the smaller diameter of the vortex device, the Reynolds range in these simulations is from 2,000 to 3,551,000. Although the SST model is adequate for most simulations, a more advanced turbulence model is needed for the vortex case [16]. To capture the highly anisotropic turbulence in the vortex, two equation models are not sufficient [16]. Therefore, the full Reynolds Stress Model (RSM) is used in a transient simulation for the vortex case.

Before running the transient RSM turbulence model, the flow was simulated with a steady state SST model until the residuals levelled off. Then, this result was used as the initial condition for a transient model with the SST turbulence model. Finally, the RSM turbulence model was used, and the time step was successively decreased until the root mean square (RMS) residuals levelled off below 10^{-4}, and the monitoring points had levelled off

or started oscillating regularly. This procedure was necessary to avoid divergence. The resulting residual and monitoring point plots are given in Figure 4.10, where the solver iterations for each step are labeled. Successive vortex runs then used the result of this simulation as an initial condition.

4.9   Convergence Criteria

Two means are used to ensure the simulation are complete. First the root mean square (RMS) of the residuals from the momentum and continuity equations are monitored. These residuals are calculated from the iterative methods, used to solve the equations. As the equations converge to the solution, the residuals of the equations decrease. For an accurate solution RMS, i.e. the square root of the average of the residuals squared, is used as the norm to measure convergence. This is equivalent to the L_2 or Euclidean norm. For the simulations the residual RMS values are required to be below 10^{-4}. For most of the simulations the residuals oscillated between 10^{-4} and 10^{-5}. When possible the simulations were run until the residuals dropped below 10^{-5}. A typical residual plot is given in Figure 4.11a.

In addition to the residuals, monitoring points were placed in critical areas of the flow to track the flow velocity. The location of the monitoring points is shown in Figure 4.12. The values of the points are monitored during the simulation and the simulation is only stopped once they level off or oscillate regularly. A typical monitoring point plot is given in Figure 4.11b.

4.10   Measured Values

There are two values from the simulations that are of special interest, the pressure drop across the device and the maximum velocity. For these values to be comparable, they must be extracted in a consistent manner.

To measure the pressure drop the value of the pressure at two locations must be measured. Since the flow is different in each device the average pressure across the flow is used. In the annular region two planes are located on either side of the device to capture the upstream pressure. For the downstream pressure, a plane is placed two diameters downstream from the device. The pressure drop is determined by calculating the difference of the average pressure at these planes. To ensure the planes are far enough from the device, the range of pressure for each plane is checked. Since the range of pressures within each plane is less than 1% of the total pressure drop, the use of the average pressure is valid. This gives a consistent measure of the pressure drop that is independent of local variations in pressure.
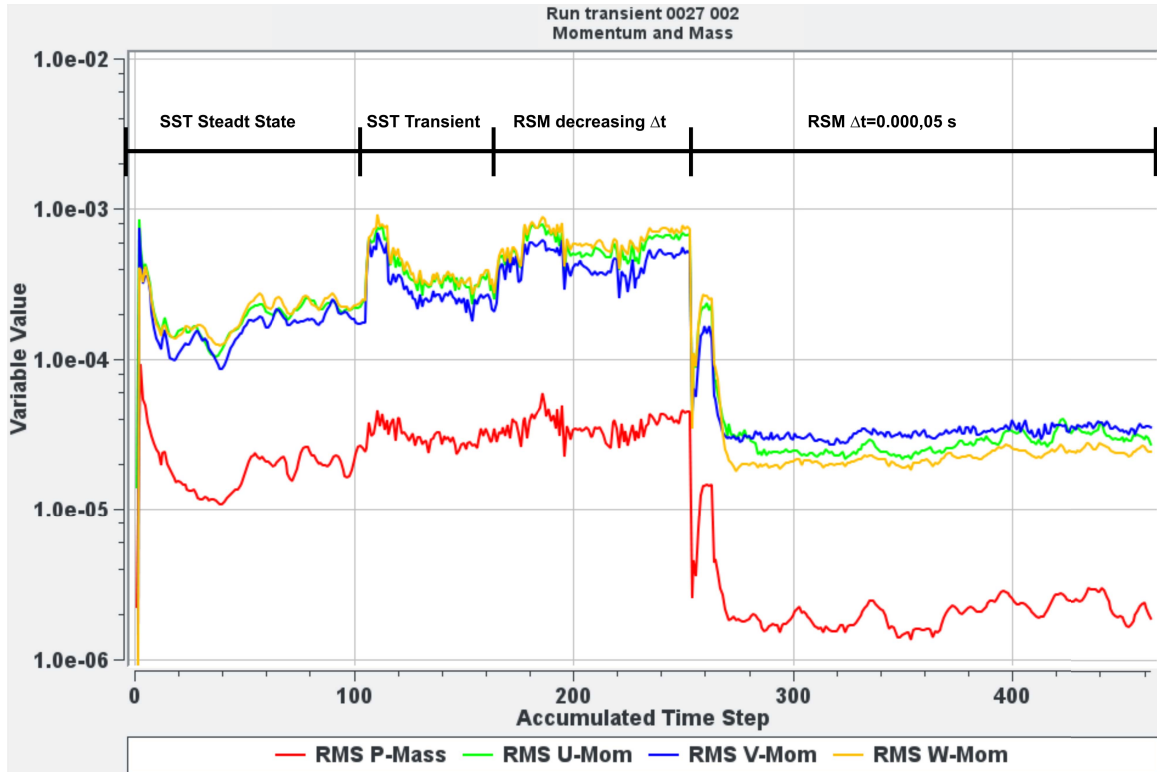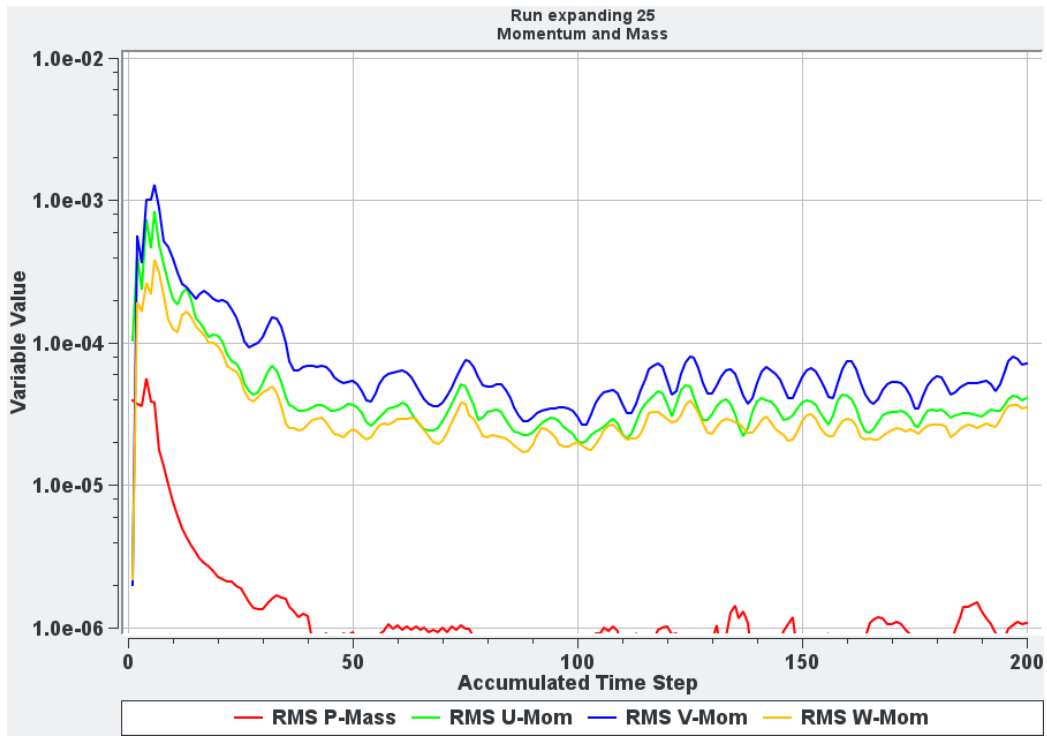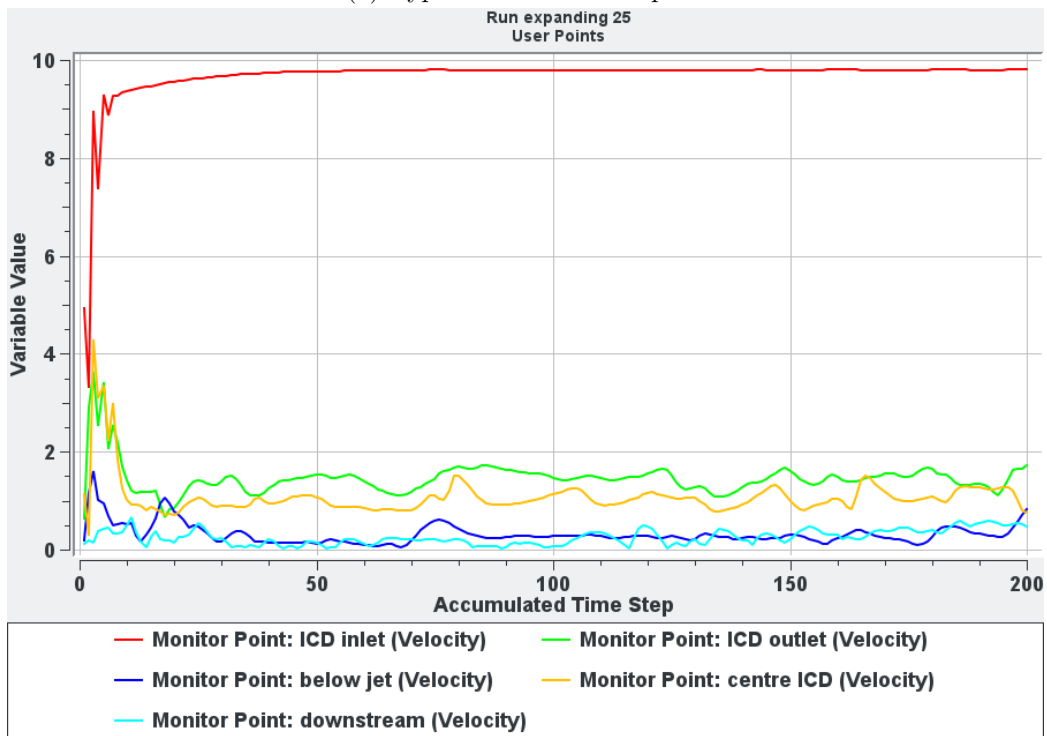
(a) Residual RMS plot for the vortex simulation.
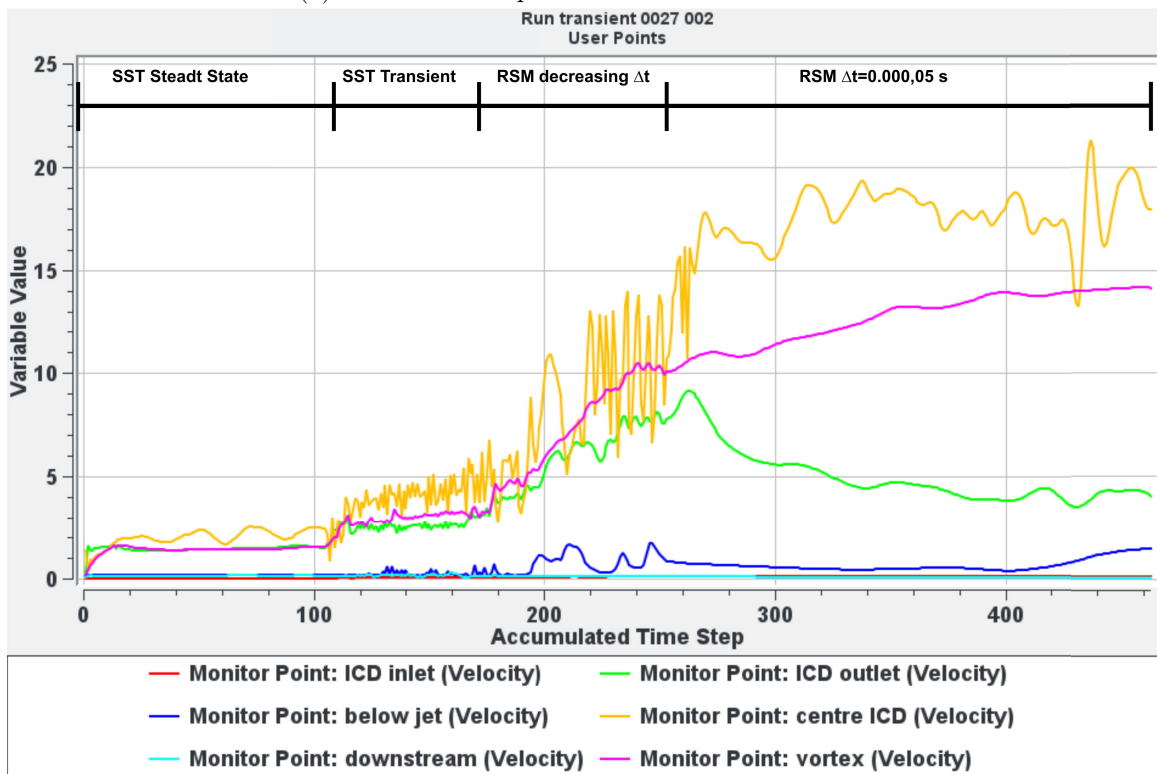
(b) Plot of the monitoring points for the vortex simulation.

Figure 4.10: Residual and monitoring point plots for the vortex device.

44

(a) Typical residual RMS plot.

(b) Typical plot of the monitoring points.

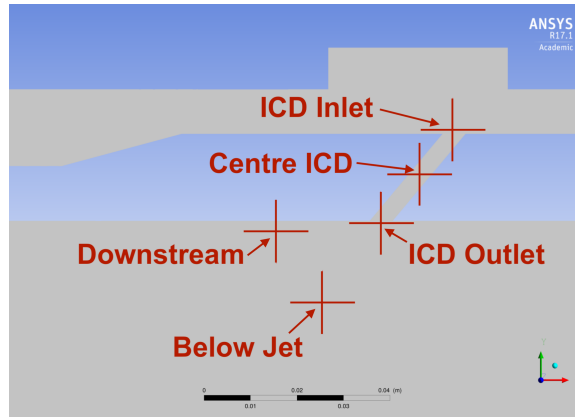Figure 4.11: Residual and monitoring point plots for a typical device.

Figure 4.12: Typical location of the monitoring points shown for the 40° nozzle.

The location of the measurement planes is shown in Figure 4.13. The upstream planes are 35.05 mm from the centre of the device, corresponding to halfway between the end of the central ring of slots and the end of the contraction in the annulus. The downstream plane is placed two inner liner diameters downstream of the centre of the device.
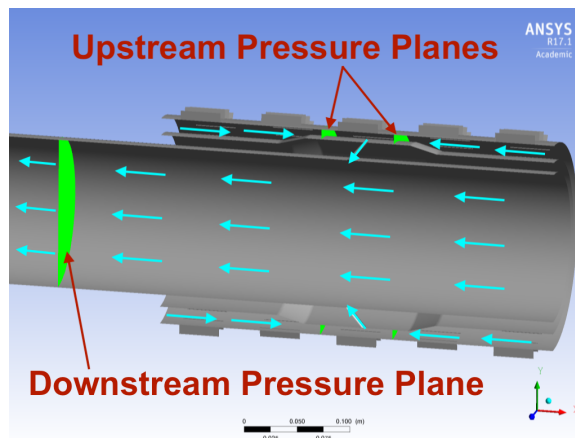

Figure 4.13: Location of plane for measuring pressure drop.

To measure the maximum velocity in the devices, the maximum velocity in the domain is extracted. Since the peak velocity always occurs in the devices, this corresponds to the maximum velocity achieved in either of the devices.

4.11 Model Independence

The focus for this study is on the local production defined by the annular flow rate and the fluid viscosity. But there are other factors that could affect the simulation results. To test the effect of these factors and make sure they do not affect the conclusions, a series of

sensitivity analyses are performed.

4.11.1 Domain Sensitivity

To test the domain sensitivity to the location of the outlet, a series of simulations is performed with the outlet placed successively farther downstream. The basic 15° nozzle model is used for the simulations and the boundary conditions are selected to match those for the highest flow rate simulation with an average velocity of 49.3 m/s in the device. For the initial run the inner liner was extended 150 mm beyond the end of the annular region. For each successive run this length was increased by a factor of 1.25 up to a length of 458 mm. The pressure drop for each simulation was measured and plotted against the domain length extension on a log-linear plot shown in Figure 4.14.
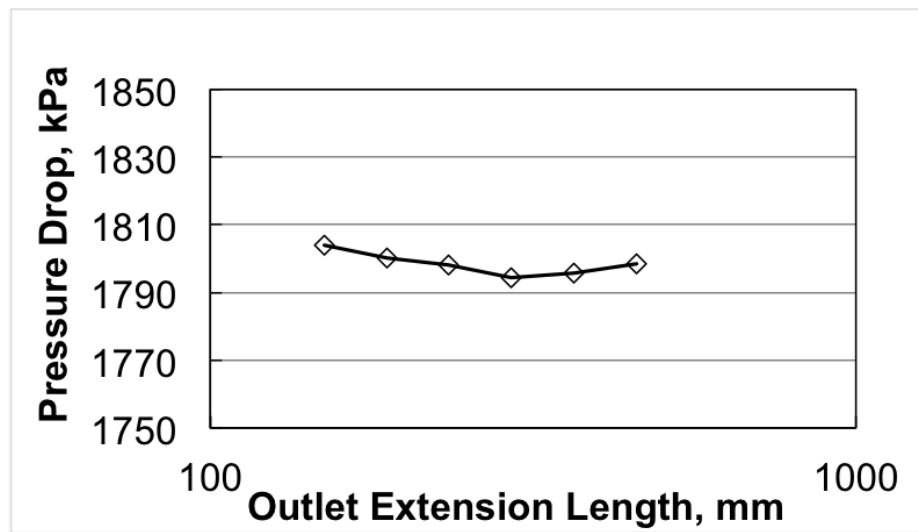

Figure 4.14: Log-linear plot of pressure drop versus inner liner domain extension.

Ideally the pressure drop should asymptotically approach a fixed value as the domain length is extended. In this case, the value varies up and down without approaching a fixed value. However, the total range of the values is only 0.5% of the original value. Thus, it is concluded that the domain length is sufficient and any variations are small enough that they will not significantly affect the result. For the other devices with more steeply angled exits the effect of the jet extends farther downstream. To allow for this, the extension length of 234 mm is selected.

4.11.2 Mesh independence

With a CFD simulation, one of the most important aspects to check is the mesh independence of the model. For testing the mesh the 15° nozzle model is used. To test for mesh independence, the mesh should be systematically refined or coarsened. Since a non-uniform mesh is used for much of the model, a consistent refinement is difficult to achieve. To force

47

the automatic mesher to refine the mesh consistently, each dimension and growth rate in the mesh settings is scaled by the same refinement scale. This method causes the mesh to be refined at approximately a constant rate across the whole mesh. Although a refinement scale is used to create the mesh, the resulting mesh typically has a different refinement rate that must be calculated from the number of nodes in each mesh.

For the mesh refinement, a refinement scale of 1.19 is used. This value is selected, as the mesh is already fine and does not allow for significant further refinement. Even with this rate the mesh exceeds 10 million nodes after two refinements. To obtain a fourth point, the mesh is coarsened once. Based on these four meshes, the average refinement rate is calculated as 1.16. The number of nodes and refinement rates for the meshes is given in table 4.4 along with the pressure drop and maximum velocity.

Table 4.4: Mesh size and refinement rates.

Number of Nodes	Refinement Rate	Average Pressure Drop	Maximum Velocity
3,691,887	N/A	2056 kPa	78.19 m/s
5,731,208	1.158	2064 kPa	79.02 m/s
9,115,658	1.167	2057 kPa	78.93 m/s
13,984,601	1.153	2060 kPa	79.74 m/s

For each mesh the pressure drop across the device is calculated. The pressure drop is then plotted against the number of nodes on a log linear plot, where the points are evenly spaced. The plot is given in Figure 4.15.
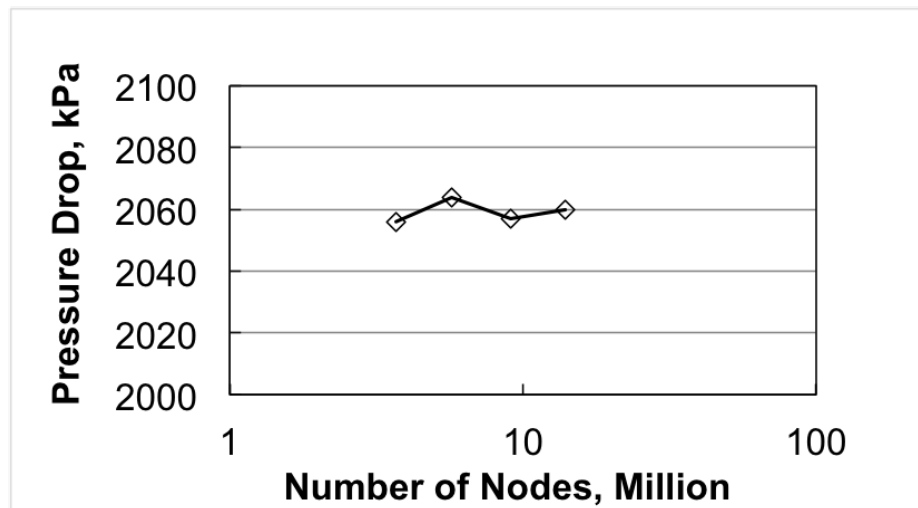

Figure 4.15: Log-linear plot of pressure drop versus number of nodes.

Comparing the variation with the grid, the pressure drop varies by 0.4% and the maximum velocity varies by 2.0%. Typically a pattern is looked for, where the points asymp-

totically approach a fixed value. In this case, while there is no asymptotic pattern, the variation in the points is small enough that the mesh is considered sufficiently refined.

4.11.3 Turbulence Model Sensitivity

To test the effect of the turbulence model on the results, simulation are run for the 15° nozzle with different turbulence settings. First, the simulation was run with the steady state SST turbulence model. Then a transient SST and a scale adaptive simulation (SAS) were run. The flow conditions were selected for a highly turbulent flow with an average velocity of 50.6 m/s in the device, corresponding to a Reynolds number of 215,524. The average pressure drop from the three simulations is given in Table 4.5.

Table 4.5: Turbulence model comparison.

Turbulence Model	Average Pressure Drop	Maximum Velocity
Steady state SST	1929 kPa	69.5 m/s
Transient SST	1941 kPa	69.6 m/s
Transient SAS	1940 kPa	69.8 m/s

For these turbulence models the SAS model is expected to provide the most accurate results followed by the transient SST simulation. Comparing these results with the steady state SST simulation reveals only a 0.6% change in the pressure drop and a 0.5% change in maximum velocity. Thus, for the purpose of this study, the steady state SST model is adequate. Since these simulations were for the 15° nozzle, the flow behaviour must be similar for this conclusion to hold. For the vortex design, the addition of the vortex means that the turbulence model needs to be reevaluated.

4.11.4 Low Reynolds Turbulence Sensitivity

The Reynolds number in the device is large, and turbulent flow is expected for most cases. But, upstream of the device in the annulus and slots, the Reynolds number is much smaller. For these regions, laminar flow is expected in the annulus, and creeping flow in the slots. In addition, with the addition of the crossflow, it is unknown if the jet exiting the device is turbulent or laminar. Since the flow behaviour at low Reynolds numbers in unknown, the validity of a turbulence model must be examined.

To investigate this both laminar and turbulent simulations are run for water at an average velocity of 2.35 m/s in the device. This corresponds to a Reynolds number of 10,000 in the device. For this comparison a 15° nozzle model was used. The resulting pressure drop values are given in Table 4.6.

Comparing these results the use of a laminar model results in less than a 1% change in the results. Any error arising from the use of a turbulence model does not significantly affect

Table 4.6: Low Reynolds turbulence sensitivity.

Turbulence model	Pressure drop	Maximum velocity
Laminar	4.86975 kPa	3.31 m/s
Turbulent SST	4.84391 kPa	3.28 m/s
Percent change	0.53%	0.93%

the result. Thus, for the simulations a turbulence model is used, even at lower Reynolds numbers.

4.11.5 Crossflow Sensitivity

Depending on where the ICD is located, the flow rate in the inner liner changes. The closer the ICD is to the heel of the well, the higher the flow rate. Simulations are run with a liner inlet velocity of 0.18 m/s and 0.36 m/s to determine if this flow rate in the inner liner impacts the flow behaviour in the device. For both cases nine simulations are run, and the pressure drop is evaluated. Then the quadratic flow coefficient, C_{qfc}, is calculated along with the erosion potential, and the viscosity sensitivity, C_{vis}, for a device average velocity of 2.35 m/s. A comparison of these values is given in Table 4.7.

Table 4.7: Crossflow sensitivity comparison.

Crossflow Velocity	C_{qfc}	C_{vis} for u=2.35 m/s	Erosion Potential
0.18 m/s	1.414	112.3	36.78
0.36 m/s	1.406	114.5	36.68
Percent change	0.56%	1.96%	0.27%

Comparing the results, the crossflow velocity appears to have little impact on the criteria. This is expected, since the flow exiting the device is significantly greater than the crossflow velocity. Thus, for this study a fixed inner liner flow rate of 0.18 m/s is used.

4.11.6 Device Orientation

When the ICD is placed in the well the orientation of the device is not consistent. Since the crossflow in the inner liner interacts with flow exiting the device, the effect of this orientation on the performance of the device is considered. For the comparison, simulations are run with the 15° nozzle oriented both directions, with the jet directed downstream and upstream. The three coefficients are then calculated, with the viscosity sensitivity coefficient calculated for an average velocity of 2.35 m/s. The resulting values are given in Table 4.8.

Based on these results, the performance of the ICD is not greatly affected by the orientation of the device. For the simulations in this study the devices are all oriented in the

Table 4.8: Orientation comparison.

Orientation	C_{qfc}	C_{vis} for u=2.35 m/s	Erosion Potential
Downstream	1.414	112.3	36.78
Upstream	1.401	113.3	36.34
Percent Change	0.92%	0.89%	1.2%

downstream direction.

4.12   Model Validation

To validate the simulations, the results should be compared to experimental or theoretical results. Due to the complexity of the geometry, an experiment of the flow through the device is beyond the scope of this study. For validation, a simplified portion of the geometry can be simulated using the same mesh, turbulence and other simulation settings. By comparing this simplified model to known experimental results, the simulation methodology can be partially validated for the complex simulations. For this validation, a simplified helical channel is compared to an empirical correlation regarding the frictional losses.

4.12.1   Helical channel validation

One of the important aspects of the simulations is the ability to accurately capture the frictional losses, especially in the long helical channel. For validation a simplified helical channel is modelled using the same mesh settings as for the channel device. In the actual channel device the channel alternates between a helical and a straight channel to maximize the length of the flow path. For the simplified model, a pure helical channel is used with the same diameters and pitch as that used in the channel device. The helix geometry and mesh are shown in Figure 4.16. Identical simulation settings are used and the simulations converged with a RMS residual of 10^{-5}.

   The helix geometry consists of three complete cycles. Based on an inspection of the velocity profiles the flow is fully developed by the end of the first cycle. The pressure drop in the helix is thus calculated across the last two cycles of the helix. For the validation three simulations are performed with water at the three flow rates used for the viscosity sensitivity calculations. These flow rates correspond to Reynolds numbers of 10,000, 110,000, and 210,000.

   The results of the simulations are compared to the expected flow structures in a helical channel. The flow in the helical channel produces dean vortices in the channel as described by Tang et al. [52]. The dean vortices consist of two counter rotating vortices in the channel. The size and location of these vortices depends on the flow and geometry of the channel. As the flow rate increases and the radius of the helix decreases, the two vortices move
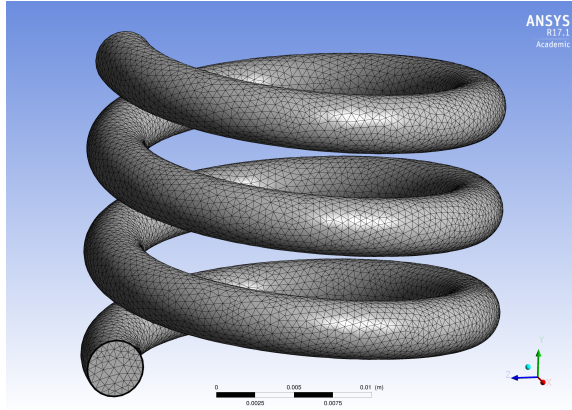
Figure 4.16: Simplified helix model and mesh.

symmetrically closer to the wall of the channel. The pitch of the helical channel causes the vortices to rotate from the vertical orientation found in channel with zero pitch [52]. This flow structure is captured by the simulation as shown in Figure 4.17. Due to the high flow rate the vortices are very close to the wall of the channel, while the pitch of the helix has caused a rotation of the location of the two vortices.
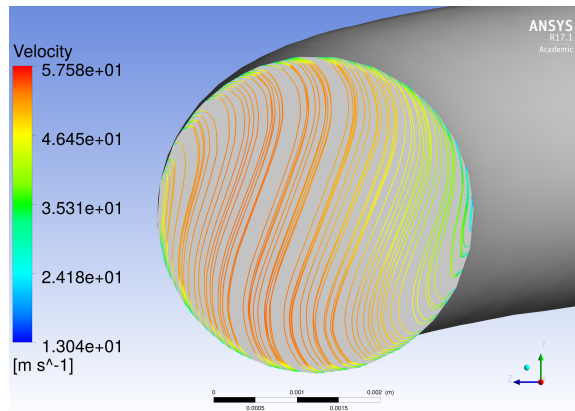

Figure 4.17: Streamlines showing the dean vortices in the helical channel.

To validate these results an empirical model is used to predict the pressure drop. The model gives the friction factor that can be used to determine the pressure drop in a helix. The typical friction factor is designed for a straight channel and is not accurate for a helical channel. For a helical channels a coil influence factor for the friction factor ($\mathrm{CIF_f}$) is used. This is defined as the ratio of the friction factor in a helical channel and a straight channel. To predict the $\mathrm{CIF_f}$, the correlation, proposed by Hayes and Park, is used [53]. This correlation is derived from the results of previous helical channel studies, using a least squares regression of the different models. The correlation is given as

$$\mathrm{CIF_f} = 1.07 + 0.0726 \, \mathrm{Re}^{0.278} \left(\frac{d}{D}\right)^{0.59} \tag{4.1}$$

where $\mathrm{CIF_f}$ is the ratio of the friction factor in a helical and straight channel, d is the diameter of the channel, and D is the diameter of the helix. When this is combined with a straight channel friction factor correlation, it gives the helical channel friction factor as

$$\mathrm{CIF_f} = \frac{1.07 + 0.0726 \, \mathrm{Re}^{0.278}(\frac{d}{D})^{0.59}}{[0.79 \log(\mathrm{Re}) - 1.64]^2} \tag{4.2}$$

This equation is used to predict the frictional losses in the helix. For the validation the error in the theoretical model is needed. Comparing the helical channel correlations, Hayes and Park found a 12 - 23 % deviation between the models. At lower Reynolds numbers the correlations are closer, but as the Reynolds number increases the correlation begin to diverge as shown in Figure 4.18. The results of the simulations and empirical model are given in Table 4.9.
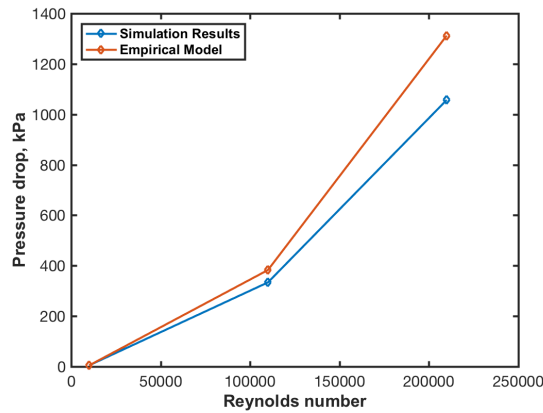

Figure 4.18: Plot of empirical and simulation values for pressure drop versus Reynolds number.

Table 4.9: Helical channel pressure losses.

Reynolds Number	CFD Pressure Loss	Empirical Pressure Loss	Percent Error
10,000	4.813 kPa	4.634 kPa	3.88%
110,000	333.7 kPa	382.7 kPa	12.8%
210,000	1057 kPa	1312 kPa	19.5%

Although the error is large at the higher Reynolds numbers, the pressure predicted by the simulations is within the range of deviation of the theoretical model. Especially at lower Reynolds numbers, the CFD simulations accurately predict the frictional losses in a long winding channel.

4.13   Conclusion

Now that a detailed CFD model has been created for each device, the models can be used to simulate the flow behaviour and calculate the criteria. The models have been checked to ensure they are independent of the grid, model settings, domain, and other boundary conditions. Finally, a simplified version of the model has been compared to empirical values to validate the model. The model can now be used with confidence to calculate the proposed criteria and analyze the behaviour of the devices.

Chapter 5

Results

By examining the results of the simulations the flow behaviour of the devices is understood. Using pressure contour plots, the major sources of pressure loss are identified. Velocity vectors reveal the areas with high erosion and the flow structures in the device. The results can also be compared to the flow structures predicted by the physics, providing qualitative validation of the simulations. Based on the results of these simulations the pressure drop and maximum velocity can be extracted from each simulation. Using these results, the three proposed criteria can be evaluated for each of the devices.

5.1 Simulation Results

Using the CFD model that has been developed, the results of the simulations are examined in each area of the domain, from the slots to the inner liner. In each area the flow structures are identified and compared to the expected result. The sources of pressure drop and erosion are also examined. For the devices, a side-by-side comparison is made of the flow. This is used to analyze the effect of the design features, such as the inlet angle of the device. For the autonomous designs, the particular flow features of the devices are examined, to understand the different pressure loss mechanisms.

5.1.1 Slot Flow

The first area that is examined is the inlet area in the slots. The mesh in the slots is coarse, with only five elements across the slot. To examine the flow the velocity profile in the slots is measured near the exit of the slot as shown in Figure 5.1. Although coarse, the mesh is able capture the symmetric velocity profile in the slot.

5.1.2 Annulus Flow

After exiting the slot, the flow in the annulus converges on the two devices included in the simulation. The streamlines in the annulus are shown in Figure 5.2. The flow evenly divides between the two devices, because the pressure differential across the devices is identical and
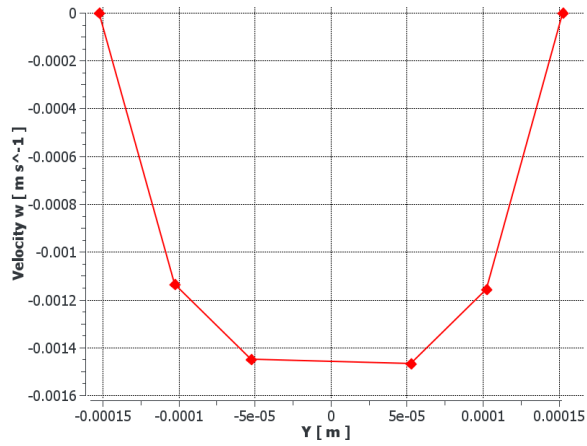
Figure 5.1: Velocity profile across a slot.

the geometry is symmetrical. As the flow approaches the devices, inflow from the slots and the contraction in the annulus cause the velocity of the flow to increase. Due to the large flow area the flow remains laminar in the annular region. The velocity profiles in the annulus are shown in Figure 5.3.
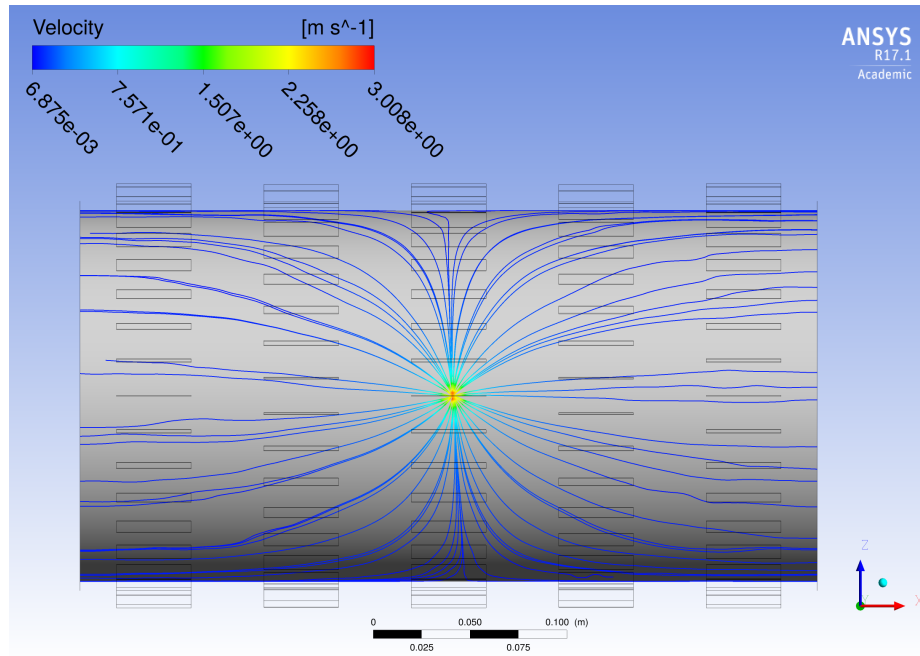

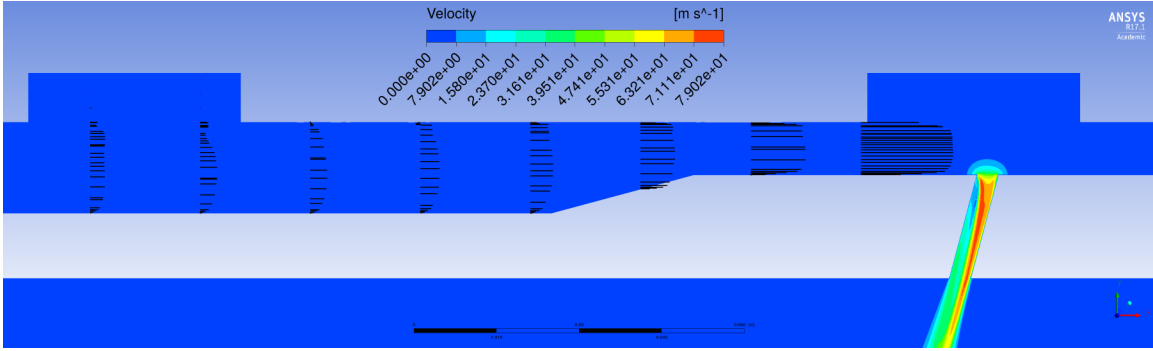Figure 5.2: Top view of streamlines in the annulus, converging on a device.

Figure 5.3: Velocity profiles in the annulus, approaching the device.
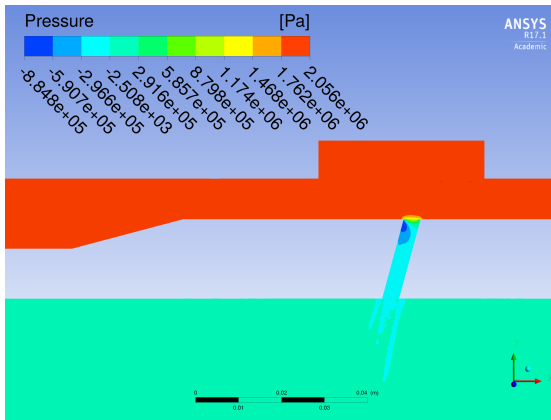
5.1.3 Pressure Contours

As the flow leaves the annulus and enters the device, the geometry change creates a pressure drop in the flow. This combined with the frictional and other losses in the device creates the pressure loss mechanism to control the flow. To understand the sources of this pressure loss, pressure contour plots for all the devices are compared. By examining these plots, the mechanisms for creating the pressure losses can be identified. This also allows an investigation of the effect of the design parameters on the pressure drop. The pressure contour plots for the devices are given in Figure 5.4. The simulations are for water with a flow rate of 20.71 m^3/d through the device. This corresponds to a Reynolds number of 171,000 for the vortex device and of 90,000 for the other devices. While, for comparing the devices a fixed colour scale is preferable, this is precluded by the range of pressure losses in the devices. The scale of the legend for each figure is based on the global pressure range.

An initial examination of Figure 5.4 reveals that, for most of the devices, the primary source of the pressure drop is the entrance loss of the device. Other sources include the frictional loss clearly visible in the channel and the special mechanisms in the two autonomous ICD designs.

Comparing the two straight nozzles, the entrance behaviour is similar. As the flow enters it creates a pocket of low pressure at the entrance of the device. Since the diameter of the devices is the same, the change in the pressure loss is the result of the entrance angle. As expected, the steeper entrance angle of the 40° nozzle results in a greater entrance loss. Although the 40° nozzle is slightly longer, this does not have a significant effect on the overall losses. Large entrance losses help to increase the minor losses in the device, resulting in an improved quadratic flow coefficient.

Comparing the nozzles with the channel again confirms the influence of a steep entrance angle on the entrance losses. As the flow enters the channel, the pressure drops rapidly. As the flow continues through the channel, the frictional losses further decrease the pressure. These increased frictional losses tend to make the device more sensitive to changes in the viscosity of the flow.
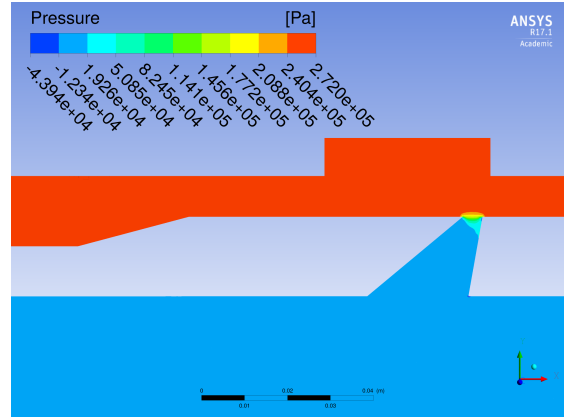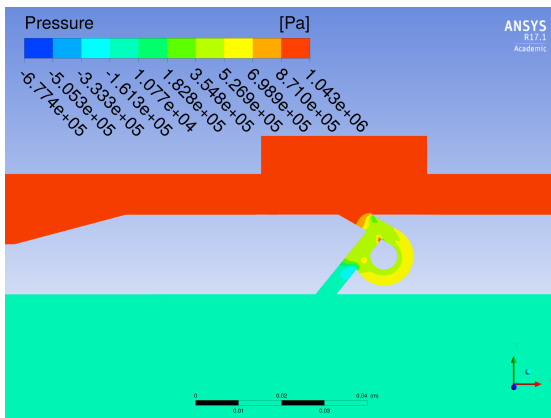
(a) 15° Nozzle with ΔP=353 kPa.
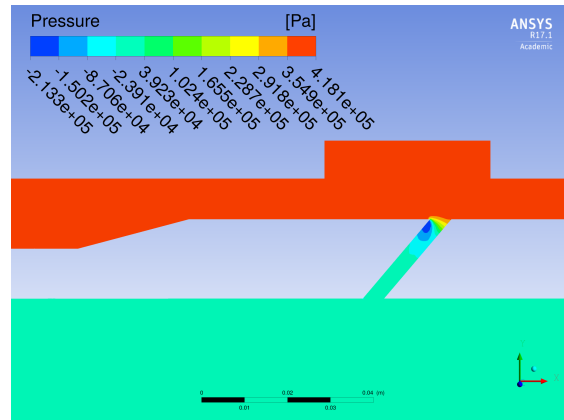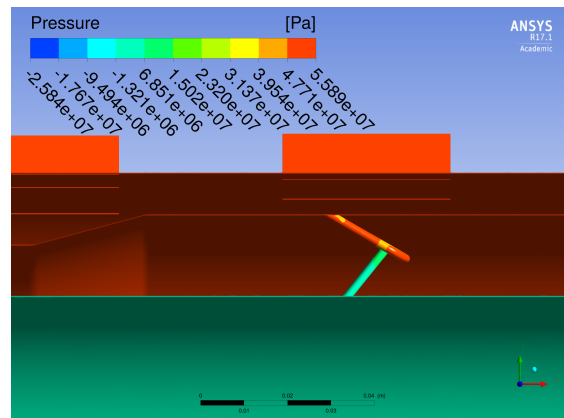
(b) 40° Nozzle with ΔP=418 kPa.
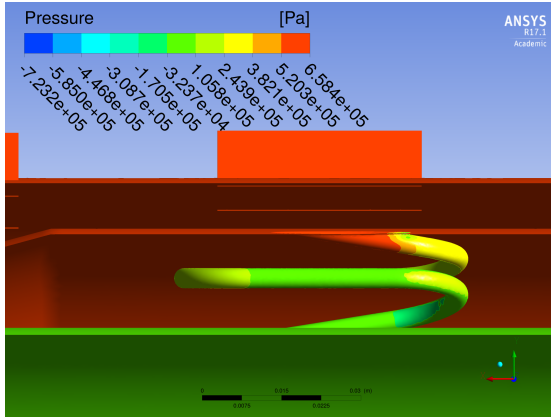
(c) Channel with ΔP=659 kPa.

(d) Expanding nozzle with ΔP=272 kPa.

(e) Diode nozzle with ΔP=991 kPa.

(f) Vortex device with ΔP=55,881 kPa.

Figure 5.4: Pressure contour plots in the devices for water with a flow rate of 20.71 m^3/d.

Next the expanding nozzle is compared to the two straight nozzles. Due to the expansion, a pocket of low pressure does not form in the same way. Although the entrance still provides the primary pressure loss, the overall pressure loss of the device is greatly decreased by the expansion. Avoiding the pocket of low pressure reduces the risk of cavitation at the entrance of the device.

A comparison of the passive and autonomous devices, reveals similar pressure drop behaviour at the entrance to the devices. But, for the two autonomous devices, a large portion of the pressure drop also comes from the pressure drop mechanisms peculiar to each device. This specialized behaviour will be examined in detail in sections 5.1.6 and 5.1.7.

5.1.4 Flow velocity

To identify the flow structures, it is important to look at the velocity vectors in the devices. The vector plots for the devices are given in Figure 5.5. By comparing these with the pressure contours, the flow structures responsible for the pressure drop can be identified. In addition, the vector plots help reveal the areas in the devices that are most susceptible to erosion.

Comparing the vector plot of the two straight nozzle with the pressure contours, reveals the source of the low pressure pocket at the entrance of the nozzle. As the flow enters the device, the flow around the sharp corner separates from the wall. This forces the flow to be concentrated against the opposite wall. This separation causes a low pressure recirculation region to form near the sharp angle. For the 40° nozzle, the sharper angle magnifies this effect, causing a larger recirculation region and more concentrated flow.

In examining the erosion in the devices, two types of areas are identified as areas of high erosion: first, areas near the wall with high velocity and second, areas with sharp curvatures in the flow, where particles will concentrate and the material will easily erode. As sand particles are carried by the flow, the concentration of the flow in these two nozzles would make the particles impact the wall, causing erosion. The flow would also tend to erode the sharp corner at the entrance, resulting in a rounded entrance with a decreased pressure drop.

Although only a portion of the velocity vectors for the channel are shown, the large recirculation region at the entrance is clearly visible. As expected, the sharper angle of the channel increases this effect. As the flow travels through the channel, it redistributes across the channel. For this device, the main erosion occurs at the entrance, where the sharp angle and concentrated flow trigger increased erosion.

For the expanding nozzle, the expansion keeps the flow from concentrating as quickly. Although the flow is forced against one wall, the maximum velocity stays small reducing erosion. As the flow enters, there is still a strong curvature, even though the low pressure pocket is not formed. Particularly at the sharp corner, the device will erode causing the
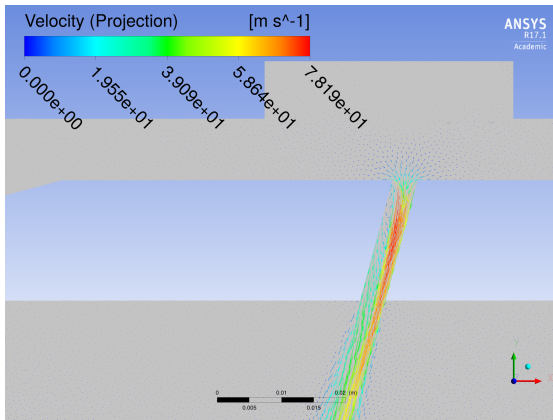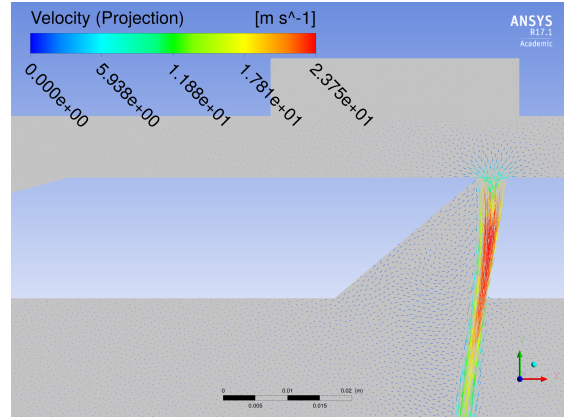
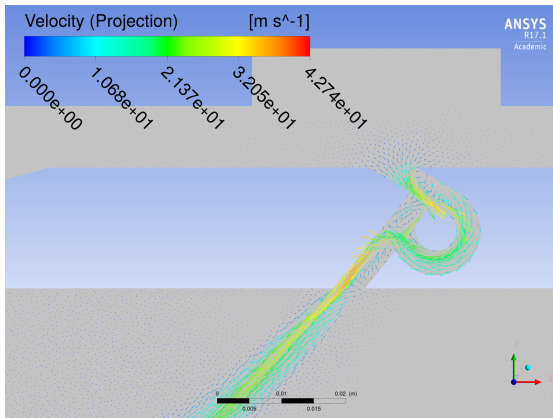(a) 15° Nozzle with $u_{\max}$=29.1 m/s.
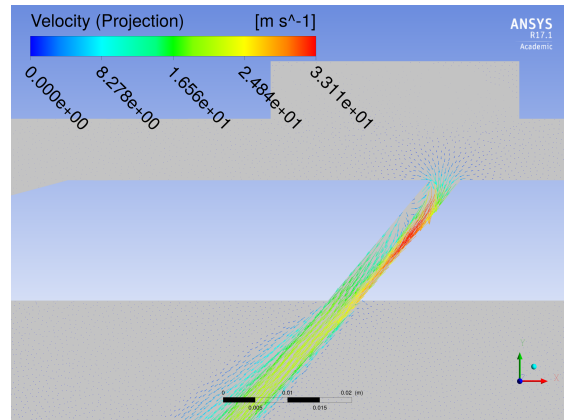
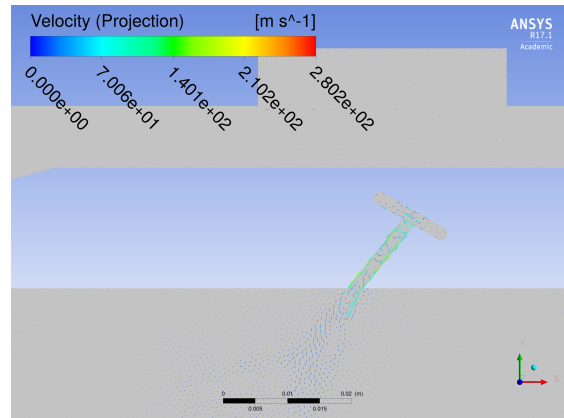(b) 40° Nozzle with $u_{\max}$=33.1 m/s.
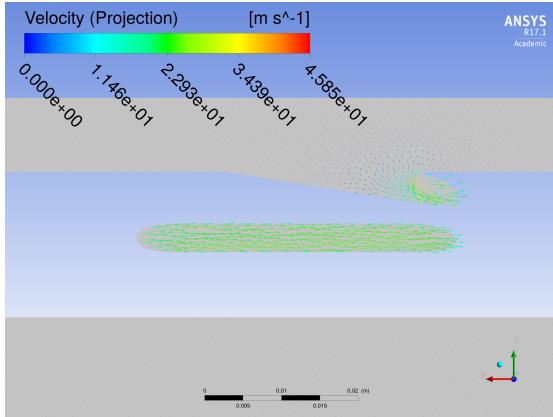
(c) Channel with $u_{\max}$=45.9 m/s.

(d) Expanding nozzle with $u_{\max}$=23.8 m/s.

(e) Diode nozzle with $u_{\max}$=42.7 m/s.

(f) Vortex device with $u_{\max}$=280.2 m/s.

Figure 5.5: Velocity vectors in the devices for water with a flow rate of 20.71 m^3/d.

opening to enlarge and the pressure drop to decrease rapidly. Since the flow is concentrated against one side, the rest of the device is filled with a slow moving recirculation region that extends into the inner liner. This means that the flow in the device is effectively only in contact with one side of the device, so that the frictional losses are greatly reduced.

For the two autonomous devices the entrance flow is similar, with a flow concentration and recirculation region. These flow structures extend downstream and affect the flow in the rest of the device, particularly for the diode nozzle. Further examination of the flow structures in these devices is detailed in sections 5.1.6 and 5.1.7.

5.1.5 Exit jet velocity profile

As the flow exits the devices it forms a submerged jet in the inner liner. To examine the jet, the profile of the vertical component of the velocity is measured at the exit of the device. The jet velocity profiles for the devices are given in Figure 5.6.

The flow exiting both the straight nozzles is asymmetrical with the majority of the flow on the right side of the nozzle. This is a result of the flow being forced against the far wall as it enters the device. Since the device is short, there is not enough time for the flow to redistribute across the device. For the 40° nozzle the magnitude of the velocity is smaller, as the device is at more of an angle than the 15° nozzle.

For the channel device, the flow has had time to redistribute across the channel. The slight predominance of the right side is a result of the downward momentum in the winding channel. For the expanding nozzle the exit is much wider than the other designs. The jet of flow out of the device is concentrated in a peak on the right side of the device. For much of the device the flow is into the device as the recirculation region pulls flow from the inner liner into the device.

For the diode nozzle, the flow exiting the loop pushes the flow to the left side of the device. The rest of the opening is on the edge of a recirculation region in the device, formed by the intersecting channels. For the vortex design the velocity profile of the vortex remains as the flow exits the device. This results in high velocity flow around the outside, while the low pressure in the centre of the vortex results in a lower velocity. To understand the flow in these autonomous designs the flow mechanisms are investigated separately.

5.1.6 Diode nozzle

To create the pressure drop in the diode nozzle, the device uses a split in the channel to divide the flow into two separate channels. The channels are then recombined, with the primary flow directed back toward the entrance. A close up of the flow in the diode is given in Figure 5.7.

As observed in Section 5.1.4, the sharp entrance angle forces the flow against the bottom wall as it enters the device. For the diode this results in more of the flow being directed into the side branch. This reduces the ability of the device to produce the pressure drop,
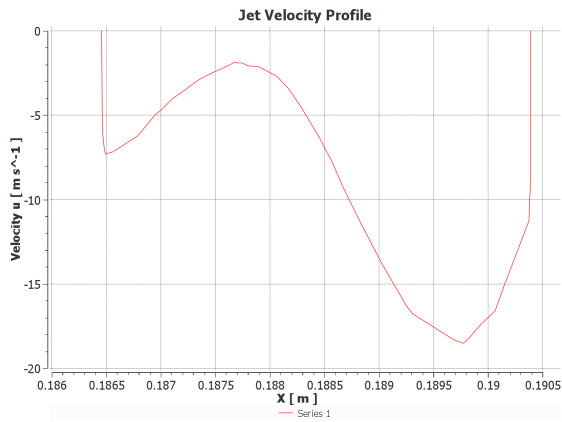
(a) 15° Nozzle.
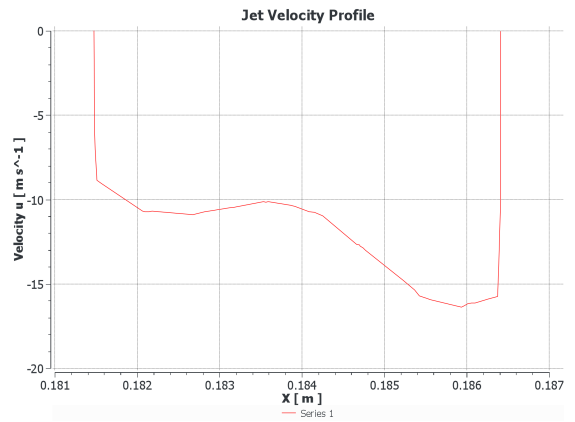
(b) 40° Nozzle.
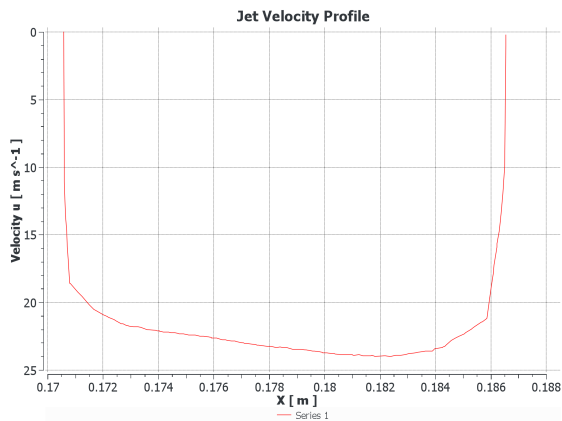
(c) Channel.
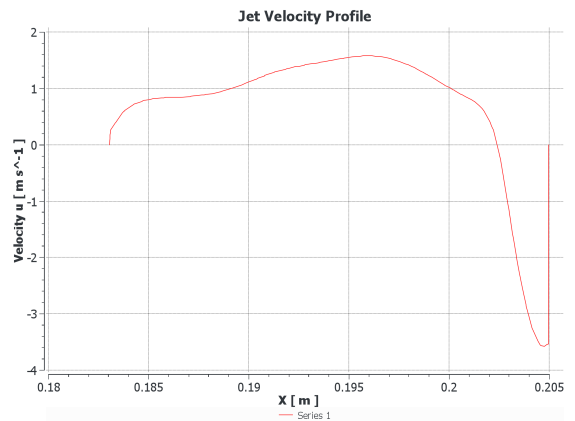
(d) Expanding nozzle.
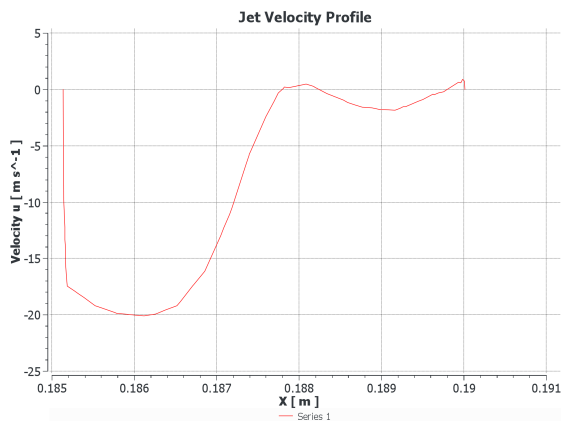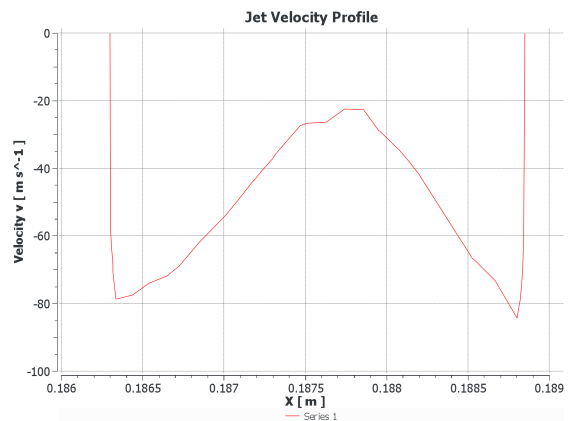
(e) Diode nozzle.

(f) Vortex device.

Figure 5.6: Velocity profile of the downward velocity of the jet at the exit of the devices for water with a flow rate of 20.71 m^3/d.

(a) Velocity vectors in the diode nozzle.

(b) Streamlines in the diode nozzle.

Figure 5.7: Velocity of the flow in the diode nozzle for water with a Reynolds number of 90,000.

since the device relies on the flow in the loop to create the losses.

The pressure drop at the intersection of the channels is the primary source of pressure losses in the device. Two mechanisms are involved in creating the pressure drop. First, the momentum of the flow entering the intersection creates a pressure drop [23]. This can be observed by applying conservation of momentum a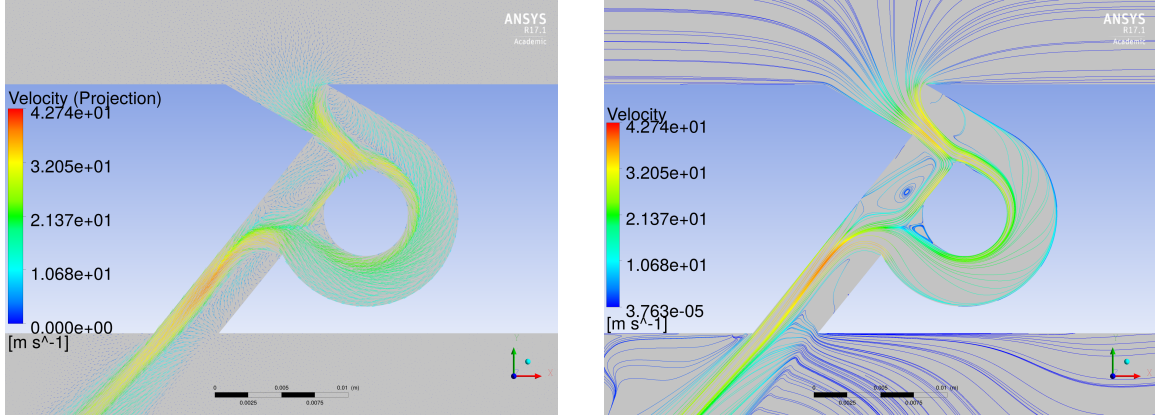round the intersection. Since most of the flow is in the loop, the momentum of the flow entering the intersection causes significant momentum in the upstream direction. To balance this momentum, a large pressure drop is created across the intersection.

The second mechanism is the contraction of the flow downstream of the intersection [23]. As the flow exits the loop, the jet of fluid forces the flow against the far wall, creating a recirculation region near the exit of the device. This contraction of the flow adds to the pressure losses created by the momentum imbalance.

5.1.7 Vortex device

For the vortex device the primary pressure loss comes from the vortex. To control the strength of the vortex, the channel is split, with part of the flow directed to counter the vortex. The primary flow remains straight and tangentially enters the circular region, or vortex bowl. The flow and pressure in the vortex are shown in Figure 5.8.

As the flow approaches the centre of the vortex, the velocity of the flow increases. This increase in velocity causes the pressure of the fluid to drop. In order to guide the flow, vanes are added around centre, inline with the flow direction. As the flow exits the device, it continues to rotate as it enters the inner liner, resulting in the profile shown in Figure 5.6f. The vortex in the device is a natural vortex and should have the profile of a compound or Rankine vortex [28]. To compare the profiles, the velocity and pressure along the line in Figure 5.9b are plotted with the same orientation. The profiles are given in Figure 5.9.
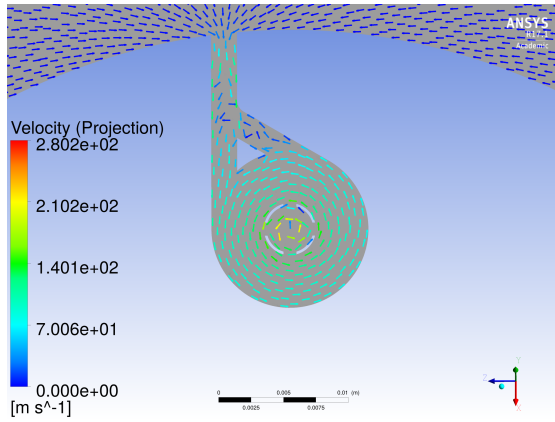
(a) Velocity vectors in the vortex device.
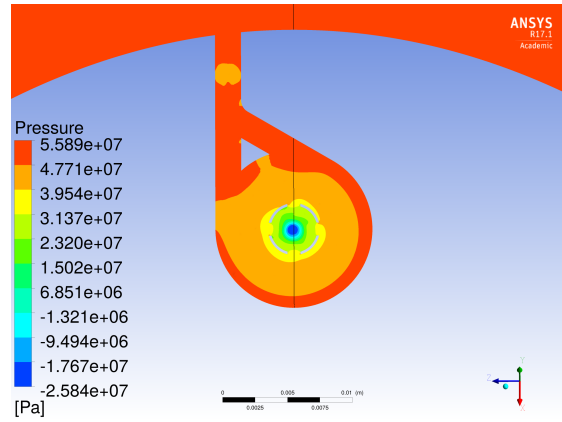
(b) Pressure contours in the vortex device.

Figure 5.8: Streamlines and pressure contours in the vortex device for water with a Reynolds number of 171,000.
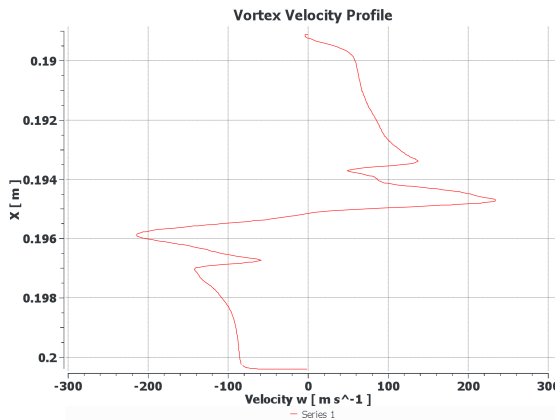
(a) Velocity profile across the vortex.
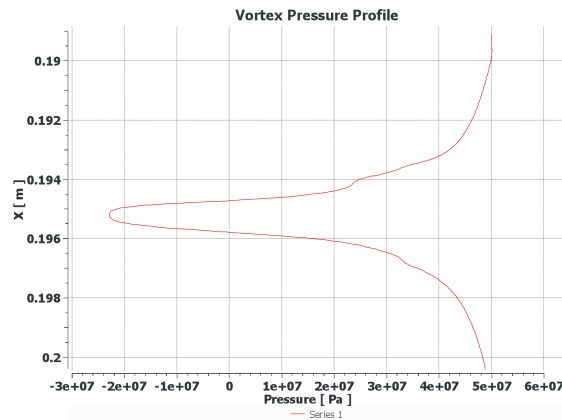
(b) Pressure profile across the vortex.

Figure 5.9: Profiles across the vortex device for water with a Reynolds number of 171,000, corresponding to the line in Figure 5.8b. Interruptions in the profile are caused by the guide vanes in the device

As expected for a Rankine vortex, the velocity increases rapidly as it approaches the centre of the vortex. In this region, the fluid acts irrotationally. But, at the core of the vortex, this condition can no longer hold, and the core rotates as a solid body. This causes the velocity to vary linearly across the core as it goes from one extreme to another. The velocity profile closely matches this, with only breaks where the vanes interfere with the flow. At the bottom of the profile a boundary layer is formed. At the top of the profile, the inflow from the side branch causes a slight back flow, but quickly reaches the expected profile. For the pressure contour the pressure is expected to rapidly drop at the centre of the vortex, due to the high velocity. This is clearly shown by the pressure profile.

For the vortex simulations the same flow rates are used as in the other simulations. However, the pressure losses are so large that an actual device would have a larger diameter or slower flow rate. Since the flow is pressure driven, the flow rates and pressure losses in these simulations are unrealistically high. In spite of these exaggerated conditions the flow matches the expected behaviour and is cautiously used in the analysis.

5.1.8   Inner liner flow

Once the flow exits the device, the jet of fluid is entrained into the flow in the inner liner. The interaction of a submerged jet with a crossflow has previously been studied [29, 30]. Based on this research, the expected flow structures can be predicted. As the jet initially enters the crossflow it behaves like a cylinder, causing the inner liner flow to pass around the jet. This creates a force on the jet that turns it in the direction of the main flow. However, this force is not strong enough to be the sole cause of the rapid entrainment of the jet [29, 30].

For a jet entering perpendicularly into the flow, the main flow passing around the jet would induce two counter rotating vortices in the jet. These vortices would pull flow from the crossflow into the downstream side of the jet. However, for the present simulations the ratio of the jet velocity to the crossflow velocity is large, ranging from 13 to 274 and the jet is angled in the downstream direction. For $r \gg 10$, the flow initially behaves like a free jet, independent of the crossflow [29, 30]. In addition, due to the angle of the jet, the downstream velocity component of the jet is greater than the crossflow velocity, even for the 15° nozzle. For the simulations, the jets behave as free jets and collide before vortices can form in the jets. This collision of the jets causes the flow shown in Figure 5.10. Since the simulation perfectly aligns the jets, they produce symmetric results. Upstream of the jets, the crossflow is blocked by the jets, causing vortices to be formed upstream of the jets.

To investigate the interaction of the jets, the velocity profile is measured at the lines shown in Figure 5.10. The lines are placed at intervals of half a diameter downstream of the device. The velocity profiles are shown in Figure 5.11. Initially the combined jets cause a strong peak in the centre of the profile and recirculation on either side. As the jets are entrained into the flow, the peaks combine and decrease as the flow approaches a fully
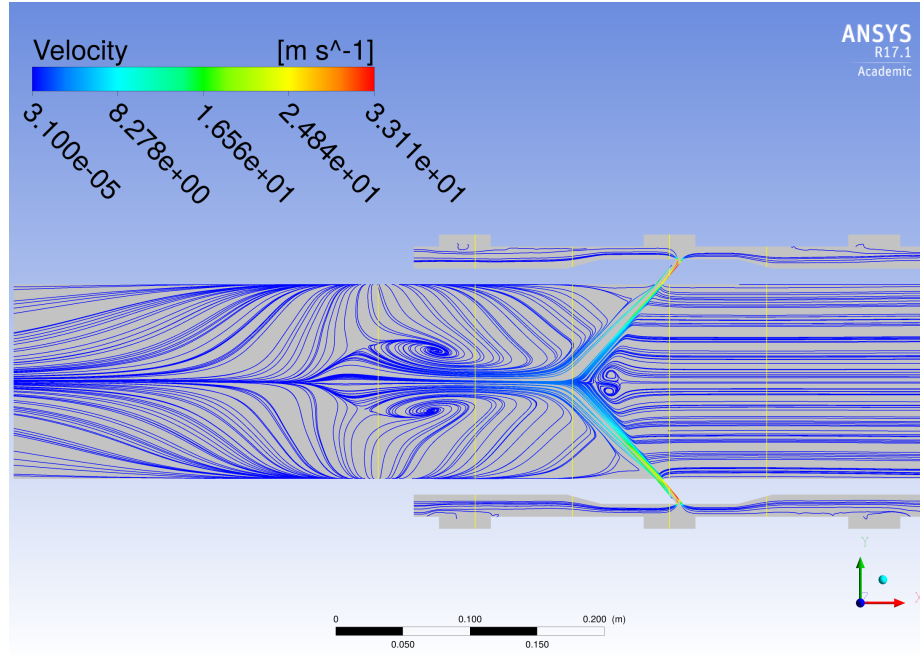
Figure 5.10: Streamlines on the centre plane for the 40° nozzle device.

developed profile.

Although the jets collide, the crossflow around the jets still induces two counter rotating vortices in each jet. The resulting vortices appear downstream of the jets, in the inner liner. A vector plot showing these vortices is given in Figure 5.12.

5.2 Performance criteria

Now that the pressure and flow results of the simulations have been compared, the simulations can be used to calculate the proposed criteria. Using the method described in Chapter 4, the pressure drop for each device is measured along with the maximum velocity. Then, using curve fitting as described in Chapter 3, the three performance criteria are calculated.

5.2.1 Quadratic flow coefficient

To calculate the quadratic flow coefficient, a set of six simulations is performed. The fluid properties for the simulations are those for room temperature water with a density of 997 kg/m^3 and a viscosity of 0.8899 cP. The annular inlet velocity is selected to achieve a Reynolds number in the device ranging from 10,000 to 210,000. This corresponds to a range of average velocities in the device from 2.30 m^3/d to 49.3 m/s. The flow rates are evenly spaced between these values. For the vortex device with its smaller diameter, the velocity ranges from 8.48 m/s to 178.1 m/s. From these six simulations the pressure drop is extracted and the quadratic flow coefficient is calculated. The resulting flow coefficients
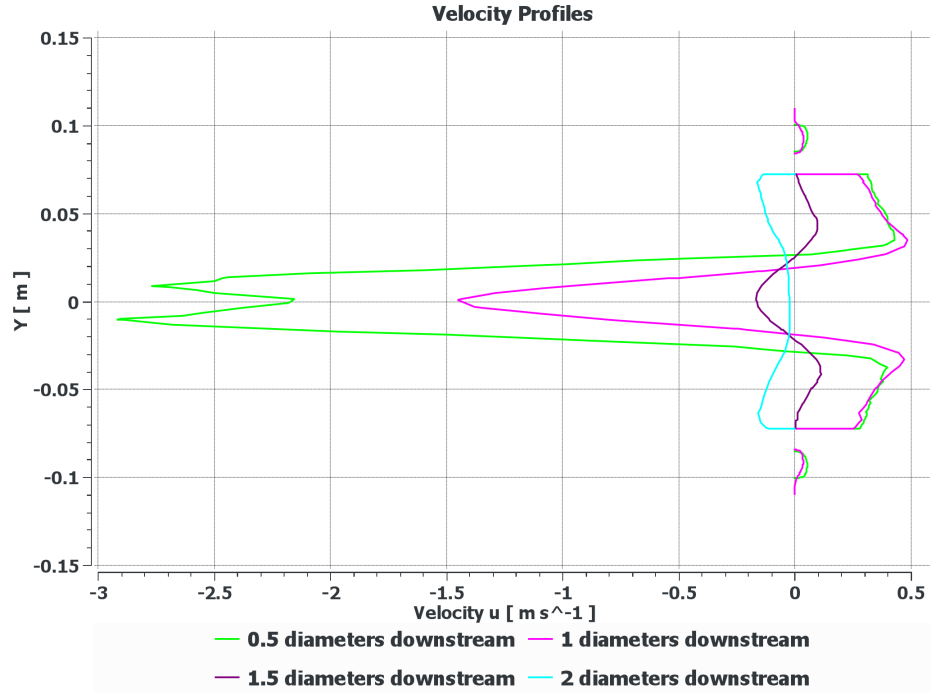
Figure 5.11: Velocity profiles in the inner liner for the 40° nozzle device.

are given in Table 5.1.

Table 5.1: Quadratic flow coefficients.

15° Nozzle	40° Nozzle	Channel	Expanding Nozzle	Diode	Vortex
1.414	1.132	0.8123	1.686	0.4616	0.1929

5.2.2 Erosion potential

Using the same set of six simulations, the maximum velocity is extracted. Using these values the erosion potential for each device is calculated. The resulting values are given in Table 5.2

Table 5.2: Erosion potential.

15° Nozzle	40° Nozzle	Channel	Expanding Nozzle	Diode	Vortex
36.78	55.33	127.3	11.72	104.1	235.8
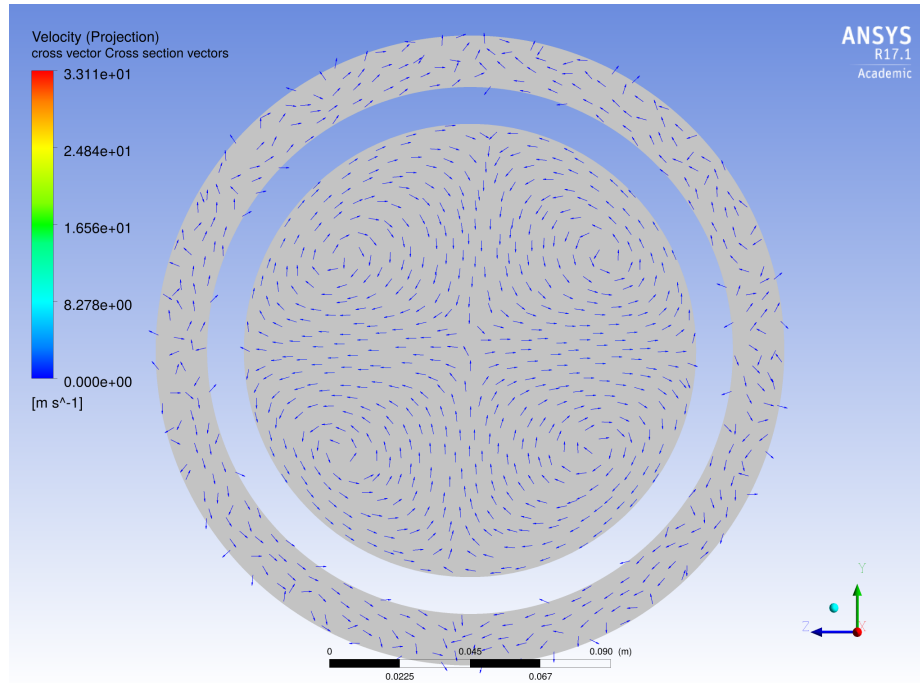
Figure 5.12: Velocity vectors downstream of the jets for the 40° nozzle device.

5.2.3 Viscosity Sensitivity Coefficient

To calculate the viscosity sensitivity coefficient a total of nine simulations is performed for each device. The viscosity sensitivity is calculated for three flow rates 2.30 m^3/d, 25.32 m^3/d, and 48.33 m^3/d. These correspond to the extreme values used previously and a middle value. For each of these flow rates simulations are performed at three evenly spaced viscosities of 0.1 cP, 5.05 cP, and 10 cP. All other fluid properties are held constant. From these simulations the viscosity sensitivity is calculated at the three flow rates. The resulting viscosity sensitivity values are given in Table 5.3.

Table 5.3: Viscosity sensitivity.

Flow rate	15° Nozzle	40° Nozzle	Channel	Expanding Nozzle	Diode	Vortex
2.30 m^3/d	112.3	205.4	963.6	4.248	60.72	-736.0
25.32 m^3/d	303.6	419.6	1,585	17.34	477.8	-3,150
48.33 m^3/d	509.9	456.4	2270	17.80	508.4	8,955

Chapter 6

Analysis

To analyze the proposed criteria they are compared to the ideal characteristics of performance criteria described in Chapter 3. First the criteria are compared to the flow results, to ensure each criteria is accurately tied to a specific aspect of the performance. The criteria are then analyzed to determine the dependence of the criteria on the flow rate and fluid properties. By analyzing the extent of this dependence, the limitations of the new criteria are determined. To show the benefits of the new criteria, they are compared to the current criteria. Finally, to demonstrate the proposed criteria, they are used to compare the six ICD designs.

6.1 Physical Meaning

One of the goals in selecting the performance criteria was to make each criteria relate to a specific aspect of the performance of the device. The quadratic flow coefficient relates to the minor losses, the viscosity sensitivity coefficient to the frictional losses, and the erosion potential to the erosion rate. To examine if the criteria are linked to these aspects of the performance, the criteria are compared to the expected relevance of these quantities in each device.

6.1.1 Quadratic Flow Coefficient

Based on the derivation, the quadratic flow coefficient is directly related to the minor losses. The smaller the quadratic flow coefficient the larger the minor losses in the device. The minor pressure losses are the result of sudden changes in geometry that cause flow separation and eddies in the flow. The physical meaning of the coefficient is examined by comparing the minor losses with the quadratic flow coefficient.

For the two straight nozzles, the only difference is the angle of the nozzle. Both nozzles have two minor losses, the entrance loss and the exit loss. For these, the minor losses are expected to be greater for the 40° nozzle, where the sharp entrance and exit angles induce greater flow separation in the device. Comparing this with the values of the quadratic flow

coefficient shows a corresponding decrease in the criterion from 1.414 to 1.132. In the same way, the sharp entrance and exit angles (80.91°) of the channel device result in increased minor losses and a corresponding decrease in C_{qfc} to 0.8123. For the expanding nozzle, the expansion reduces the entrance and exit losses, resulting in a high C_{qfc} value of 1.686, as expected.

For the two autonomous ICDs, additional methods of producing pressure loss are used. The portion of these losses, independent of the viscosity, is added to the minor losses and affects the quadratic flow coefficient. These additional losses further decrease the value of C_{qfc}. For the diode nozzle, C_{qfc} drops to 0.4616. For the vortex design there are large losses resulting from the large momentum dissipation of the vortex. This results in a significantly lower C_{qfc} of 0.1929.

Overall, the coefficient values closely match the expected minor losses. By examining the quadratic flow coefficient for a device, the level of minor losses in the device can be determined. Thus, the criterion is successfully linked to this aspect of the performance.

6.1.2 Viscosity Sensitivity Coefficient

From the derivation of the criteria, the viscosity sensitivity coefficient is designed to give a measure of the frictional losses in the device. For this derivation it is assumed that the friction factor is inversely proportional to the Reynolds number of the flow. While this holds for laminar flow, it is a rough approximation for turbulent flow.

For the straight passive designs the frictional losses are expected to be related to the length of the flow path through the device. Since the flow is not fully developed in the shorter nozzle, the frictional losses are not directly proportional to the length. For the two straight nozzles, the 40° nozzle has a slightly longer flow path. The viscosity sensitivity is slightly higher in the 40° nozzle, except at the higher flow rate. For the channel, the length of the flow path is significantly greater than the short nozzles. This is clearly reflected in the viscosity sensitivity.

In the expanding nozzle, the flow is only along one side of the device, resulting in a decrease in frictional losses. In the diode nozzle, the longer flow path through the loop causes additional frictional losses. For both these devices the viscosity sensitivity corresponds to the expected behaviour (lower in the expanding nozzle and higher in the diode). The specialized flow in the vortex has been shown to restrict low viscosity flow in some cases [15]. This is reflected in the resulting negative viscosity sensitivity, which is in fact highly desirable in ICDs.

Overall, the viscosity sensitivity matches the expected behaviour of the device. It is also able to capture the frictional losses in more complex autonomous designs. Thus, the viscosity sensitivity is successfully linked to the frictional losses.

6.1.3   Erosion Potential

The erosion potential is designed to predict the level of erosion based on the maximum velocity in the flow. This simplified approach does not include factors, such as the material, particle size, and particle density. More importantly, the curvature of the flow can also be a significant factor in the erosion. To examine the effectiveness of this criterion, it is compared to the expected erosion rate.

For the straight nozzles and the channel, the erosion is expected to occur at the entrance of the device. The sharper the entrance angle the greater the erosion rate. This erosion is composed of two parts. As the flow is forced around the sharp entrance angle, the edge of the entrance erodes. Erosion also occurs, as the flow is concentrated against the far wall. This concentration of the flow results in the peak velocity used in the erosion potential. Thus, as the entrance angle increases the erosion potential increases.

For the expanding nozzle, the expansion prevents this concentration of the flow, resulting in a low value for the erosion potential. This fails to capture the erosion at the entrance of the device, where the sharp curvature and thin material would quickly erode, increasing the size of the entrance. Thus, the criterion performs poorly in this case, where the curvature of the flow is a dominant factor in the erosion.

For the diode nozzle the diameter of the channels is constant, so the erosion potential fits with the expected erosion. For the vortex, the peak velocity occurs near the core of the vortex. These high velocities in the vortex are expected to cause significant erosion of the guide vanes and the walls surrounding the vortex. This high erosion is captured in a correspondingly high erosion potential.

Overall the erosion potential works well for devices with straight non-expanding entrances, as it captures the concentration of the flow in the devices. But, it does not capture the effects of the curvature in the devices and should always be compared to the expected erosion patterns. As sharp corners are rounded by erosion, the geometry and performance of the device will change over time. Thus, while the erosion potential works well for many devices, it is a simplified criterion that should be compared to the expected erosion rate.

6.2   Flow Independence

A significant issue with current criteria is the dependence of the criteria on the flow rate and fluid properties for which they are calculated. To reduce this dependence, the pressure drop is split between two coefficients and least squares regression is used to calculate the criteria from multiple measurement. To analyze the dependence of the resulting criteria, the quality of the fit is examined and the criteria are compared for different flow rates or viscosities.

6.2.1 Quadratic Flow Coefficient

For the quadratic flow coefficient, simulations for a range of flow rates are used in a least squares fit, to calculate the criteria. A sample of the fitted curve for the 15° nozzle is shown in Figure 6.1. The polynomial fit of the form $\Delta P = au^2 + bu$ fits closely to the data, giving an R^2 close to one. To assess the sensitivity of C_{qfc} to the flow rate, the quality of the fit is examined, as expressed by the R^2 value. For all the devices, the R^2 value is greater than 0.99. Thus, the quadratic flow coefficient is independent of the flow rate.
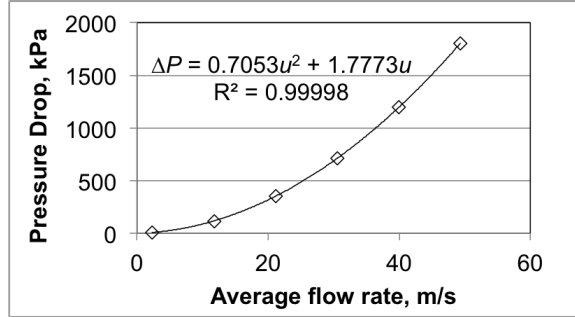

Figure 6.1: Sample plot of the fitted curve for the 15° nozzle.

When calculating C_{qfc}, the viscosity is held constant at 0.8899 cP. To check for viscosity dependence, the criteria can be calculated from the viscosity sensitivity simulations, using three points. Since the R^2 values are high, calculating C_{qfc} from these sets of three points should still provide accurate results. The resulting quadratic flow coefficients are given in Table 6.1.

Table 6.1: Quadratic flow coefficients.

Viscosity	15° Nozzle	40° Nozzle	Channel	Expanding Nozzle	Diode	Vortex
0.8899 cP	1.414	1.132	0.8123	1.686	0.4616	0.1929
0.1 cP	1.528	1.201	0.9736	1.750	0.4819	0.1847
5.05 cP	1.342	1.176	0.7404	1.754	0.4797	0.0987
10 cP	1.303	1.171	0.7138	1.749	0.4772	0.0841
Maximum change	8.1%	6.1%	19.9%	4.0%	4.4%	56.4%

For most devices, the variation is under 10%, and there is no overlap between the devices. For the channel and vortex designs, the variation is higher, especially for the vortex. This seems to correspond to the devices with large viscosity sensitivities. To further inspect the dependence the values for the quadratic flow coefficient are plotted against the viscosity in Figure 6.2. Based on this plot the value of C_{qfc} decreases slightly at higher viscosities.

Although there is a dependence on viscosity, it is not large enough to affect the comparison. To further reduce this dependence, future implementations could use values in the least squares regression that are evenly spread across the range of viscosities.
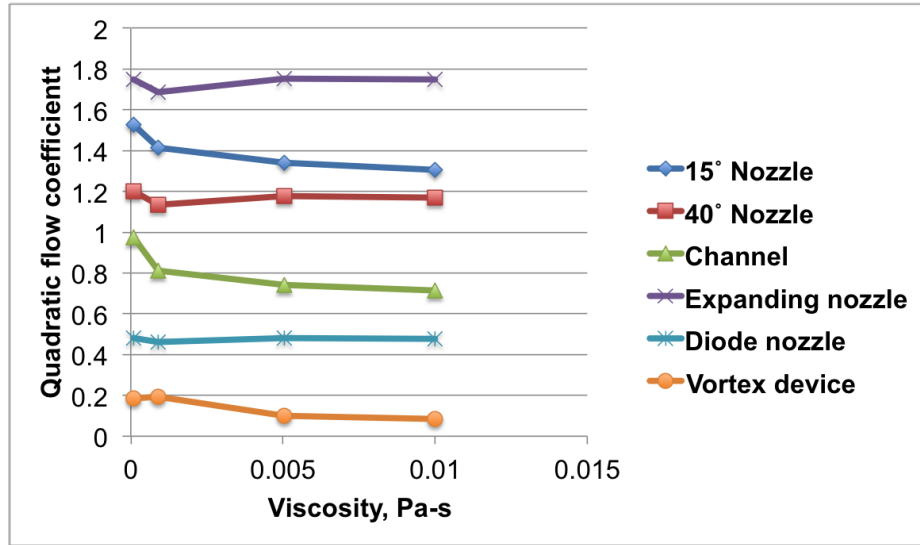

Figure 6.2: Quadratic flow coefficient versus viscosity for the six devices.

6.2.2 Viscosity Sensitivity Coefficient

As with the quadratic flow coefficient, the viscosity sensitivity is calculated across a range of viscosities with a linear least squares fit. For most of the values the fit is good, with an R^2 value greater than 0.88. The only exceptions are the fit for the low viscosity runs in the expanding nozzle and the mid viscosity runs in the vortex device. For the expansion case, the three points are close together and should give a very low viscosity sensitivity. For the vortex, the assumption of linear behaviour is not necessarily valid, because of the specialized behaviour of the device. As shown in Wang et al., the pressure drop initially decreases with viscosity, but for higher viscosities the pressure drop rises again [15]. This nonlinear behaviour could explain the poor fit of the viscosity sensitivity in the vortex. Since the velocities in the vortex device are too large for normal operations, this device should be reassessed with proper dimensions.

For the viscosity sensitivity a certain amount of variation with flow rate is expected. To examine this aspect the viscosity sensitivity is calculated at three flow rates across the expected range. For comparing the devices, the viscosity sensitivity at the mid flow rate of 25.32 m^3/d is used. The range of variation in the criteria is compared to this value in Table 6.2.

Although there is significant variation with flow rate, the values are of the same order of magnitude with the exception of the vortex device. The viscosity sensitivity coefficient

Table 6.2: Viscosity sensitivity.

Flow rate	15° Nozzle	40° Nozzle	Channel	Expanding Nozzle	Diode	Vortex
2.30 m^3/d	112.3	205.4	963.6	4.248	60.72	-736.0
25.32 m^3/d	303.6	419.6	1,585	17.34	477.8	-3,150
48.33 m^3/d	509.9	456.4	2,270	17.80	508.4	8,955
Relative Range	131%	60%	82%	78%	94%	308%

is plotted against the flow rate in Figure 6.3. For all the devices, the overall trend is for the viscosity sensitivity to increase with increasing flow rate.
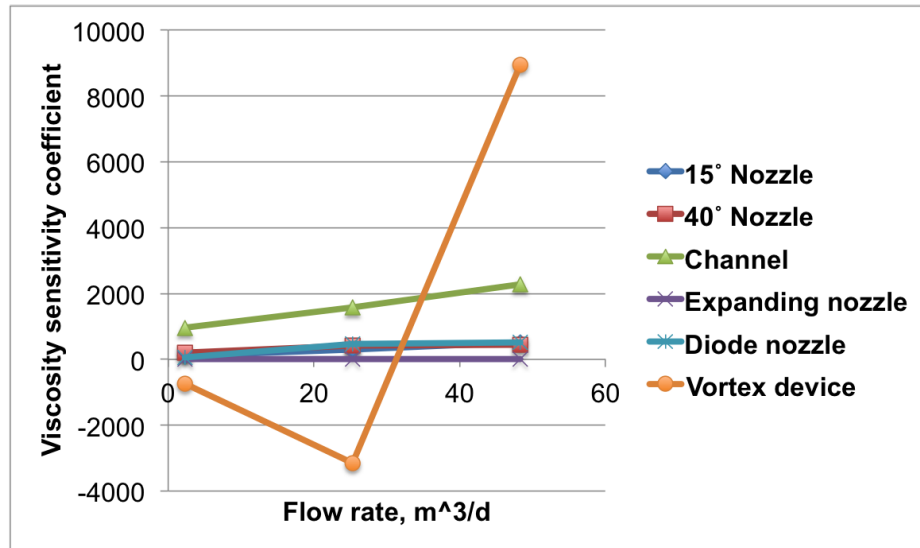

Figure 6.3: Viscosity sensitivity coefficient versus flow rate for the six devices.

For these devices the viscosity sensitivity at 25.32 m^3/d can be used as representative of the devices viscosity sensitivity. For the vortex at low flow rates the values indicate a negative viscosity sensitivity that preferentially restricts low viscosity fluids. At high flow rates this transitions to a high positive viscosity sensitivity that favours the production of low viscosity fluids. As mentioned in Section 5.1.7, this device should be reassessed with dimensions that more closely resemble its practical use, where the flow regime is expected to result in a more consistent viscosity sensitivity coefficient for this device.

While the viscosity sensitivity coefficient at a single flow rate can be used, it should be used with caution. It is important to check the dependence of the viscosity sensitivity on the flow rate and viscosity.

6.2.3 Erosion Potential

For the erosion potential, the flow rate dependence is reduced by applying a linear fit of the maximum velocity to the six simulations for the quadratic flow coefficient. These all fit well with an R^2 value greater than 0.99. As in the case of the quadratic flow coefficient, the erosion potential is calculated for each viscosity. The results are given in Table 6.3.

Table 6.3: Erosion potential.

Viscosity	15° Nozzle	40° Nozzle	Channel	Expanding Nozzle	Diode	Vortex
0.8899 cP	36.78	55.33	127.3	11.72	104.1	235.8
0.1 cP	36.51	54.02	143.0	12.03	124.9	242.0
5.05 cP	37.98	57.60	115.1	13.36	97.1	241.5
10 cP	38.64	58.91	109.3	23.42	93.6	250.8
Maximum change	5.1%	6.5%	14.1%	100%	20%	6.4%

For most of the devices the variation is minor, but for the expanding nozzle the erosion potential varies by 100%. An examination of the simulations reveals that this is the result of a change in behaviour at the high viscosity case. A plot of the erosion potential versus the viscosity is given in Figure 6.4. There does not appear to be any particular trend of the erosion potential to increase or decrease with viscosity. While for most devices this criterion is sufficiently independent, any change in the fundamental flow behaviour can make the linear fit inaccurate.
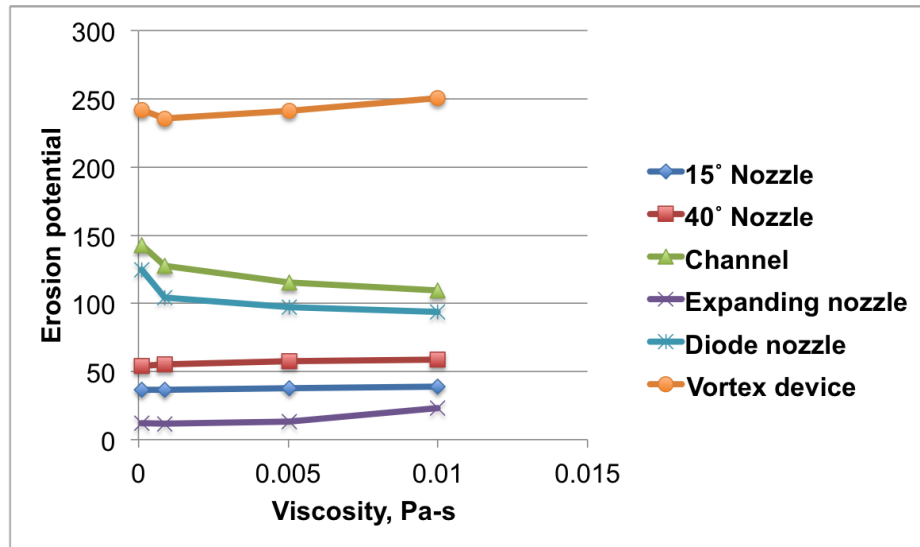

Figure 6.4: Erosion potential versus viscosity for the six devices.

6.3 Criteria Limitations

To effectively use the three criteria it is important to identify their limitations. As shown in the previous section, the criteria are still somewhat dependent on the flow rate and fluid properties for which they are calculated. In particular, the viscosity sensitivity coefficient is dependent on the flow rate. The variation in the criteria tends to be higher for autonomous designs, where the flow behaviour fundamentally changes with the flow rate or fluid properties.

The application of these criteria is also limited by the assumptions with regard to the fluid and geometry. These assumptions affected the way the coefficients were derived and the boundary conditions in the simulations. Although the criteria can be calculated outside these restrictions, further research is needed to test them under these conditions.

6.3.1 Flow Limitations

In deriving the criteria, several assumptions are made about fluid and flow regime in the device. These assumptions affect how well the criteria relate to the physics of the flow. The key assumption in the derivation is that the friction factor is inversely related to the Reynolds number, so that $f = C/\text{Re}$. While this is true for laminar flow, it is a poor approximation for turbulent flow with a high Reynolds number. However, the criteria are calculated from three points across the range of expected viscosities, from 0.1 cP to 10 cP. Since the R^2 value is close too one, the viscosity sensitivity coefficient is representative within this range. But, the model should not be extrapolated beyond this range.

For the criteria and the simulations the following assumption are made for the fluid:

- Incompressible flow

- Single phase fluid

- Newtonian fluid

These assumptions restrict the application of the criteria and the flow simulations. During regular production, the flow is incompressible when liquid oil and water is produced. The single phase fluids are used in the study, to focus on the effect of the individual fluid properties. For oil at the high temperatures in the well, the newtonian assumption is valid, although at low temperatures the bitumen is non-Newtonian [42].

Although this works for regular production, the production well also experiences flow outside the scope of these assumptions. With the production of water comes the possibility of flashing in the device. When water enters the production well, it is only a few degrees below the saturation temperature. As the flow enters the device, the drop in pressure can lead to the water becoming saturated, causing it to flash into steam. This produces multiphase compressible flow in the ICD [54]. Because of the assumptions, this sudden

change in flow behaviour is not captured by the proposed criteria or the simulations and is outside the scope of this study.

6.3.2 Geometry restrictions

For the comparison, only tubing deployed devices are considered. But, the criteria are not dependent on the type of design and can be applied to liner deployed devices as well. To make the comparison as similar as possible, the devices in this study are made to fit into the same space and are designed with the same diameter of 3.8 mm in most of the devices. The only exception is the vortex design, where the diameter is shrunk to 2 mm. Maintaining a constant diameter, allows a better comparison of the impact of the design features on the pressure drop. For this study, the sensitivity to the diameter is not tested. Although the criteria are designed to be independent of the scale of the device, the criteria may still vary with the diameter. However, only a slight change in the diameter is usually needed to size the device for the desired pressure drop.

Most of the devices considered in the study produce a pressure drop in the same order of magnitude. The exception is the vortex design, where the pressure drop is two orders of magnitude greater than the other devices. For the vortex device to have a similar pressure drop would require a large change in diameter, and this could change the behaviour of the device. When using the criteria in practice to compare actual devices, it is best to have the devices sized for a similar pressure drop.

Another area where the diameter must be considered, is the erosion. For the erosion potential, the maximum velocity is compared relative to the average velocity. But, when the diameter is increased, the average velocity decreases, along with the maximum velocity. For the expanding nozzle, with its small pressure losses, the diameter would be small to achieve the desired pressure drop. This, in turn, would result in an increased flow rate and erosion. In general, when the total losses are small, the erosion potential underestimates the erosion.

6.3.3 Additional Considerations

The criteria are designed to be used for both passive and autonomous devices. But, for some autonomous designs, where the flow behaviour varies drastically, these criteria may not be applicable. For these devices it is important to examine the quality of the fit and the variation in the criteria in relation to the flow field revealed by the simulations.

6.4 Comparison with Current Criteria

While the proposed criteria have limitations, they are a significant improvement over the current criteria. They are more directly related to the behaviour of the device and allow for a more informed comparison of the devices.

6.4.1 Quadratic Flow Coefficient Vs. Discharge Coefficient

One of the most common criteria is the discharge coefficient, C_d, defined by

$$\Delta P = \frac{\rho u^2}{2C_d^2} \tag{6.1}$$

This is designed for an orifice and assumes that the frictional losses are negligible. Applying the assumption of negligible frictional losses to the equation for the new criteria, gives

$$\Delta P = \frac{\rho u^2}{C_{\text{qfc}}} + \frac{C_{\text{vis}}\, \delta u \mu}{D^2} \rightarrow \Delta P = \frac{\rho u^2}{C_{\text{qfc}}} \tag{6.2}$$

Comparing this to the discharge coefficient, shows that for an orifice the discharge coefficient can be given in terms of the quadratic flow coefficient as $C_{\text{D}} = \sqrt{C_{\text{qfc}}/2}$. But, for many devices, the frictional losses cannot be neglected, causing the discharge coefficient to vary with the Reynolds number. In deriving the new criteria, this variation is separated from the minor losses and characterized by the viscosity sensitivity coefficient. This reveals the quadratic flow coefficient as an improved discharge coefficient for inflow control devices.

6.4.2 Frictional Losses

Although there are no criteria commonly used for the frictional losses, the sensitivity of the pressure drop to viscosity is sometimes examined using plots of the pressure drop versus viscosity [14]. To obtain a quantitative measure, the slope of this line is used. The proposed viscosity sensitivity coefficient is an improvement over this, since it extracts the flow rate and scale of the devices from the coefficient. This allows the criteria to be applied to a wider range of cases.

In designing the criteria, the flow rate is extracted to reduce the dependence on flow rate. While the viscosity sensitivity criteria still varies somewhat with the flow rate, this variation is usually of the same order of magnitude. Current methods, where the flow rate is included in the sensitivity, result in a higher dependence on the flow rate. Thus, while not completely independent of flow rate, the viscosity sensitivity criterion is an improvement over current methods.

6.4.3 Erosion Measurement

Due to the simplified model, the erosion potential is not as accurate as erosion experiments or simulations. But, when testing multiple designs, these methods are complex and time consuming. Compared to these, it is easy to extract the maximum velocity from a simulation. But, using the maximum velocity neglects other factors that can influence erosion.

The normalized form of the maximum velocity, used in the erosion potential, is preferable to the maximum velocity on its own. While the erosion potential is an improvement over the maximum velocity and is easy to calculate, it only provides a rough estimate of the erosion rate.

6.5 Combined Criteria

Since multiple criteria have been defined, it is challenging to identify the best design. For a comparison, devices are usually sized for the same pressure drop as defined by the FRR value. This allows for a comparison by plotting the pressure drop versus volumetric flow rate for the devices. For the devices in this study, the diameter of the devices is kept constant except for the vortex device, in order to focus the analysis on the flow patterns. This results in each device having a different pressure drop.

6.5.1 Device Scaling

To size the devices, the criteria can be used in equation 2.19 to scale the devices for the same pressure drop. But, in scaling the device several assumptions are made.

- A device is scaled by changing only the diameter

- The quadratic flow coefficient is independent of diameter

- The viscosity sensitivity coefficient is independent of the diameter

- A single fixed value can be used for each criteria

For the device sizing, only the diameter is changed. Although other means can be used to size a device, this method limits the changes in the device. While the criteria are designed to be independent of the scale of the device, a large change in the diameter could affect the criteria by altering the flow regime. For this comparison, however, the criteria are assumed to be independent of the diameter, as long as the change to the diameter is small.

For the comparison, a single value is used for each criterion. For the quadratic flow coefficient, the value for water is used. For the viscosity sensitivity coefficient, the value is selected for a mid flow rate of 25.32 m^3/d. While the criteria are known at other flow rates and viscosities, the criteria are designed to be expressed by a single value at a defined flow rate and viscosity.

6.5.2 Diameter Calculation

To size the devices, the values of the criteria are inserted back into equation 3.7 to calculate the diameter. Since the diameter changes the flow rate in the device, the equation is expressed in terms of the volumetric flow rate. The average flow rate in the devices is given by $u = 4Q/n\pi D^2$, where Q is the volumetric flow rate through the devices and n is the number of devices at the location. Replacing the average flow rate gives

$$\Delta P = \frac{16\rho Q^2}{n^2\pi^2 D^4 C_{\text{qfc}}} + \frac{4C_{\text{vis}}\delta Q\mu}{n\pi D^4} \tag{6.3}$$

To resize the devices this equation is solved for the diameter, giving

$$D = \left(\frac{16\rho Q^2}{n^2\pi^2 C_{\mathrm{qfc}}\Delta P} + \frac{4C_{\mathrm{vis}}\delta Q\mu}{n\pi\Delta P} \right)^{1/4} \qquad (6.4)$$

To size the device, the desired flow rate, pressure drop, and fluid properties are inserted into equation 6.4, giving the device diameter. When sizing a device, the FRR value is typically used, with its prescribed flow rate and fluid properties. To compare the six devices, they are sized for an FRR value of 0.8 with four ICDs ($n=4$). Inserting these values into equation 6.4 gives the device diameters as

Table 6.4: Device diameters for an FRR of 0.8 and $n=4$.

15° Nozzle	40° Nozzle	Channel	Expanding Nozzle	Diode	Vortex
3.27 mm	3.46 mm	3.87 mm	3.07 mm	4.28 mm	5.14 mm

For most devices the diameter change is small, with the greatest change occurring in the vortex design, which was simulated for a diameter of 2 mm. Now that the diameters are sized, equation 6.3 can be used to predict the pressure drop across the device.

6.5.3 Performance Comparison

For the comparison, three fluid are considered, bitumen at 200°C [9], water at 25°C, and water at 200°C. For all three, the pressure in the production well is assumed to be around 2 MPa. The fluid properties are given in Table 6.5. Using equation 6.3, the pressure drop curves are calculated using the Matlab®script in Appendix A.

Table 6.5: Density and viscosity values for bitumen and water at 2 MPa.

Fluid Property	Bitumen at 200°C	water at 25°C	water at 200°C
Density, kg/m^3	888.14	997.9	865 7
Viscosity, cP	9.957	0.8896	0.1344

For flow through the ICDs, the flow is driven by the pressure drop across the device. As different fluids are produced, the flow rate changes, while the pressure drop remains constant. To compare these devices, the flow rate of the three fluid is compared at a fixed pressure drop of 600 kPa. The pressure drop versus volumetric flow rate plot for each devices is given in Figure 6.5.

For the two straight nozzles the behaviour is similar, with increasing production as the viscosity decreases. For the channel, the lines are more widely spread as a result of the high viscosity sensitivity of the device. In the expanding nozzle and diode nozzle, the curves for the bitumen and 25°C water cross each other, because of the higher density of the water.
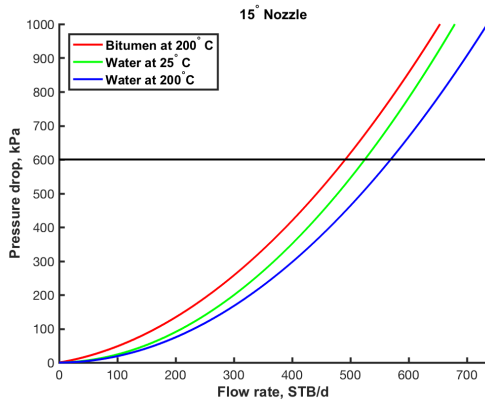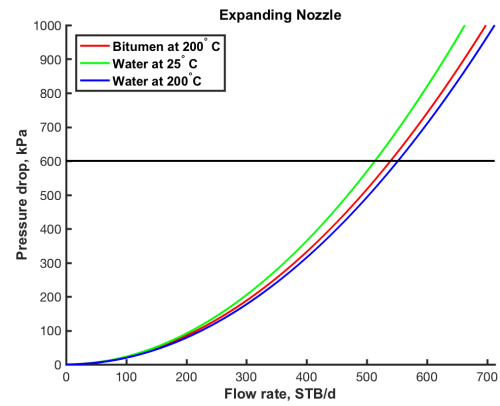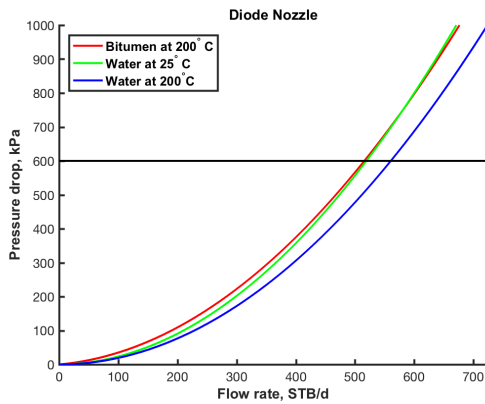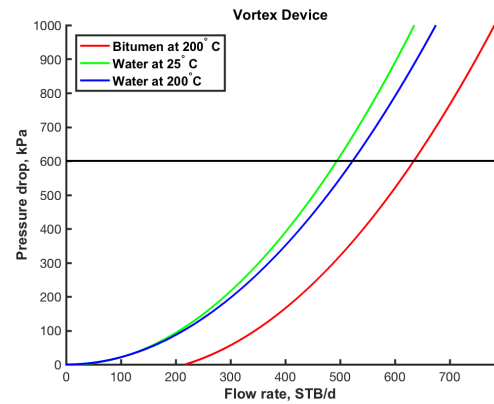
(a) 15° Nozzle.
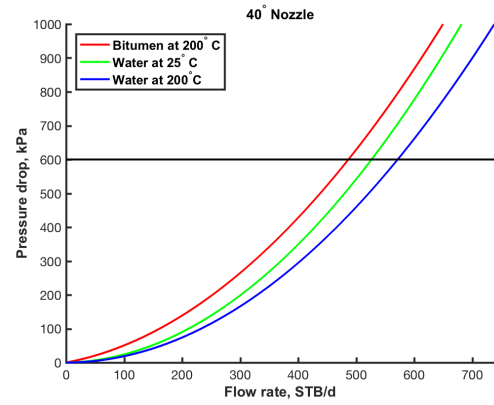
(b) 40° Nozzle.
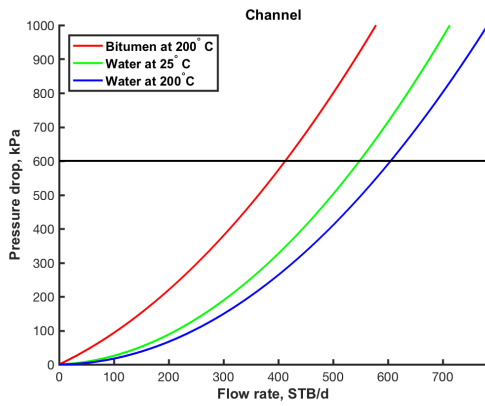
(c) Channel.

(d) Expanding nozzle.

(e) Diode nozzle.

(f) Vortex device.

Figure 6.5: Pressure drop versus volumetric flow rate plots for the six devices with bitumen and water at 2 MPa.

For both these devices the lines are close together indicating little change in production rate, when water is produced.

The vortex device, because of the negative viscosity sensitivity, shows preferential production of the viscous oil. This would indicate that the device decreases the production rate when water is produced. However, for this comparison only a single value of the viscosity sensitivity is used. For higher flow rates, this sensitivity reverses, with a large positive viscosity sensitivity. The use of a single value for the vortex creates unrealistic flow behaviour for the viscous bitumen at low flow rates, where the curve should pass through the origin. Due to the use of the single negative value for the viscosity sensitivity, the model incorrectly predicts a positive flow rate at a pressure drop of zero.

To compare the devices under operational conditions, the pressure drop curves for the six devices are plotted together in Figure 6.6. For the bitumen, a high flow rate is desirable, while for water, a low flow rate is preferable. For the bitumen, the vortex device has the highest production rate, followed by the expanding nozzle and the diode nozzle. The worst performance is shown by the channel device with the lowest production rate for oil. For the water the order of the curves is reversed, with the channel producing the most water.
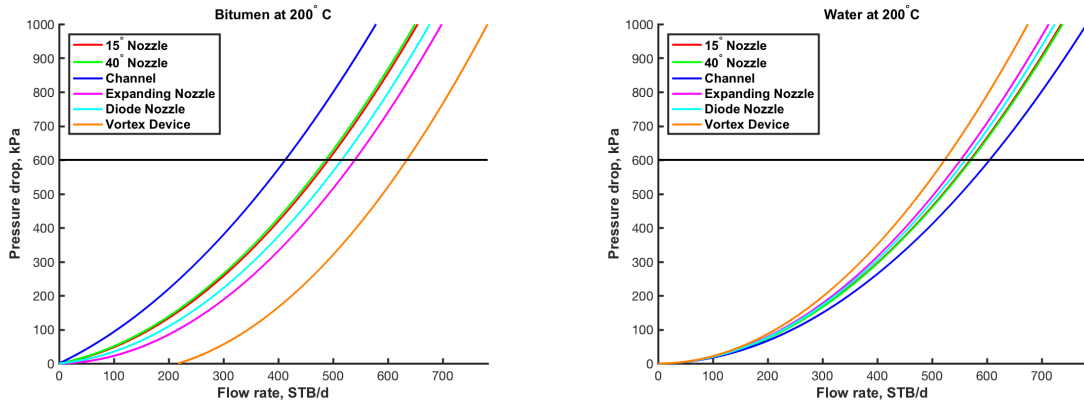
(a) Device comparison for bitumen at 200°C.   (b) Device comparison for water at 200°C.

Figure 6.6: Device comparison for bitumen and water at 200°C and 2 MPa.

6.5.4   Comparison Limitations

Comparing these plots gives an understanding of the performance of the devices and the effect of the criteria. But, this comparison makes many assumptions and can only give a rough estimate of the flow performance. This is apparent for the vortex design, where the variation in the viscosity sensitivity would greatly change the flow behaviour at high and low flow rates. The use of a single value of the viscosity sensitivity coefficient for the vortex also results in unrealistic behaviour, where the pressure versus flow rate curve fails to pass through the origin.

6.6 Design Comparison

Based on the criteria and the comparison plots, the best of the six designs can be determined. First the four passive ICDs are considered, then the two autonomous designs.

The two straight nozzles demonstrate that a sharper entrance angle improves the performance of the device by increasing the quadratic flow coefficient. But, it also increases the rate of erosion. The use of a long channel to produce the pressure drop is a poor choice, since this results in a high sensitivity to viscosity. This restricts the production of the oil, while increasing production of water. The use of an expansion, produces a very low viscosity sensitivity, and based on the criteria, this is the best passive ICD design. But, the erosion is not well captured by the erosion potential and could cause the device to erode rapidly.

The Tesla diode design, has a low quadratic flow coefficient, while avoiding a large viscosity sensitivity. The comparison plots show that it performs better than the straight nozzles and is close to the expansion nozzle. Unlike the expansion, the diode avoids the thin geometry that could quickly erode. While its erosion potential is greater than for the straight nozzles it is still less than that of the channel design. Of these devices, the diode nozzle is the best design.

While the results for the vortex device are promising, further simulations would need to be done with a larger diameter and more realistic velocities. Based on the simulation in this study, the design could produce a negative viscosity sensitivity, that would selectively restrict low viscosity fluids, which is ideal. However, this behaviour is sensitive to changes in flow rate and viscosity, and could quickly reverse, causing poor performance.

6.7 Conclusion

An analysis of the proposed criteria reveals that the criteria provide an improved method of comparing ICD designs. The criteria are closely linked to the physics and can be used to understand the flow behaviour of a device. Although there is still some dependence of the criteria on the flow rate and viscosity, this is reduced by the method of calculating the criteria with a fitted curve. This variation can be large for devices with strong autonomous behaviour, where the flow behaviour changes with flow rate or viscosity. For these devices, the criteria can vary too much to be represented by a single value. While the erosion potential is an improvement over the maximum velocity, it is not able to capture the effect of curvature in the design. This causes it to give an inaccurate measure of erosion in the expanding nozzle. In spite of these limitations, the proposed criteria are an improvement over the current criteria for comparison between devices.

The criteria can be used to inform further design improvements of new devices. Since the criteria are designed to be used in an optimization, they can easily be used when optimizing a design. As proposed by Li et al., the proposed criteria can be minimized by using CFD simulations to optimize the ICD design [46]. These criteria can also be used to improve

designs by combining devices to achieve a desired flow behaviour.

Based on the comparison of the six designs, the diode nozzle shows the best results. Due to the high erosion expected in the expanding nozzle, the diode nozzle is preferable. The long channel design clearly shows the worst results, because of its high viscosity sensitivity coefficient. While the vortex design shows promising results, further study of the device is needed to effectively compare it to the other designs.

Chapter 7

Summary and Conclusions

For SAGD wells, inflow control devices improve performance by evening out production and restricting the production of unwanted fluids. For these ICDs, a wide variety of designs are used that use different methods to control the flow. To compare these devices, only a few criteria are available that are highly dependent on flow rate and fluid properties. In this study, a new set of criteria is proposed to facilitate the comparison and analysis of ICD designs for these applications.

Three criteria are proposed that are based on the physics of the flow and designed to be representative of different aspects of the flow performance. The criteria are also designed to be less dependent on the flow rate and fluid properties, than current criteria. To achieve this, the criteria are calculated from multiple measurements using a least squares fit. So the criteria are easy to optimize, they are made dimensionless and are designed to be minimized for the best performance.

The three criteria are the quadratic flow coefficient, the viscosity sensitivity, and the erosion potential. The quadratic flow coefficient is a measure of the device's ability to resist changes in the flow rate, especially large increases in flow rate, resulting from the production of water or steam. This is also tied to the minor losses in the device. The viscosity sensitivity is designed to measure the decrease in flow resistance with low viscosity fluids. This criterion is tied to the frictional losses in the device. Finally, the erosion potential provides a rough measure of the erosion rate based on the maximum velocity.

To test the criteria, six ICD designs are modelled using computational fluid dynamics. The designs are chosen to cover a range of different designs. Four passive ICDs are considered, consisting of two straight nozzles at $15°$ and $40°$, a long winding channel, and an expanding nozzle. Two autonomous ICD designs are also considered. One design is based on Tesla's fluidic diode, placed in the reverse direction to create a high pressure drop. The other is a vortex based design that uses a vortex in the device to produce a pressure drop.

For these six designs, the flow is carefully modelled, including the regions up and downstream of the device. To ensure an accurate model, the sensitivity of the model is examined with respect to the domain size, grid refinement, and turbulence model. For validation of

the model, the frictional losses in a helical channel are compared to an empirical model. The main model is validated, by using the same mesh and simulation settings, when modelling the helical channel.

Once the CFD model is tested, the results of the simulations are examined and compared to the expected physics of the flow. Based on the pressure contours, the sources of minor and frictional losses are identified. The devices show high minor losses at the entrances with greater losses for those with steeper entrance angles. As expected, the long channel produces a large frictional loss. For the diode nozzle the primary pressure loss is the result of the intersection of the channels. In the vortex design, the primary pressure loss is caused by the increased velocity in the vortex. Using these simulations the proposed criteria are calculated for each design.

Based on the analysis of these criteria, the proposed criteria provide an improved method for evaluating and comparing ICDs. Since multiple criteria are used, they can be linked to specific aspects of the devices performance. The quadratic flow coefficient is tied to the minor losses with the effects of viscosity removed and assigned to the viscosity sensitivity. The erosion potential measures the erosion separately from the flow rate. The analysis of these criteria demonstrates that each criterion is linked to a specific aspect of the performance.

Part of the goal in developing the new criteria was to reduce the dependence of the criteria on the flow rate and fluid properties. This was targeted especially through the use curve fitting. An analysis of the criteria reveals that, while there is still some dependence, the new criteria are less dependent on the flow conditions than current criteria. Although the viscosity sensitivity is made independent of the fluid viscosity, it continues to be dependent on the flow rate. While not used in an optimization, the criteria are designed to be minimized for the best performance.

In addition to comparing particular performance aspects, the proposed criteria can be combined for an overall comparison of ICD designs. The combined comparison is based on results across a range of flow rates and viscosities. This is an improvement over current single criteria methods, which are based on a limited set of flow conditions.

To demonstrate the use of these criteria, the six ICD designs are compared. Of the passive designs, the expanding nozzle demonstrates the best criteria values, because of a low viscosity sensitivity. But, the erosion at the entrance of the expansion is not captured by the erosion potential. Of the remaining devices, the diode provides a well balanced result that provides a low quadratic flow coefficient without too great an increase in the viscosity sensitivity and erosion potential.

The performance of the vortex design is difficult to interpret from these simulations, because of the unrealistically high flow rate and pressure drop. While it is able to produce a negative viscosity sensitivity, this is dependent on the flow rate. For a high flow rate, the simulations give a large positive viscosity sensitivity that results in poor performance. In addition the vortex produces high velocities that could cause significant erosion.

Comparing the six designs the diode nozzle provides the best performance, while maintaining a reasonable erosion rate. Although the expanding nozzle shows good results, the expected erosion would quickly erode the device. The vortex design shows promising results but requires further investigation. The worst device is clearly the long channel device. The high frictional losses cause the device to have a high viscosity sensitivity. This encourages production of low viscosity water, while restricting oil production.

7.1 Contributions of this Thesis

The new criteria proposed in this thesis provide an improved method for comparing and evaluating ICD designs. The reduced dependence of the criteria allows devices to be compared, without the need for identical sizing, fluids, and flow rates. The connection between the criteria and the flow behaviour allows the criteria to provide an understanding of a device's strengths and weaknesses. Although still somewhat dependent on the flow rate and fluid properties, the proposed criteria are a definite improvement over current criteria.

Another contribution of this thesis is the method of calculating the criteria in connection with CFD modelling. With CFD models, it is easy to simulate the flow for a wide range of flow conditions. By using curve fitting, the results of these simulations can be expressed by a few criteria that are representative of the flow performance and independent of the flow conditions.

7.2 Future Work

In testing the proposed criteria the passive ICD designs were selected to examine the effect of the entrance angle, expansion angle, and channel length. Another consideration for future testing is the effect of rounded edges on the device performance. As the edges of a device erode over time, the performance of the device changes due to the rounded edges. Particularly at the entrance of the device this could cause a significant reduction in the pressure drop.

While the proposed criteria consider the flow behaviour and erosion, there are other considerations in the development of an ICD design. One of these is the risk of plugging in the device, where fines and sand particles become trapped in the device increasing the flow resistance and potentially blocking the flow. Future work should develop criteria to evaluate the risk of plugging, so that a more informed comparison can be made between ICD designs.

For this study the fluids used are restricted to single phase Newtonian fluids, where the flow in incompressible. But, for flow in a SAGD well, the fluid entering the well is a multiphase emulsion of oil and water. This combination, along with separate oil and water, produces a complex multiphase flow. While bitumen is Newtonian at high temperatures, under other conditions the fluid can be non-Newtonian. To accurately simulate the flow,

future simulations should incorporate the multiphase non-Newtonian character of the fluid.

Another consideration is flashing of the water in the device. Since the water enters near its saturation temperature, it can easily flash into steam, when pressure drops. This results in multiphase compressible flow, which is not considered in this study. Future work should simulate the effect of flashing in the device using multiphase compressible flow models. Since flashing results in a sudden change in the pressure drop, the proposed criteria are not sufficient to describe this behaviour. Future work should consider additional criteria to capture these features.

Bibliography

[1] Natural Resources Canada, "Energy markets fact book: 2014-2015," 2014. [Online]. Available: http://publications.gc.ca/site/eng/449509/publication.html

[2] Alberta Government, "Oil sands: Facts and stats," June 2017. [Online]. Available: https://open.alberta.ca/publications/oil-sands-facts-and-stats

[3] Institute for Oil Sand Innovation, "Oil sands." [Online]. Available: https://www.ualberta.ca/engineering/research/groups/oil-sands-innovation/oil-sands

[4] Alberta Energy Regulator, "Crude bitumen production," 6 2018. [Online]. Available: https://www.aer.ca/providing-information/data-and-reports/statistical-reports/crude-bitumen-production.htm

[5] A. de Klerk, M. R. Gray, and N. Zerpa, *Chapter 5 - Unconventional Oil and Gas: Oilsands A2 - Letcher, Trevor M.*, 2nd ed. Boston, USA: Elsevier, 2014, pp. 95–116.

[6] R. M. Butler, "Steam-assisted gravity drainage: Concept, development, performance and future," *Journal of Canadian Petroleum Technology*, vol. 33, February 1994.

[7] R. M. Butler, G. S. Mcnab, and H. Y. Lo, "Theoretical studies on the gravity drainage of heavy oil during in situ steam heating," *The Canadian Journal of Chemical Engineering*, vol. 59, no. 4, pp. 455–460, 1981.

[8] S. Banerjee, T. Abdelfattah, and H. Nguyen, "Benefits of passive inflow control devices in a SAGD completion," in *SPE Heavy Oil Conference Canada 2013*, vol. 2, Baker Hughes, United States. Calgary, AB, Canada: Society of Petroleum Engineers, June 2013, pp. 1195–1203.

[9] N. Edmunds, "Investigation of SAGD steam trap control in two and three dimensions," *Journal of Canadian Petroleum Technology*, vol. 39, no. 1, pp. 30–40, 2000.

[10] J. Kumasaka, K. Sasaki, Y. Sugai, and M. Nakano, "Numerical modeling of emulsion to investigate the SAGD oil production based on viscosity measurements," in *21st Formation Evaluation Symposium of Japan*. Chiba, Japan: Society of Petrophysicists and Well-Log Analysts, 2015.

[11] O. Oyeka, F. Felten, B. Least, and Halliburton, "Screen-inflow-design considerations with inflow control devices in heavy oil," in *SPE Heavy Oil Conference Canada 2014*, Halliburton, Canada. Calgary, AB, Canada: Society of Petroleum Engineers, June 2014.

[12] M. Fripp, L. Zhao, and B. Least, "The theory of a fluidic diode autonomous inflow control device," in *SPE Intelligent Energy International 2013: Realising the Full Asset Value*, Halliburton, United States. Manama, Bahrain: Society of Petroleum Engineers, October 2013, pp. 262–270.

[13] C. Jones, Q. Morgan, S. Beare, A. Awid, and K. Parry, "Design, testing, qualification and application of orifice type inflow control devices," in *International Petroleum Technology Conference 2009*, vol. 2, Weatherford International, Norway. Doha, Qatar: Society of Petroleum Engineers, December 2009, pp. 723–734.

[14] Q. Zeng, Z. Wang, G. Yang, and J. Wei, "Selection and optimization study on passive inflow control devices by numerical simulation," in *SPE Intelligent Energy International 2013: Realising the Full Asset Value*, China University of Petroleum-Beijing, China and Northeast Petroleum University, China. Dubai, United arab emirates: Society of Petroleum Engineers, October 2013, pp. 515–524.

[15] X. Wang, Z. Wang, and Q. Zeng, "A novel autonomous inflow control device: Design, structure optimization, and fluid sensitivity analysis," in *International Petroleum Technology Conference 2014 - Innovation and Collaboration: Keys to Affordable Energy*, vol. 1, China University of Petroleum-Beijing, China. Kuala Lumpur, Malaysia: Society of Petroleum Engineers, December 2014, pp. 512–523.

[16] J. H. Ferziger and M. Perić, *Computational Methods for Fluid Dynamics*, 3rd ed. Berlin, Germany: Springer, 2002.

[17] M. Lastiwka, C. Bailey, B. James, and D. Zhu, "A practical approach to the use and design of flow control devices in SAGD," in *SPE Canada Heavy Oil Technical Conference*. Calgary, Alberta, Canada: Society of Petroleum Engineers, February 2017.

[18] S.-Y. Park, D. Saks, V. Laksmanan, A. Singh, and M. Ma, "Flow control devices for SAGD applications: Lessons learned, best practices, and suggested design improvements," in *SPE Thermal Well Integrity and Design Symposium*. Banff, Alberta, Canada: Society of Petroleum Engineers, November 2017.

[19] N. Tesla, "Valvular conduit," U.S. Patent 1 329 559, February 1920.

[20] S. M. Thompson, T. Jamal, B. J. Paudel, and D. K. Walters, "Transitional and turbulent flow modeling in a tesla valve," in *ASME 2013 International Mechanical Engineering Congress and Exposition*, Department of Mechanical Engineering, Center for Advanced Vehicular Systems, Mississippi State University, United States. San Diego, CA, United states: American Society of Mechanical Engineers, November 2013.

[21] S. M. Thompson, B. J. Paudel, T. Jamal, and D. K. Walters, "Numerical investigation of multistaged tesla valves," *Journal of Fluids Engineering*, vol. 136, no. 8, pp. 081 102–081 102–9, 05 2014. [Online]. Available: http://dx.doi.org/10.1115/1.4026620

[22] T. Q Truong and N.-T. Nguyen, "Simulation and optimization of tesla valves," in *2003 Nanotechnology Conference and Trade Show*, vol. 1, February 2003, pp. 178–181.

[23] R. L. Bardell, "The diodicity mechanism of tesla-type no-moving-parts valves," Mechanical Engineering, University of Washington, 2000.

[24] Y. A. Çengel and J. M. Cimbala, *Fluid mechanics: fundamentals and applications*, 2nd ed. 1221 Avenue of the Americas, New York, NY 10020: McGraw-Hill, 2010.

[25] M. Mahmoudi, V. Fattahpour, A. Nouri, T. Yao, B. A. Baudet, M. Leitch, and B. Fermaniuk, "New criteria for slotted liner design for heavy oil thermal production," in *SPE Thermal Well Integrity and Design Symposium*. Banff, Alberta, Canada: Society of Petroleum Engineers, 2016.

[26] F. Rasimarzabadi, M. Leitch, S. Ansari, and D. S. Nobes, "Flow visualization for performance measurement across sand control orifices," in *SPE Latin America and Caribbean Heavy and Extra Heavy Oil Conference*. Lima, Peru: Society of Petroleum Engineers, October 2016.

[27] B. S. Aadnoy and G. Hareland, "Analysis of inflow control devices," in *Offshore Europe Oil and Gas Conference and Exhibition 2009*, vol. 1, University of Stavanger, Norway and University of Calgary, Canada. Aberdeen, United kingdom: Society of Petroleum Engineers, 2009 2009, pp. 57–65.

[28] P. R. N. Childs, *Rotating flow.* 30 Corporate Drive, Suite 400, Burlington, MA 01803, USA: Butterworth-Heinemann, 2011.

[29] S. Muppidi and K. Mahesh, "Direct numerical simulation of passive scalar transport in transverse jets," *Journal of Fluid Mechanics*, vol. 598, pp. 335–360, 2008.

[30] E. F. Hasselbrink and M. G. Mungal, "Transverse jets and jet flames. part 1. scaling laws for strong transverse jets," *Journal of Fluid Mechanics*, vol. 443, pp. 1–25, September 2001.

[31] M. Matsumura, *Erosion-corrosion : An Introduction to Flow Induced Macro-cell Corrosion.* Bentham Science Publishers, 2012.

[32] G. Sundararajan, "The solid particle erosion of metallic materials: The rationalization of the influence of material variables," *Wear*, vol. 186-187, no. Part 1, pp. 129–144, July 1995.

[33] Y. I. Oka, S. Mihara, and T. Yoshida, "Impact-angle dependence and estimation of erosion damage to ceramic materials caused by solid particle impact," *Wear*, vol. 267, no. 1, pp. 129–135, 2009.

[34] J. J. Olsen, C. S. Hemmingsen, L. Bergmann, K. K. Nielsen, S. L. Glimberg, and J. H. Walther, "Characterization and erosion modeling of a nozzle-based inflow-control device," *SPE Drilling and Completions*, vol. 32, no. 4, 12 2017.

[35] J. E. Lauritzen and I. B. Martiniussen, "Single and multi-phase flow loop testing results for industry standard inflow control devices," in *Offshore Europe Oil and Gas Conference and Exhibition 2011*, vol. 2, Saudi Aramco, Saudi Arabia and Statoil, Norway. Aberdeen, United kingdom: Society of Petroleum Engineers, September 2011, pp. 1002–1015.

[36] T. A. Abdelfattah, S. Banerjee, G. A. Garcia, and H. T. Nguyen, "Effective use of passive inflow control devices to improve the field development plan," in *SPE Deepwater Drilling and Completions Conference.* Galveston, Texas, USA: Society of Petroleum Engineers, June 2012.

[37] M. Akbari, J. R. Gonzalez, and N. Macklin, "Considerations for optimum inflow control devices (ICDs) selection and placement in horizontal sections," in *SPE Russian Oil and Gas Exploration & Production Technical Conference and Exhibition.* Moscow, Russia: Society of Petroleum Engineers, 2014.

[38] M. P. Coronado, L. Garcia, R. Russell, G. A. Garcia, and E. R. Peterson, "New inflow control device reduces fluid viscosity sensitivity and maintains erosion resistance," in *Offshore Technology Conference.* Houston, Texas: Offshore Technology Conference, May 2009.

[39] C. C. Ezeuko, J. Wang, and I. D. Gates, "Investigation of emulsion flow in steam-assisted gravity drainage," *Society of Petroleum Engineers Journal*, vol. 18, no. 3, January 2013.

[40] J. Plasencia, E. Schaefer, and O. J. Nydal, "Pipe flow of water in oil emulsions in different pipe diameters," in *8th North American Conference on Multiphase Technology.* Banff, Alberta, Canada: BHR Group, June 2012.

[41] O. Becerra, B. Kearl, and A. Sanwoolu, "A systematic approach for inflow control devices testing in mackay river SAGD wells," in *SPE Heavy Oil Conference-Canada.* Calgary, Alberta, Canada: Society of Petroleum Engineers, June 2014.

[42] A. B. Bazyleva, A. Hasan, M. Fulem, M. Becerra, and J. M. Shaw, "Bitumen and heavy oil rheological properties: Reconciliation with viscosity measurements," *Journal of Chemical and Engineering Data*, vol. 55, no. 3, pp. 1389 – 1397, October 2010.

[43] R. D. Blevins, *Applied Fluid Dynamics Handbook*, reprint w. corrections ed. Malabar, Florida 32950: Krieger Publishing Company, 1992.

[44] ANSYS, "ANSYS 17.1 capabilities," Brochure, 2016.

[45] ANSYS Inc., "ANSYS CFX-Solver Theory Guide," ANSYS Inc., Release 17.0, January 2016.

[46] L. Li, C. F. Lange, and Y. Ma, "Association of design and computational fluid dynamics simulation intent in flow control product optimization," *Proceedings of the Institution of Mechanical Engineers, Part B: Journal of Engineering Manufacture*, March 2017.

[47] D. C. Montgomery, *Design and analysis of experiments*, 8th ed. Hoboken, NJ: John Wiley and Sons, Inc., 2013.

[48] M. Noroozi, M. Melo, J. Montoya, and B. Neil, "Optimizing flow control devices in SAGD operations: How different methodologies are functional," in *SPE Thermal Well Integrity and Design Symposium*. Banff, Alberta, Canada: Society of Petroleum Engineers, November 2015.

[49] S. Shad and M. M. Yazdi, "Wellbore modeling and design of nozzle-based inflow control device (ICD) for SAGD wells," in *SPE Heavy Oil Conference Canada 2014*, vol. 3, Devon Canada Corporation, Canada and Schlumberger Information Solutions, Canada. Calgary, AB, Canada: Society of Petroleum Engineers, June 2014, pp. 1701–1710.

[50] Canadian Natural Resources Limited, "Kirby in situ oil sands project directive 54 annual performance presentation," Canadian Natural Resources Limited, Calgary, AB, Canada, Tech. Rep., September 2017.

[51] Dassault Systèmes SolidWorks Corporation, "Solidworks 2016," 175 Wyman Street, Waltham, MA, USA, October 2015.

[52] L. Tang, Y. Tang, and S. Parameswaran, "A numerical study of flow characteristics in a helical pipe," *Advances in Mechanical Engineering*, vol. 8, no. 7, July 2016.

[53] B. Hayes, H. Park, S. Raether, and M. Farrell, "Investigation of turbulent forced convection heat transfer and pressure drop correlations for a helically coiled tube." in *Proceedings of the National Heat Transfer Conference*, vol. 2, Department of Mechanical Engineering, Marquette University, 2001, pp. 1561–1570.

[54] S. Banerjee and B. Hascakir, "Management of steam flashing in SAGD completion design via the implementation of flow control devices," in *SPE Thermal Well Integrity and Design Symposium*. Banff, Alberta, Canada: Society of Petroleum Engineers, November 2015.

Appendix A

Friction Factor Dependence on Reynolds

Since turbulent flow is expected in the devices, the model of $f = C/\mathrm{Re}$ does not appear to be the best suited for the flow. To test the model, the variation in the viscosity sensitivity coefficient is compared to other models of the form $f = C/\mathrm{Re}^n$, where n is a fixed exponent. By selecting an appropriate exponent, the model can approximate the turbulent friction factor. This gives the model for deriving the criteria as

$$\Delta P = \frac{\rho u^2}{C_{\mathrm{qfc}}} + \frac{C_{\mathrm{vis}}\,\delta\rho^{1-n}u^{2-n}\mu^n}{D^{1+n}} \tag{A.1}$$

First an exponent of $n = 0.15$ is used. The viscosity sensitivity values are given for $n = 1$ and $n = 0.15$ in Tables A.1 and A.2 respectively. The vortex device is not considered in this comparison.

Table A.1: Viscosity sensitivity for $n = 1$.

Flow rate	15° Nozzle	40° Nozzle	Channel	Expanding Nozzle	Diode
2.30 m^3/d	112.3	205.4	963.6	4.248	60.72
25.32 m^3/d	303.6	419.6	1,585	17.34	477.8
48.33 m^3/d	509.9	456.4	2,270	17.80	508.4
Relative Range	131%	60%	82%	78%	94%

While the relative range is reduced for the diode, the average relative range increased. Thus a value of $n = 0.15$ provides no improvement.

To further test this model, the exponent n is adjusted to find the minimum average relative range. This was found for an exponent of $n = 0.708$. the results for this model are given in Table A.3.

Although there is some improvement, the criteria is still dependent on the flow rate. In addition, this exponent is adapted for these devices and is not the best value in general. Thus, changing the model does not provide a significant improvement and introduces the fluid density into the calculations. Changing the model would also affect the calculation of the quadratic flow coefficient due to the change in the exponent of the flow rate.

Table A.2: Viscosity sensitivity for $n = 0.15$.

Flow rate	15° Nozzle	40° Nozzle	Channel	Expanding Nozzle	Diode
2.30 m^3/d	0.633	1.199	5.349	0.034	0.341
25.32 m^3/d	0.245	0.305	1.231	0.012	0.384
48.33 m^3/d	0.237	0.193	1.036	0.006	0.234
Relative Range	162%	302%	366%	233%	39%

Table A.3: Viscosity sensitivity for $n = 0.708$.

Flow rate	15° Nozzle	40° Nozzle	Channel	Expanding Nozzle	Diode
2.30 m^3/d	15.84	29.31	135.2	0.681	8.552
25.32 m^3/d	21.96	29.27	113.2	1.18	34.53
48.33 m^3/d	30.52	26.45	135.0	0.983	30.32
Relative Range	67%	10%	21%	42%	75%

Appendix B

Well Case Calculations

Let the following variables be used for the well

- L_{total} = Total length of the well
- L_{section} = Length of the section between two packers
- L_{domain} = Length of the CFD domain
- N_{section} = Number of sections in the well
- N_{icd} = Number of ICDs per section
- N_{port} = Number of ports per ICD
- N_{slot} = Number of slots in the domain
- N_{location} = ICD number starting from the heel of the well
- Q_{well} = Total well production
- Q_{slot} = Fixed slot flow rate per slot
- Q_{annulus} = Flow rate from the annulus
- Q_{icd} = Flow rate from a single icd
- $Q_{\text{inner liner}}$ = Flow rate in the inner liner at ICD number N_{location}
- A_{slot} = Cross sectional area of a slot
- A_{annulus} = Cross sectional area of the annulus
- A_{icd} = Minimum cross sectional area in the ICD
- $A_{\text{inner liner}}$ = Cross sectional area of the inner liner
- D_{slot} = Hydraulic diameter of a slot
- D_{annulus} = Hydraulic diameter of the annulus
- D_{icd} = Minimum diameter of the ICD
- $D_{\text{inner liner}}$ = Diameter of the inner liner
- u_{slot} = Slot average velocity boundary condition
- u_{annulus} = Annulus average velocity boundary condition

- u_{icd} = ICD average velocity

- $u_{\text{inner liner}}$ = Inner liner average velocity boundary condition

- Re_{slot} = Reynolds number in the slot

- $\text{Re}_{\text{annulus}}$ = Reynolds number in the annulus

- Re_{icd} = Reynolds number in the ICD

- $\text{Re}_{\text{inner liner}}$ = Reynolds number in the inner liner

Assumptions

- Even well production

- Equal sized section so that $L_{\text{section}} = L_{\text{total}}/N_{\text{section}}$

- Evenly spaced ICDs

The total flow rate from the annulus entering the domain is given by calculating the fraction of the total production contributing to the flow.

$$Q_{\text{annulus}} = Q_{\text{well}} \left(\frac{L_{\text{total}}}{N_{\text{section}} N_{\text{icd}}} - L_{\text{domain}} \right) L_{\text{total}}^{-1} \tag{B.1}$$

The total flow rate through the ICD is then given by

$$Q_{\text{icd}} = Q_{\text{annulus}} + Q_{\text{slot}} N_{\text{slot}} \tag{B.2}$$

The flow rate in the inner liner entering the domain for ICD number N_{location} is given by

$$Q_{\text{inner liner}} = Q_{\text{well}} \left(\frac{N_{\text{icd}} N_{\text{section}} - N_{\text{location}}}{N_{\text{icd}} N_{\text{section}}} \right) \tag{B.3}$$

Based on these flow rates, the average velocity boundary conditions can be calculated.

$$u_{\text{slot}} = \frac{Q_{\text{slot}}}{A_{\text{slot}}} : \quad u_{\text{annulus}} = \frac{Q_{\text{annulus}}}{2 A_{\text{annulus}}} : \quad u_{\text{inner liner}} = \frac{Q_{\text{inner liner}}}{A_{\text{inner liner}}} \tag{B.4}$$

Based on these flow rates, the Reynolds number in the slots and annulus are given by

$$\text{Re}_{\text{slot}} = \frac{\rho u_{\text{slot}} D_{\text{slot}}}{\mu} : \quad \text{Re}_{\text{annulus}} = \frac{\rho u_{\text{annulus}} D_{\text{annulus}}}{\mu} \tag{B.5}$$

where the hydraulic diameter of the of the slot and annulus are given by

$$D_{\text{slot}} = \frac{(Length)(Width)}{2(Length + Width)} : \quad D_{\text{annulus}} = (Outer Diameter) - (Inner Diameter) \tag{B.6}$$

The Reynolds number in the inner liner and the ICD are given by

$$\text{Re}_{\text{inner liner}} = \frac{\rho u_{\text{inner liner}} D_{\text{inner liner}}}{\mu} : \quad \text{Re}_{\text{icd}} = \frac{\rho u_{\text{icd}} D_{\text{icd}}}{\mu} \tag{B.7}$$

Appendix C

Geometry Dimensions
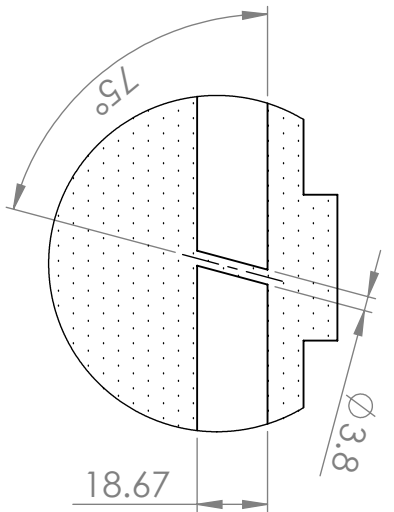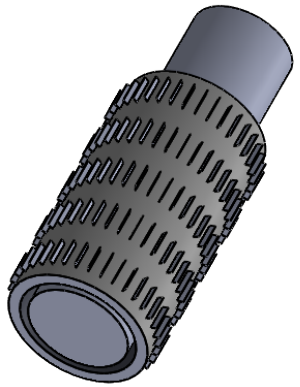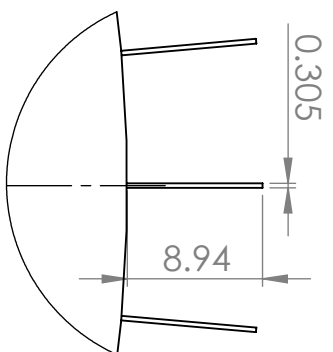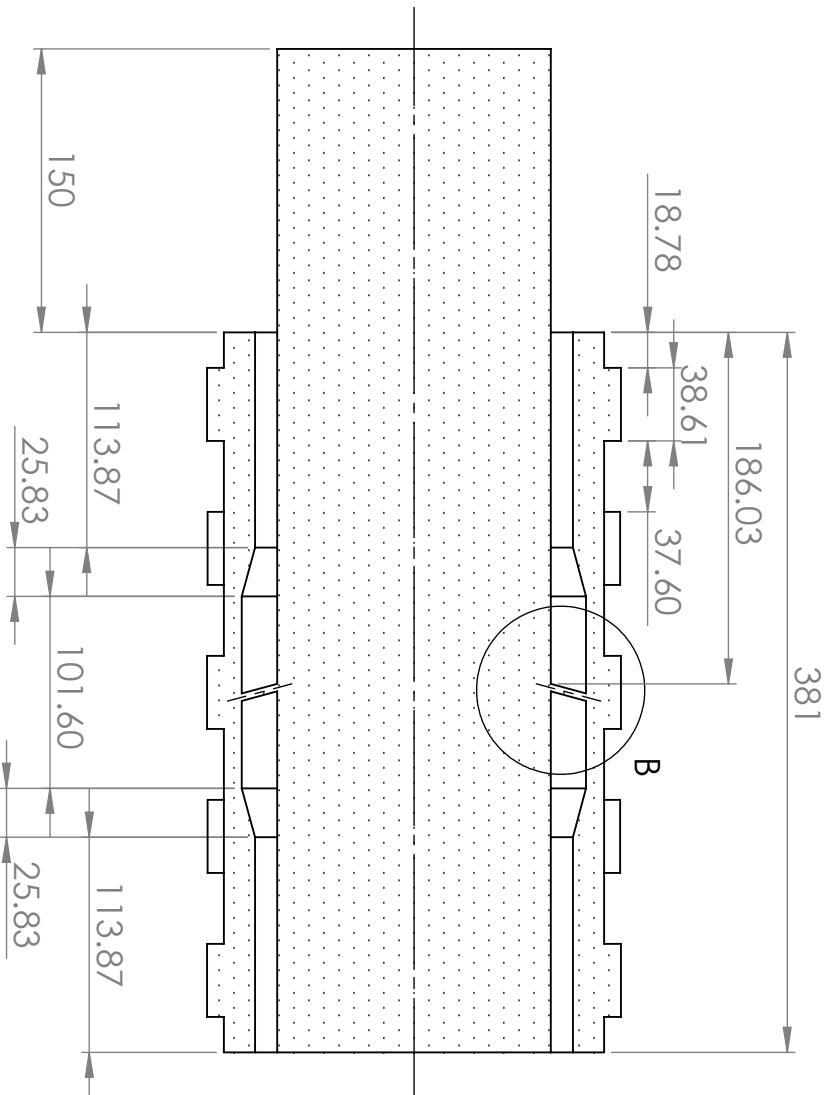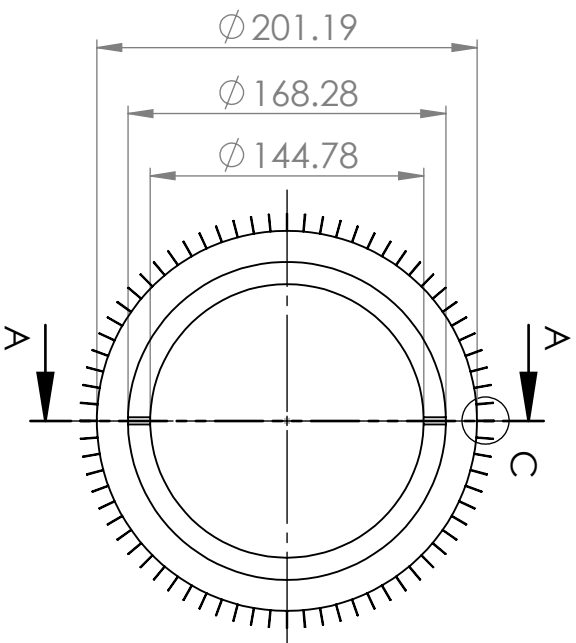
SECTION A-A

150
18.78
38.61
186.03
37.60
113.87
25.83
381
101.60
25.83
113.87

B

DETAIL B
SCALE 1 : 2

75°
∅3.8
18.67

∅201.19
∅168.28
∅144.78

A
A
C

98

DETAIL C
SCALE 2 : 1

0.305
8.94

Scale: 1 : 4

15° Nozzle

Page: 1 of 1

SECTION A-A

DETAIL B
SCALE 1 : 2

50°

Ø3.8

180.11

B

B

A

A

A

A

99

Dimensions are in
milimeters unless otherwise
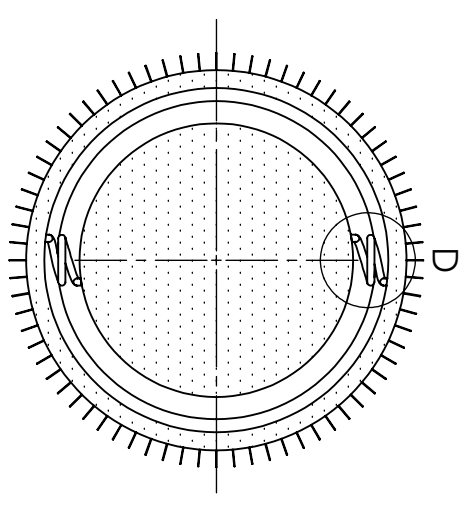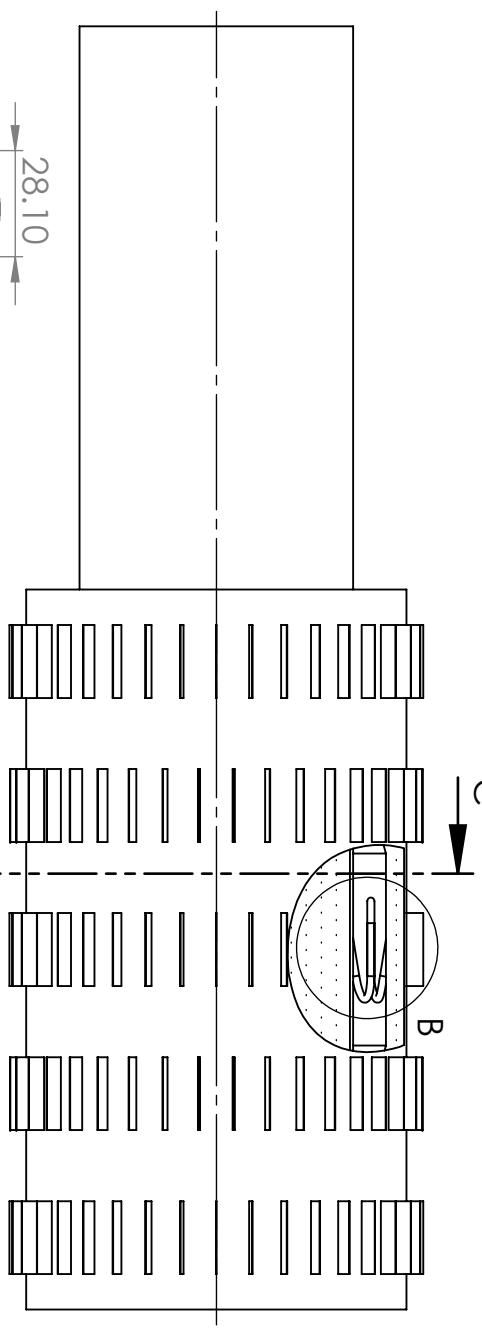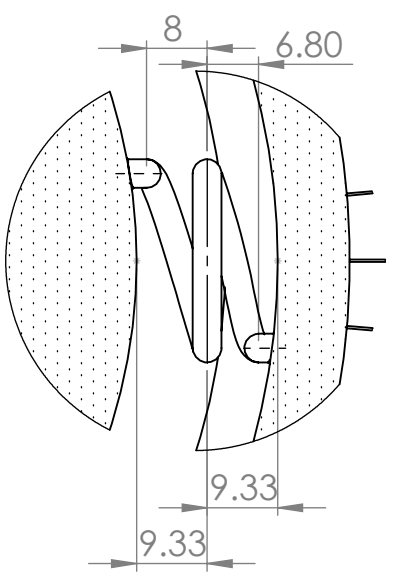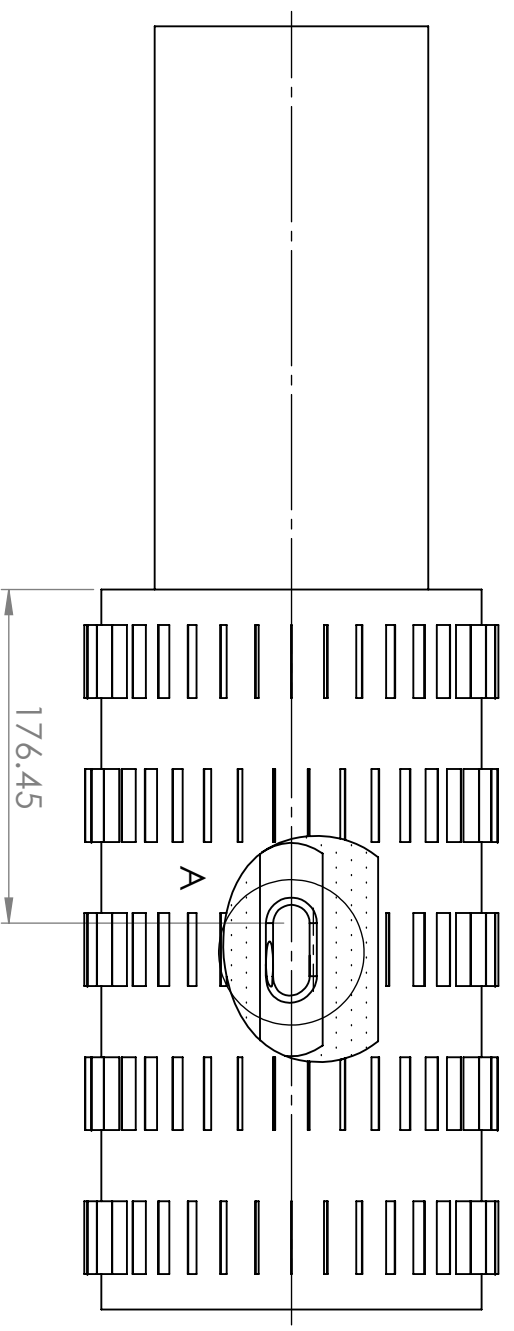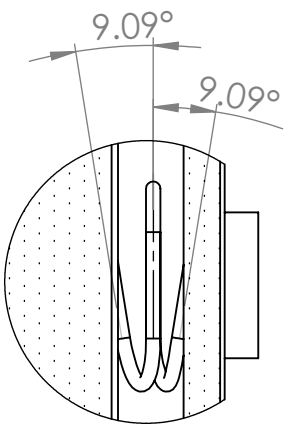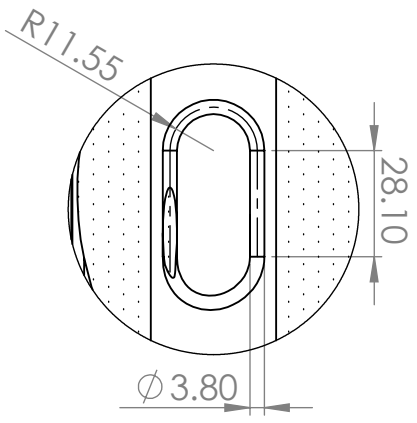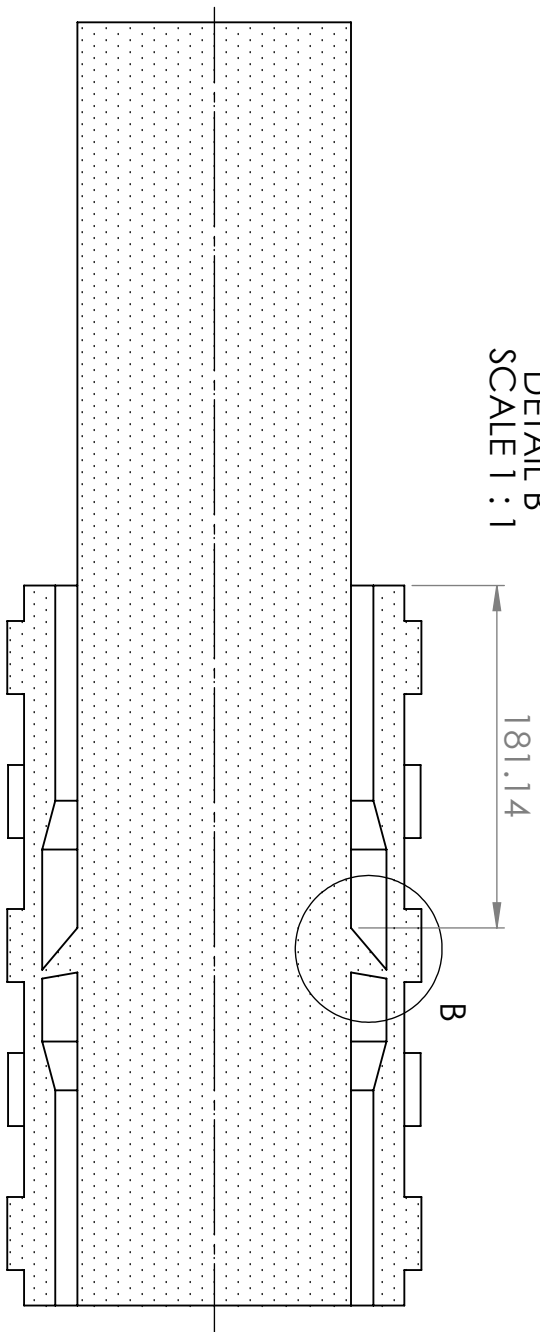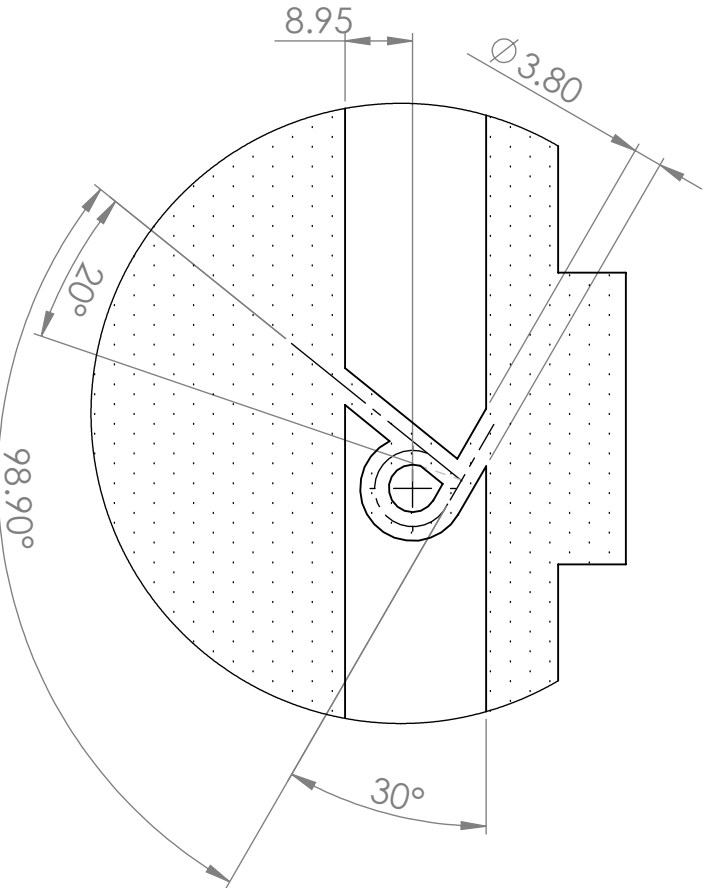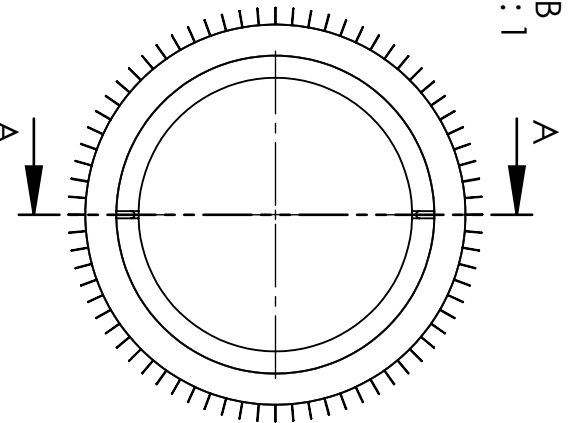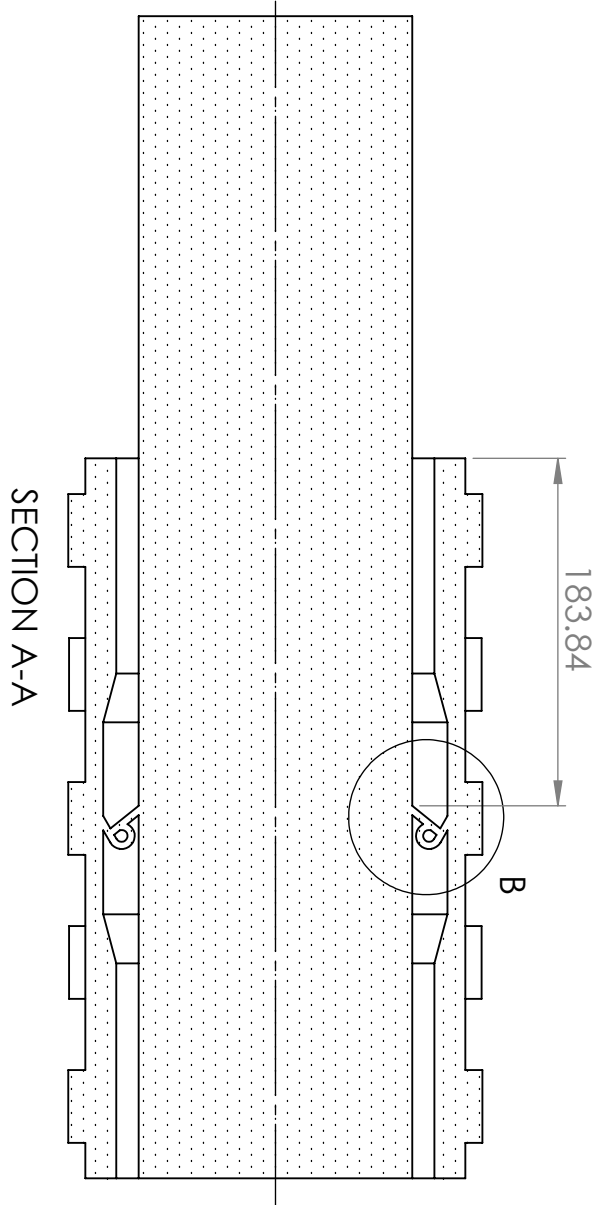specified

Scale: 1 : 4

40° Nozzle

Page: 1 of 1

DETAIL A
SCALE 1 : 2

R11.55

28.10

⌀3.80

DETAIL B
SCALE 1 : 2

9.09°

9.09°

C

C

A

B

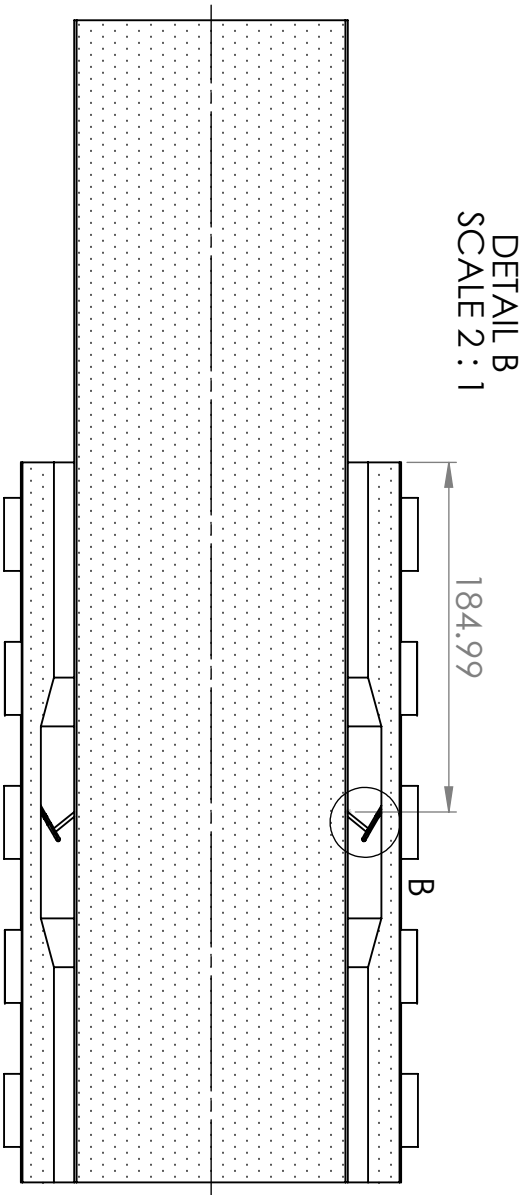176.45

SECTION C-C

D

DETAIL D
SCALE 1 : 1

8

6.80

9.33

9.33

100

Dimensions are in
milimeters unless otherwise
specified

Scale: 1 : 4

Channel

Page: 1 of 1

DETAIL B
SCALE 1 : 1

60°

20°

1.90

SECTION A-A

181.14

B
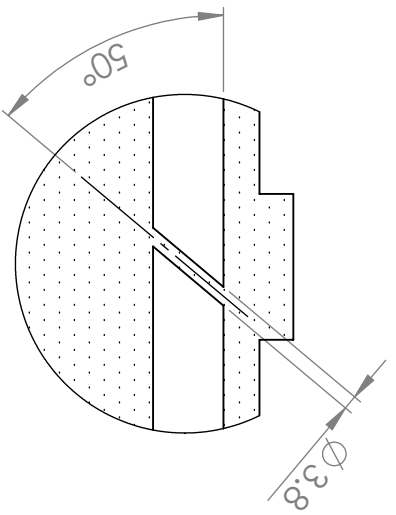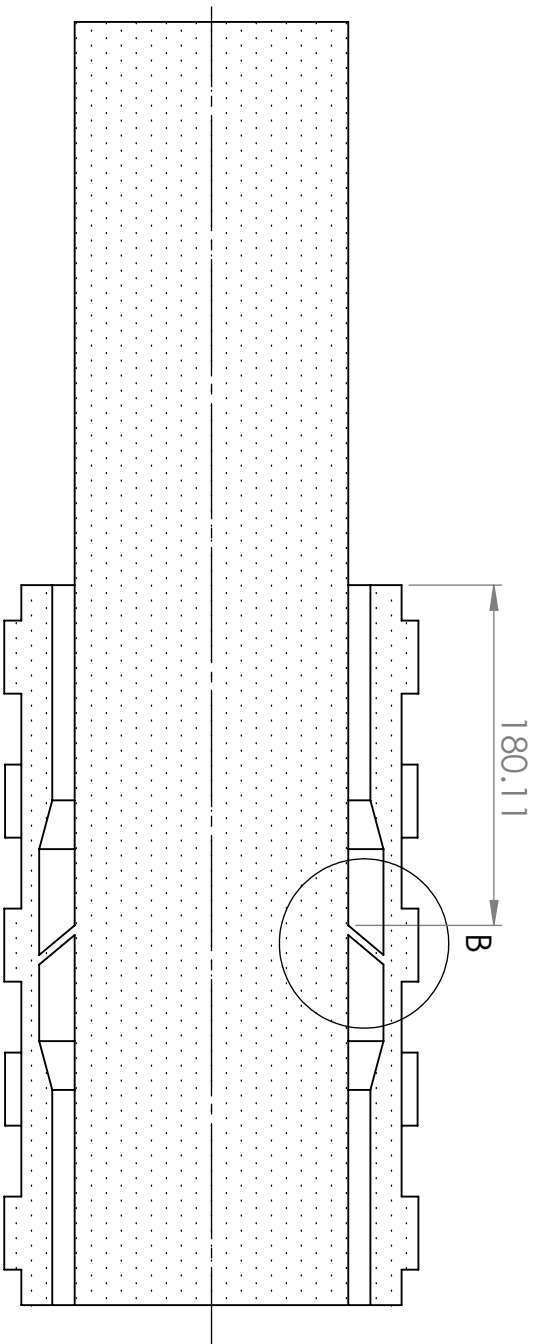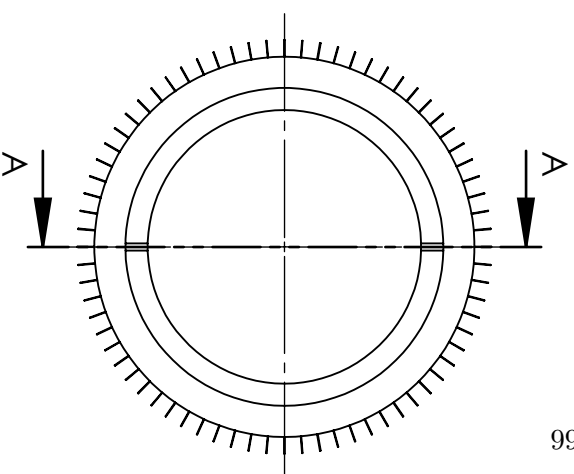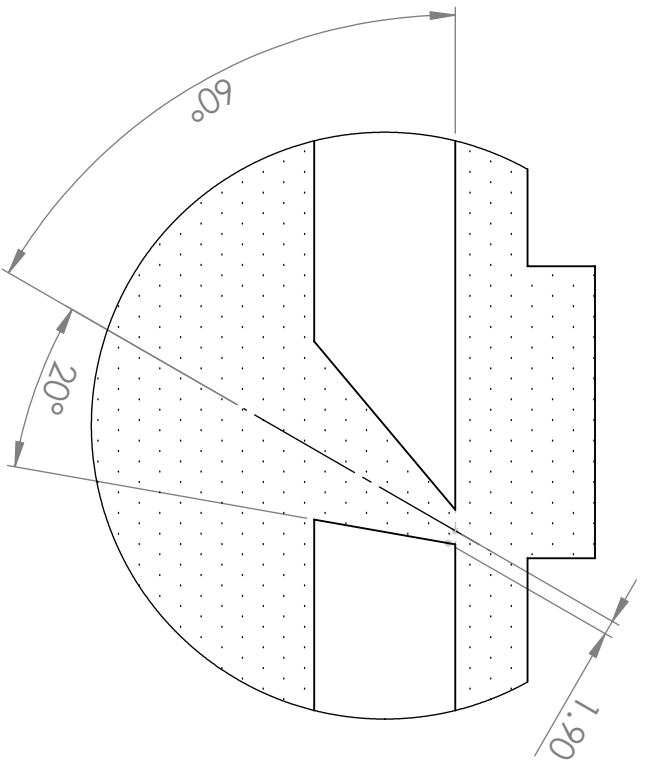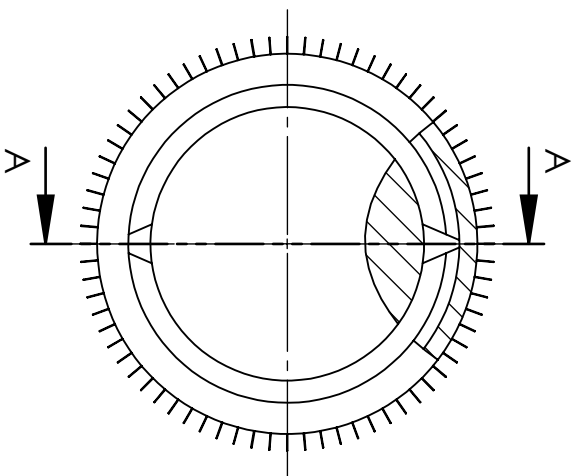
Dimensions are in
milimeters unless otherwise
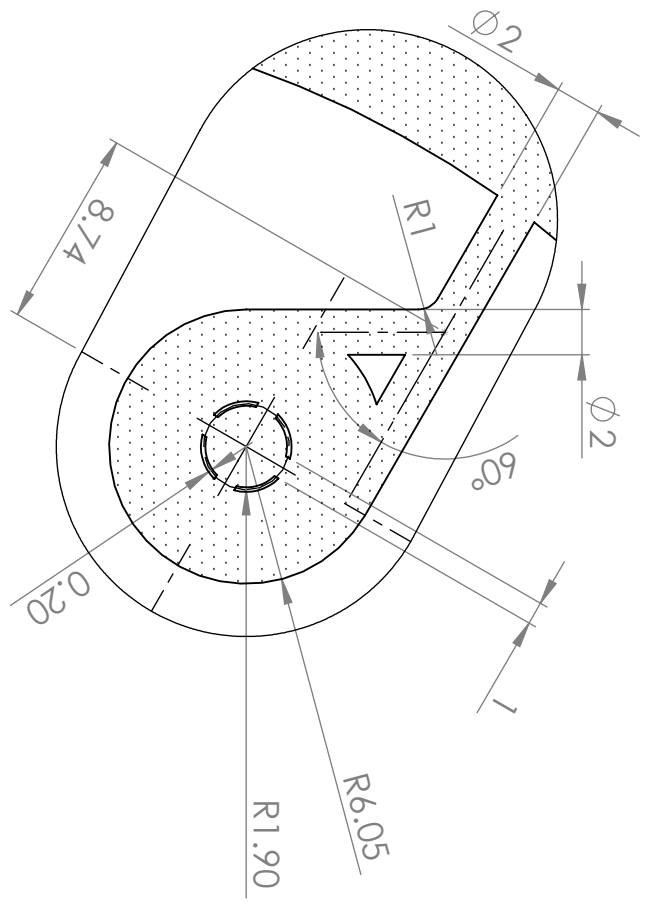specified

Scale: 1 : 4

Expanding
Nozzle

Page: 1 of 1

A

A

101

SECTION A-A

183.84

B

DETAIL B
SCALE 1 : 1

8.95

Ø 3.80

20°

98.90°

30°

Dimensions are in
milimeters unless otherwise
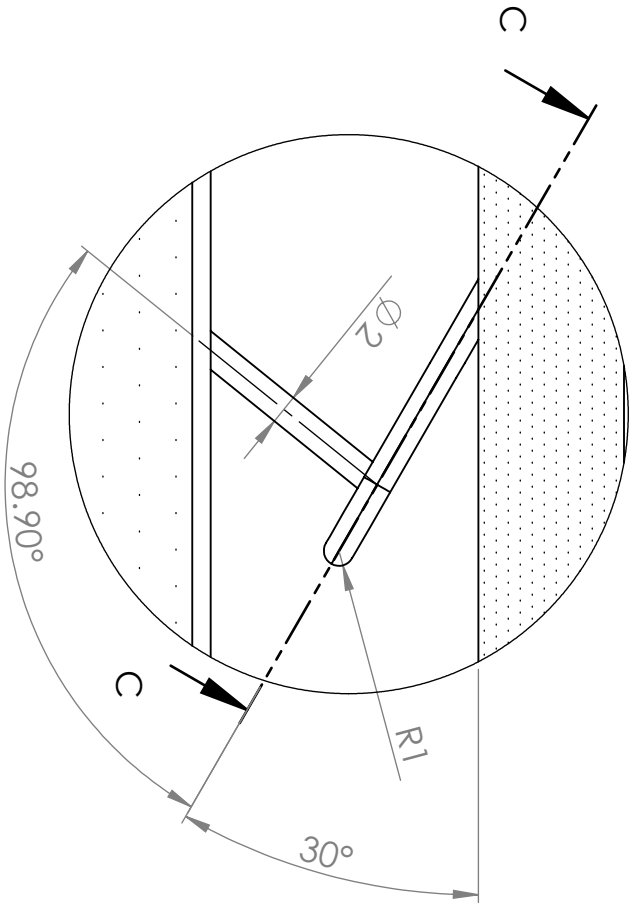specified

Scale: 1 : 4
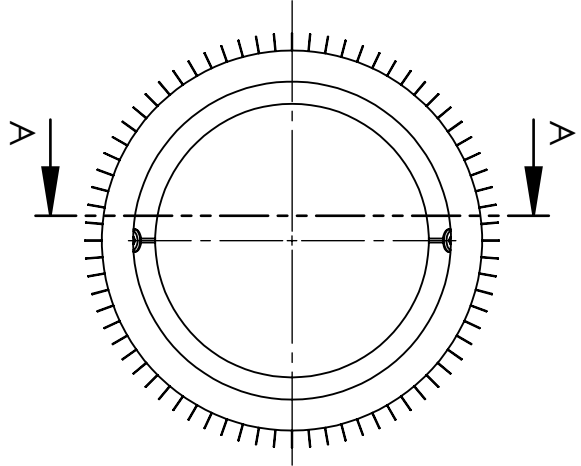
Diode
Nozzle

Page: 1 of 1

DETAIL B
SCALE 2 : 1

SECTION A-A

98.90°

R1

30°

∅2

184.99

B

SECTION C-C
SCALE 3 : 1

∅2

R1

8.74

∅2

60°

0.20

1

R6.05

R1.90

A

A

103

Appendix D

Fluidic Diode Optimization

To optimize the dimensions of the diode nozzle the device is considered by itself, neglecting the surrounding well components. The device is shown in Figure D.1. The three main parameters investigated will be the split angle A, the join angle B, and the relative diameter of the loop branch.
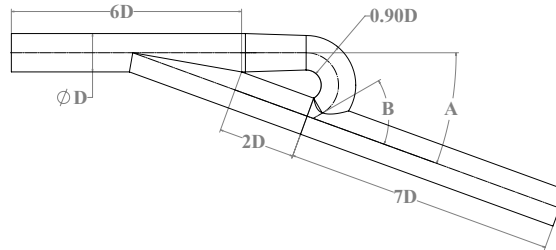

Figure D.1: Geometry of the diode.

Due to physical constraints, the angles (A and B) ranged from 20 to 80 degrees and the diameter of the loop from 0.1 to 0.9 times the diameter of the main pipe. The diameter of the main pipe and the length between the two branches was held constant. While the geometry can be extended beyond these constraints for some cases, it is kept within these constraints to allow for a factional factorial design of experiments.

The Reynolds number for the diode is defined as Re=$\rho u D/\mu$, where D is the diameter entering the device and u is the average velocity of the flow entering the device. Flow rates were selected so that the Reynolds number would be greater than 2300, for turbulent flow. The five Reynolds numbers were selected evenly from 3000 to 123,000.

Simulations were performed using ANSYS®CFX 17 [44]. The mesh generated for each device used local refinement around the branches and an inflation layer along the wall to accurately model the boundary layer. An example of the mesh used is shown in Figure D.2. A prescribed velocity boundary condition was used at the inlet and an average static pressure condition at the outlet. Turbulence was modelled using a k-ε model, since it helps ensure convergence of the simulation. Although it is not the best model and struggles to accurately model flow separation, this model provides a reasonable estimate of the devices performance. An example of the flow field can be seen in Figure D.3.

The pressure drop across the device was measured by taking the difference of the average pressure at the inlet and the outlet. Once simulations were run at all five flow values, the pressure drop was plotted against the Reynolds number and a second order polynomial of the form $\Delta P = a_0 \operatorname{Re}^2 + a_1 \operatorname{Re} + a_2$ was fitted to the data. From this the coefficient a_0 was extracted as the quantity of interest along with the R^2 value. The goal of the study was to optimize the device by maximizing the coefficient a_0. Although this formulation is different than that for the quadratic flow coefficient, the coefficients are directly linked. By
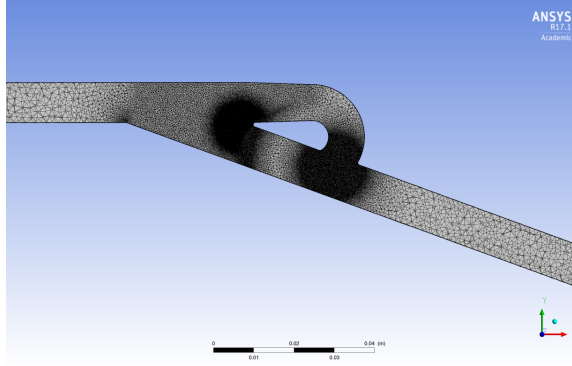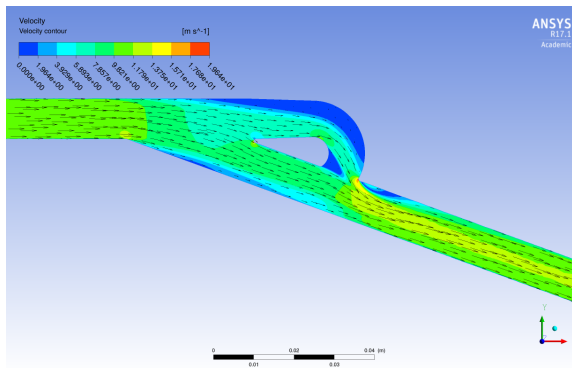
Figure D.2: Example of the diode mesh.

Figure D.3: Example of the simulated flow field.

maximizing the coefficient a_0 the quadratic flow coefficient is minimized.

Based on basic pressure loss tables for split channels [43], it is not expected that the effect of the angle and diameter ratio parameters on this coefficient will be linear and thus each parameter will be tested at three levels. To reduce the number of experiments a fractional factorial 33-1 design with nine experiments will be used. This will reduce the total number of simulations to 45. This factorial is a resolution III design, so all the two and three factor interactions are aliased, although two of the two factor interactions appear in the analysis [47].

Using STATISTICA®13, the results of the 9 experiments were analyzed. The levels of the three parameters for the experiments are shown in Table D.1. To simplify the values the power of 10^{-6} was dropped from the coefficients for the statistical analysis.

D.1 Results

Although not all simulations fully converged, solutions were found for all the simulations. When fitted with 2nd order polynomials all the curves fit with an $R^2 > 0.99$. A Pareto chart of all the effects is given in Figure D.4. The two smallest effects were removed giving the effects shown in Appendix B.

From this it was found that the linear and quadratic effect of the split angle and the linear effect of the diameter are significant. The regression model then gives the equation

$$a_0 = (3.689 + 1.42A + 0.783A^2 - 0.394B^2 + 0.84C - 0.239C^2 - 0.548AB)10^{-6} \quad \text{(D.1)}$$

Table D.1: Factional factorial cases.

Split angle (A)	Join angle (B)	Diameter ratio (C)
20	20	0.1
20	50	0.9
20	80	0.5
50	20	0.9
50	50	0.5
50	80	0.1
80	20	0.5
80	50	0.1
80	80	0.9

Where A is the split angle, B is the join angle, and C is the loop diameter. The function is in terms of the coded values ranging from -1 to 1. The fitted response curves are given in Figure D.5. Based on this model the optimum design to maximize the 2nd order coefficient has a split angle of 80°, a join angle of 50°, and a loop diameter of 0.9D. This gives a predicted value of a_0=6.49E-6 Pa, when inserted into equation D.1. Since this simulation had not been done a further simulation was done at these levels.

To check if the model is valid, the half normal probability plot and observed versus predicted plot are given in Figures D.6 and D.7. Based on these plots the data seems to be normally distributed. The half-normal probability plot also confirms the significant effects found earlier. Looking at the predicted versus residual plot in Figure D.8 indicates the data has equal variance. Thus the data meets the necessary conditions for an ANOVA analysis.

D.2   Discussion

Using the optimized values a further set of five simulations was performed for a device with a split angle of 80°, a join angle of 50°, and a loop diameter of 0.9D. This design gave a coefficient value of 6.61E-6 Pa. Comparing this the the predicted value, the relative error of the prediction is 1.8%. Therefore, this model did a good job of optimizing and predicting the design. This value for a_0 corresponds to a quadratic flow coefficient value of 1.20.

Based on these results it appears that the best design uses a large split angle and a large diameter loop. By using a large split angle and a large diameter for the loop branch, the amount of fluid in the loop is maximized resulting in the best performance of the design. By using a medium join angle a balance is reached between the flow being directed upstream and across the pipe. Overall the most significant factor is the split angle.

D.3   Continued Optimization

For this optimization the values of the parameters were kept within the range restrictions made at the beginning. To further optimize the device the split angle and diameter ratio were extended. Based on the optimization the join angle was held at 50°, the diameter ratio was set to a maximum value of one, and the split angle was increased to 120°. Adding the value from these simulation to the other results, a curve was fitted to the data. Based on this the maximum was predicted at a join angle of 20°, a split angle of 100.3°, and a diameter ratio of one. To further optimize simulations were run at these values, giving a quadratic flow coefficient of 0.968. With this added value the optimum value given by the curve fitting was a join angle of 20°, a split angle of 98.9°, and a diameter ratio of one. This set of parameters was then used for the diode nozzle used in the study.
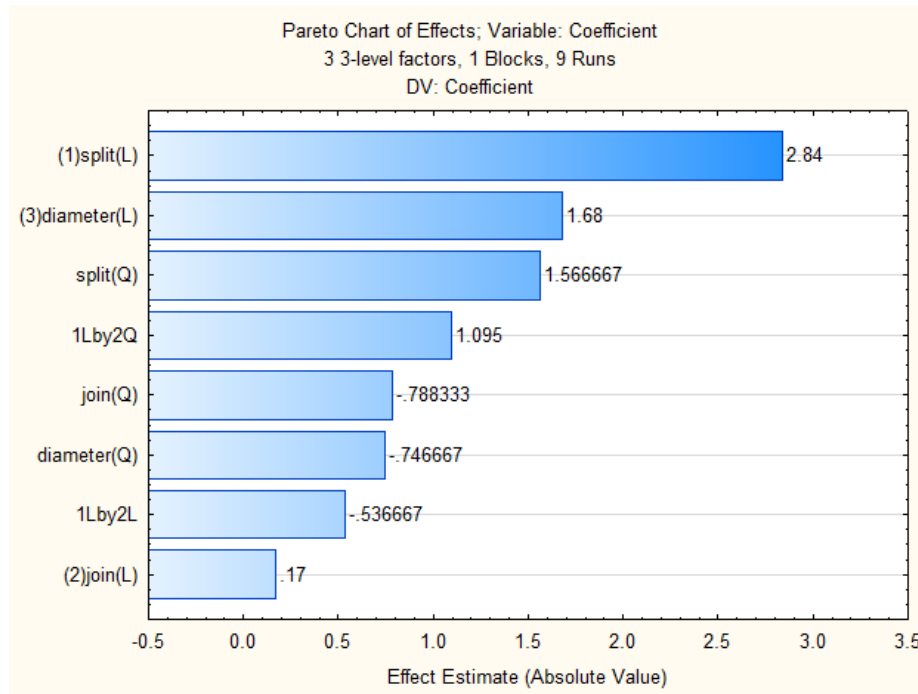
Figure D.4: Pareto chart.

The values for the quadratic flow coefficient in the optimization are large compared to the value of 0.46 found for the diode nozzle. This is due to the lack of entrance and exit losses that contribute minor losses that decrease the quadratic flow coefficient.

D.4 Conclusions

Using design of experiments the effects of three design parameters were investigated and the optimum design was selected. In order to minimize the quadratic flow coefficient, the design should have a split angle of 98.9°, a join angle of 50° and a diameter in the loop of 1. When implemented as a flow control device this design should provide a rapid and sudden transition from a low pressure drop at low flow rates to a high pressure drop at high flow rates.
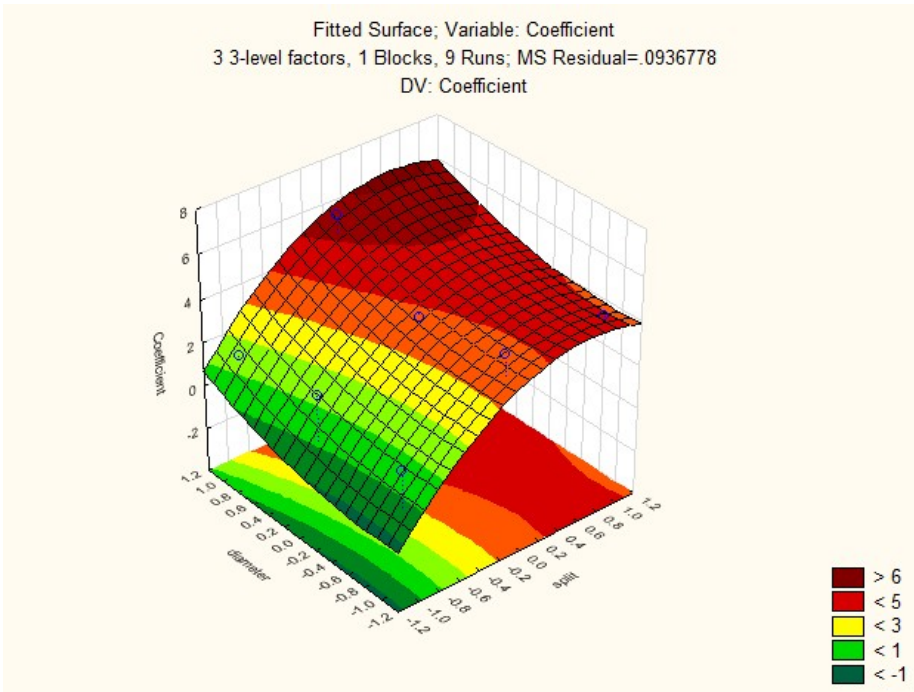
(a) Fitted curve of diameter versus split angle at a 50° join angle.
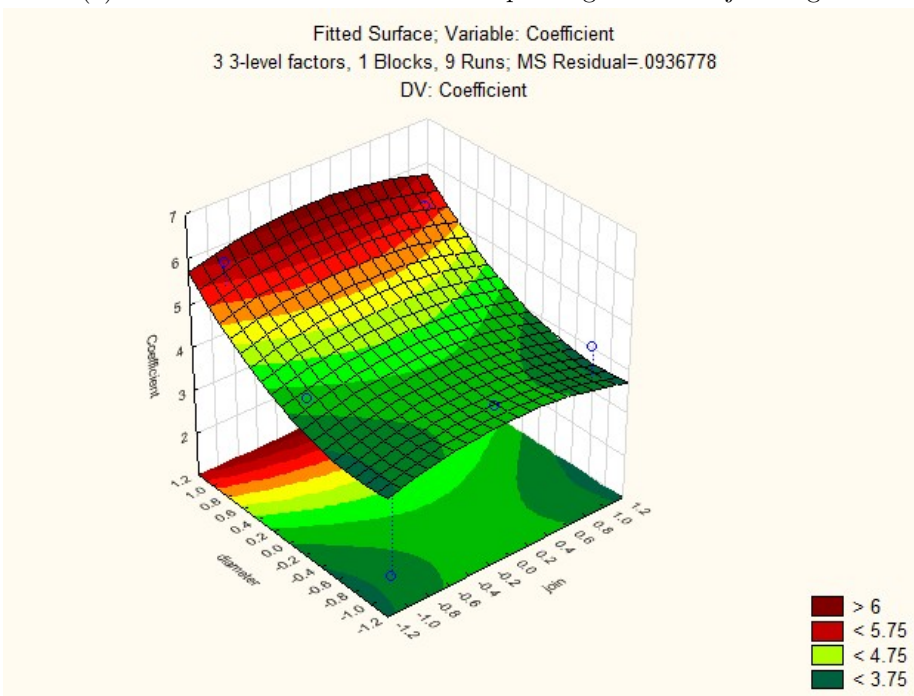
(b) Fitted curve of diameter versus join angle at an 80° split angle.

Figure D.5: Fitted curves.
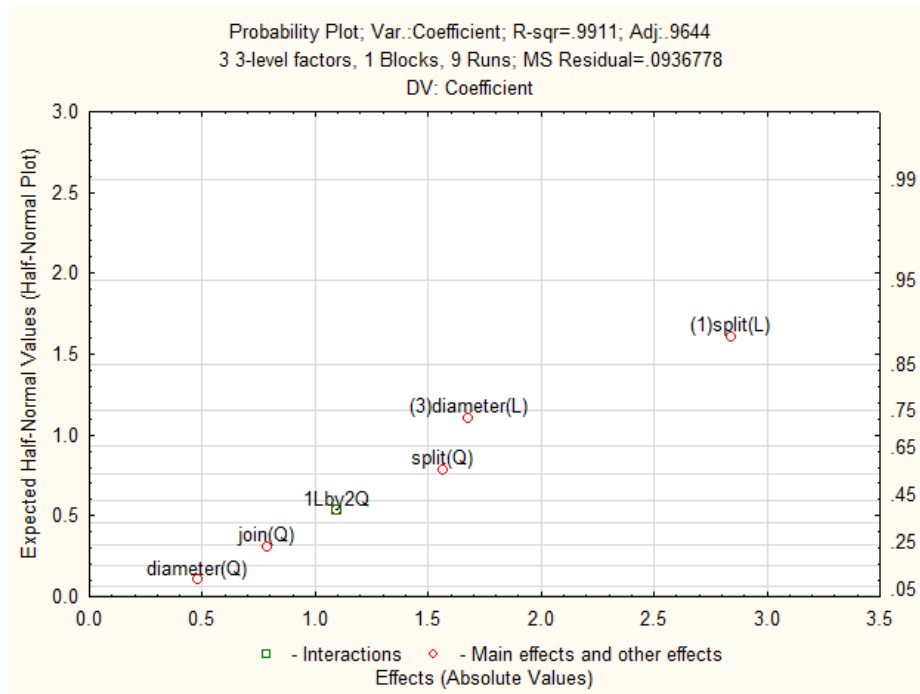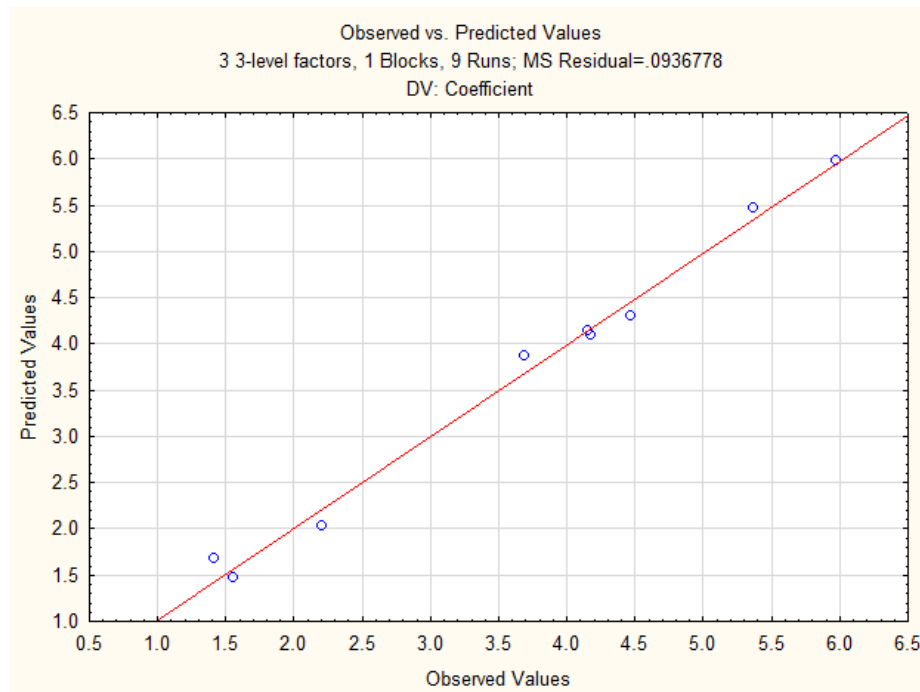
Figure D.6: Half-normal plot.
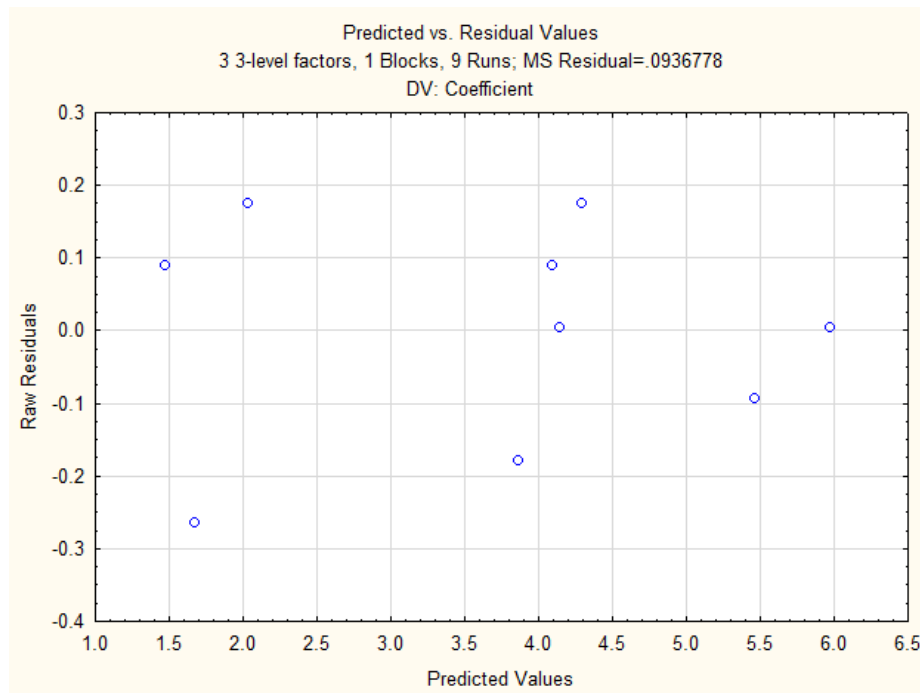

Figure D.7: Observed versus predicted plot.

Figure D.8: Predicted versus residual values.

Appendix E

Matlab Code For ICD Comparison

```matlab
%% Script for sizing and comparing ICDs for a given FRR value, using the
%  quadratic flow coefficient and viscosity sensitivity
clear, clc
% set properties for FRR
rho_FRR=1000;                          %density kg/m^3
mu_FRR=0.001;                          %viscosity Pa s
Q_FRR=3.441e-4;                        %volumetric flow rate m^3/s
%FRR value for the comparison
FRR=0.8
% Device names
device_names={'15^\circ Nozzle','40^\circ Nozzle','Channel',...
    'Expanding Nozzle','Diode Nozzle','Vortex Device'}
% corresponding criteria 1 qfc 2 vis
criteria=[1.414, 1.132, 0.8123, 1.686, 0.4616, 0.1929;...
    303.6, 419.6, 1585,  17.34, 477.8,  -3150]
% number of devices
n=4
% device scale, m
delta=0.018669
% function to size device diameter
d=@(c1,c2) ((16*rho_FRR*Q_FRR^2)/(n^2*pi^2*c1*100000*FRR) +...
    (4*c2*delta*Q_FRR*mu_FRR)/(n*pi*100000*FRR))^0.25;
% device diameters
for i=1:length(criteria(1,:))
    D(i)=d(criteria(1,i),criteria(2,i))
end
% fluids for comparison
fluid_names={'Bitumen at 200^\circ C','Water at 25^\circ C',...
    'Water at 200^\circC'}
%density kg/m^3 (bitumen@200C 2MPa,water@25C 2MPa,water@200C 2MPa)
rho=[888.14 997.9 865];
%viscosity Pa s (bitumen@200C 2MPa,water@25C 2MPa,water@200C 2MPa)
mu=[0.009957 0.0008896 0.0001344];
% flow rate range for comparison
Q_names={'Flow rate, m^3/d','Flow rate, STB/d','Flow rate, m^3/s'}
Q=0:0.1:1000;                              %Flow rate m^3/d
Q(2,:)=Q(1,:)*6.2898105697751;            %Flow rate STB/d
Q(3,:)=Q(1,:)/(24*60*60);                 %flow rate range m^3/s
%Pressure drop in kPa as a function of flow rate
deltaPquad=@(c1,D,rho) (16*rho.*Q(3,:).^2/(n^2*c1*pi^2*D^4))*0.001;
deltaPvisc=@(c2,D,mu) ((4*c2*delta*mu.*Q(3,:))./(n*pi*D^4))*0.001;
```

```matlab
for i=1:length(criteria(1,:))
    for j=1:length(rho)
        %index 1=flow rate 2=fluid 3=device
        Pquad(:,j,i)=deltaPquad(criteria(1,i),D(i),rho(j));
        Pvisc(:,j,i)=deltaPvisc(criteria(2,i),D(i),mu(j));
    end
end
%Combine losses
deltaP=Pquad+Pvisc;
%Set figure index
fig_i=0

%% Comparison of fluids for each device
% To select the desired devices and fluids, enter the corresponding
% indices in the arrays
% '15^\circ Nozzle','40^\circ Nozzle','Channel',
% 'Expanding Nozzle','Diode Nozzle','Vortex Device'
d_s=[1,2,3,4,5,6]
% fluid select 'Bitumen','water at 0^\circ C','water at 200^\circC'
f_s=1:3
% Flow unit select (single value) 'm^3/d','STB/d','m^3/s'
Q_s=2

line_color={'r','g','b','m','c','k'}
%Axis maximum pressure, kPa
Pmax=1000

for j=d_s
    figure(fig_i+1)
    hold on
    line_index=1
    for i=f_s
        p(line_index)=plot(Q(Q_s,:),deltaP(:,i,j),char(line_color(i)))
        index_Q(i)=find(deltaP(:,i,j)>Pmax,1)
        line_index=line_index+1
    end
    p(line_index)=plot([min(Q(Q_s,:)) max(Q(Q_s,:))],[600 600],'-k')
    hold off
    Qmax=max(Q(Q_s,index_Q))
    axis([0 Qmax 0 Pmax]);
    %Plot formating
    p_axes=gca;
    p_legend=legend(fluid_names(f_s));
    px=xlabel(Q_names(Q_s)) ;
    py=ylabel('Pressure drop, kPa');
    ptitle=title(device_names(j));
    p_legend.FontName='Arial';
    p_legend.FontWeight='bold';
    p_legend.FontSize=13;
    p_legend.LineWidth=2;
    p_legend.Location='northwest';
    px.FontName=p_legend.FontName;
    py.FontName=p_legend.FontName;
    px.FontWeight=p_legend.FontWeight;
    py.FontWeight=p_legend.FontWeight;
    ptitle.FontName=p_legend.FontName;
    ptitle.FontWeight=p_legend.FontWeight;
    ptitle.FontSize=18;
    px.FontSize=18;
```

```matlab
        py.FontSize=px.FontSize;
        p_axes.LineWidth=2;
        p_axes.FontSize=13;
        for j=1:line_index
            p(j).LineWidth=2;
        end
        fig_i=fig_i+1
end
%% Comparison of devices for each fluid
% To select the desired devices and fluids, enter the corresponding
% indices in the arrays
% '15^\circ Nozzle','40^\circ Nozzle','Channel',
% 'Expanding Nozzle','Diode Nozzle','Vortex Device'
d_s=[1,2,3,4,5,6]
% fluid select 'Bitumen','water at 0^\circ C','water at 200^\circC'
f_s=1:3
% Flow unit select (single value) 'm^3/d','STB/d','m^3/s'
Q_s=2

%line_color={'r','g','b','m','c','k','y'}
line_color=[1,0,0;0,1,0;0,0,1;1,0,1;0,1,1;1,0.5,0;1,1,0]
%Axis maximum pressure, kPa
Pmax=1000

for i=f_s
    figure(fig_i+1)
    hold on
    line_index=1
    for j=d_s
        p(line_index)=plot(Q(Q_s,:),deltaP(:,i,j),'Color',line_color(j,:))
        index_Q(i)=find(deltaP(:,i,j)>Pmax,1)
        line_index=line_index+1
    end
    p(line_index)=plot([min(Q(Q_s,:)) max(Q(Q_s,:))],[600 600],'-k')
    hold off
    Qmax=max(Q(Q_s,index_Q))
    axis([0 Qmax 0 Pmax])
    %Plot formating
    p_axes=gca
    p_legend=legend(device_names(d_s))
    px=xlabel(Q_names(Q_s))
    py=ylabel('Pressure drop, kPa')
    ptitle=title(fluid_names(i))
    p_legend.FontName='Arial'
    p_legend.FontWeight='bold'
    p_legend.FontSize=13
    p_legend.LineWidth=2;
    p_legend.Location='northwest'
    px.FontName=p_legend.FontName
    py.FontName=p_legend.FontName
    px.FontWeight=p_legend.FontWeight
    py.FontWeight=p_legend.FontWeight
    ptitle.FontName=p_legend.FontName
    ptitle.FontWeight=p_legend.FontWeight
    ptitle.FontSize=18
    px.FontSize=18
    py.FontSize=px.FontSize
    p_axes.LineWidth=2
    p_axes.FontSize=13;
```

```
    for j=1:line_index
        p(j).LineWidth=2
    end
    fig_i=fig_i+1
end
```